Investigations on manufacturing of NiTi shape memory alloy bimorph-based flexible mirrors and microactuators for Opto-Mechatronics Applications

Ph.D. THESIS

By

Kaushal Gangwar

Department of Mechanical Engineering

Indian Institute of Technology Indore

NOVEMBER 2024

Investigations on manufacturing of NiTi shape memory alloy bimorph-based flexible mirrors and microactuators for Opto-Mechatronics Applications

A THESIS

Submitted in partial fulfillment of the requirements for the award of the degree

of

DOCTOR OF PHILOSOPHY

By

Kaushal Gangwar

Department of Mechanical Engineering

Indian Institute of Technology, Indore

NOVEMBER 2024

Indian Institute of Technology Indore

CANDIDATE'S DECLARATION

I hereby certify that the work being presented in the thesis titled **Investigations on manufacturing of NiTi shape memory alloy bimorph based flexible mirrors and microactuators for Opto-Mechatronics Applications** in the partial fulfilments of the requirements for the award of the degree of **DOCTOR OF PHILOSOPHY** and submitted in the **Department of Mechanical Engineering, Indian Institute of Technology, Indore** is an authentic record of my own work performed during the time period of August, 2021 to November, 2024 under the supervision of Prof. I. A. Palani, Department of Mechanical Engineering, Indian Institute of Technology, Indore.

The matter presented in the thesis has not been submitted by me for the award of any other degree of this or any other institute.

14/05/2025

Signature of the student with date
(Kaushal Gangwar)

This is to certify that the above statement made by the candidate is correct to the best of my/ourknowledge.

14/05/2025

Signature of Thesis Supervisor #1 with date

Prof. I. A. Palani

Kaushal Gangwar has successfully given his/~~her~~ Ph.D. Oral Examination held on **13/05/2025**.

14/05/2025

Signature of Thesis Supervisor #1 with date

Prof. I. A. Palani

ACKNOWLEDGEMENTS

First of all, I would like to express my deepest gratitude and acknowledge My research guide **Prof. I. A. Palani**, Mechatronics and Instrumentation Lab, for his continuous guidance, patience, motivation, and enthusiasm. His valuable advice, constructive criticism, extensive discussions, and immense knowledge helped me to build a basic understanding of the subject and accomplish my thesis. His research method of developing practical application has been inspiring. During my time of association with him, I learnt a lot of things, both in life and career. He has tremendous multi-tasking and man management skills, which is something I would like to learn and carry with me in life. He has been a mentor who is always true to his position.

I would like to thank **Prof. Suhas Joshi**, Director, IIT Indore, **Dr. S. Dinakaran,** Head of Department, Mechanical Engineering, for supporting me with the sophisticated facilities to conduct my research. I would also like to thank PSPC members **Dr. Eswara Korimilli** and **Dr. Ashish Rajak** for giving their precious time for my assessment and for their valuable comments and suggestions towards enhancing my research work. My sincere thanks **Dr. S. Janakiraman**, DPGC convener for his sincere support.

I would like to thank **Department of Mechanical Engineering**, **IIT Indore** as well as **Department of MEMS, IIT Indore** for allowing access to the facility of various characterization techniques and providing a pleasant atmosphere for research. I would also like to acknowledge **HoD, Department of Mechanical Engineering, IIT Indore** for his constant support throughout the journey**.**

I would also acknowledge My appreciation also extends to **Opto-Mechatronics Group** for their strong support and stimulating discussions. Also,I would like to admire my colleagues for their constant care and endorsement through this period. My sincere appreciation extends to my B. Tech. inmates Srijan, Piyush, Vijay, Kailash, for their help and support during my work. I would also like to acknowledge my school and college friends for being my constant support during my highs and lows.

Finally, I would like to express my deepest gratitude and respect to my parents for introducing me to this world and for being an ever-supportive rock in my life with their unflinching support.

I also acknowledge Science and Engineering Research Board (SERB)-Core Research Grant (CRG) and IIT Indore for their financial assistance to the research work carried out.

Dedicated to my

Parents

ABSTRACT

Shape memory alloy (SMA) thin films-based structures have drawn much attention for a wide variety of applications such as beam deflection, interferometry, optical coherence tomography, microvalves, temperature sensors, micro grippers, micro-pumps, and micro-robots. These phase-change materials allow the freedom to alter the characteristics as per the requirements by changing the composition and fabrication conditions which are of utmost importance for SMA based device fabrication. The current research is fabricating NiTi SMA thin film bimorph-based structures with different techniques and process parameters for opto-mechatronics applications.

In this work NiTi thin film based SMA bimorph was fabricated and its functional behavior towards opto-mechatronics applications were studied. The thin film deposition was carried out in thermal evaporation and e-beam evaporation. Thermal evaporation produces good thickness films with higher substrate-to-film adhesion which is effective for microactuator applications. However, for flexible mirror applications e-beam evaporation can produce a very dense and uniform SMA film on the Kapton polyimide substrate.

Further to improve the actuation response and optical reflectance of the actuators and mirrors, the substrate was subjected to different pre-deposition processes pre-straining, heating (with the help of custom-made fixtures) and laser annealing. Henceforth, significant enhancement was observed for both actuation and optical reflectance. Further, for use of bimorph structures as flexible actuators, laser energy was employed which has improved the adhesion and actuation of thermally deposited samples.

Finally, laser micromachining was employed on the SMA bimorph structures for fabrication of customized actuators and mirrors. Being a non-contact process, it creates minimal damage around the micromachined edges of the actuators and mirrors. Various shapes of actuators and mirrors such as circle, rectangle and optical shutter were

fabricated with such machining process. Lastly, the fabricated mirrors and actuators were used in a Stewart platform structure for laser beam steering application.

List of Publications

S.No.	Journal Publication	Status
1.	**Kaushal Gangwar,** Jayachandran S, Anshu Sahu, Arpit Singh, Palani I.A.- "Influence of Pre-strain on attributes of Ni-rich NiTi/ Kapton polyimide bimorph for flexible mirrors" –*Sensors and Actuators A: Physical*- Volume 341, 1 July 2022, 113607. https://doi.org/10.1016/j.sna.2022.113607.	Published
2.	**Kaushal Gangwar,** Dhruv Gupta, Palani Iyamperumal Anand- "Parametric Investigation on laser annealing of polyimide on improving the characteristics of NiTi SMA-based bimorph towards the development of microactuators" –*Sensors and Actuators A: Physical*-360 (2023) 114536**.** **https://doi.org/10.1016/j.sna.2023.114536.**	Published
3.	**Kaushal Gangwar,** Kailaash Pandiyan**,** Palani I. A.- "Investigation of laser-assisted micromachining of NiTi SMA bimorph-based actuators toward developing optical shutters" -*J. Micromech. Microeng.* – **34** 095002. Doi 10.1088/1361-6439/ad632a.	Published
4.	**Kaushal Gangwar,** Srijan Parashar, Palani Iyamperumal Anand, Realization of SMA bimorph based composite mirror and actuator in a Stewart platform arrangement for beam steering application, Optics & Laser Technology, Volume 187, 2025, 112765, ISSN 0030-3992, **https://doi.org/10.1016/j.optlastec.2025.112765.**	Published

Patent Details:

1. Palani Iyamperumal Anand**, Kaushal Gangwar** and Srijan Parashar "Inchworm inspired shape memory alloy bimorph-based Stewart platform for opto-mechatronic system and method thereof"- **Granted** 24/06/2024 (Patent No.-542727).

TABLE OF CONTENTS

Conclusion and Future Scope

LIST OF FIGURES

LIST OF TABLES

ACRONYMS

S. No.	Acronym	Expansion
1	NiTi	NiTiNoL
2	SMA	Shape memory alloy
3	E-beam	Electron beam
4	A_s	Austenite start temperature
5	A_f	Austenite finish temperature
6	M_s	Martensite start temperature
7	M_f	Martensite finish temperature
8	% LO	% Line Overlap
9	FTIR	Fourier Transform Infrared Spectroscopy
10	Nd: YAG	Neodymium doped Yttrium Aluminium Garnet
11	KW	Kerf width
12	HAZ	Heat affected zone

Chapter 1

This chapter explains the background and focus of the research work. It elaborates about the thesis outline.

Introduction

1.1 Background of SMA based mirror and actuator

Micro-electro mechanical systems (MEMS) have been widely developed and implemented as microactuators and micromirrors. The mirror encompasses applications in optical switches, laser beam deflection[1,2], 3D scanning, interferometry, telescopes, optical coherence tomography[3–5], etc. The MEMS actuators have been employed as micro grippers, microvalves, micro switches, micro robots, and mechanisms for mirror motion. The MEMS mirrors usually depend on external actuation mechanisms involving electrostatic, piezoelectric, electromagnetic, or thermal input. In electrostatic actuation, the electrodes are placed beneath or around the mirror. The application of voltage generates an electrostatic force that moves the mirror. The translation and rotation of the mirror are controlled by varying the input voltage. Electrostatic mirrors exhibit low power consumption and fast response time; however, they face several limitations. The actuation angle greatly influences the performance of the micromirror. The maximum angular tilt required for electrostatic micromirrors is usually up to 90°. Electrostatic forces diminish above nearly one-third of the maximum tilt angle. This happens because the electrostatic torque at the above-mentioned tilt angle exceeds the mechanical restoring torque. Thus, the stability and control of the mirror are reduced. Electrostatic forces are weak, which limits the size of the mirror. Also, the actuation mechanisms have intricate geometries sensitive to dust, humidity, and contamination. Such foreign particles reduce the mechanism's performance and can even lead to seizure.

Piezoelectric mirrors, on the other hand, are actuated when an electric voltage is applied to the piezoelectric actuator attached to the mirror. Piezoelectric mechanisms are employed because of their high precision and fast response. However, their performance is limited due to hysteresis and nonlinearity. The mirror's response to voltage varies depending on its actuation history, reducing its positional accuracy. Additionally, they require high voltages for significant movement, increasing power requirements. Most piezoelectric systems are PZT (lead zirconate titanate) based materials. Lead oxide (PbO) is released during the extraction, synthesis and disposal of PZT-based materials, which adversely affects the environment and humans. Electromagnetic micromirrors involve a small magnet or magnetic material that moves due to the Lorentz force generated by the interaction between current-carrying coils and the magnetic material. They exhibit high actuation range and strong actuation force, but face limitations that limit their practicality and integration in other systems. The miniaturization of the mirror is restricted due to the requirements of attaching a magnet to it. The mechanisms are vulnerable to external magnetic interference. Additionally, the current flow through the coils generates heat, which induces thermal drift and reduces the long-term stability of the mirror.

Thermal mirrors utilize thermal expansion to achieve the mirror displacement. They rely on Joule heating and the difference in coefficient of thermal expansion of the materials employed for two or more layers of the mirror structure, which expand and contract on heat application. They offer stable and large-angle deflection. Bilayer mirrors or bimorphs fabricated on flexible substrates are advantageous due to their simple design and fabrication, extensive range of actuation, and flexible structures. NiTi SMA (shape memory alloy) based bimorph mirrors are advantageous over electrostatic, piezoelectric, and electromagnetic mirrors as they eliminate the need for complex and rigid actuation mechanisms. Bimorph mirrors fabricated on flexible substrates such as Kapton polyimide are easy to fabricate, provide a wide range of actuation, and can even act as a mirror and actuator while eliminating the need for an external actuation mechanism. Fig 1.1 (a) and (b) show electrostatic and piezoelectric mirrors, respectively, utilizing external mechanisms for actuation; however, the thermal bimorph mirror shown in Fig 1.1 (c) is simply a bilayer structure of NiTi thin film deposition on flexible Kapton polyimide substrate capable of reflection and actuation simultaneously.

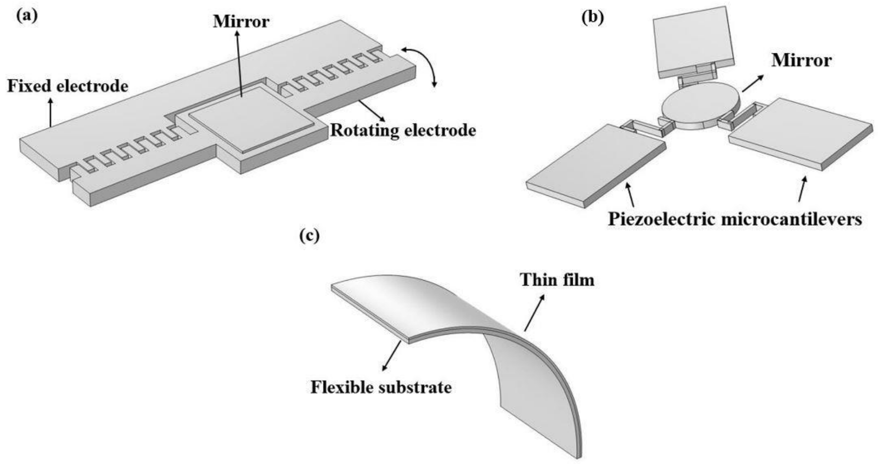

Fig. 1.1: (a) Schematic of electrostatic micromirror driven by horizontal comb drive, (b) Schematic of the piezoelectric micromirror, and (c) Schematic of a flexible thermal mirror.

Table 1 highlights the properties of different kinds of microactuator mechanisms which indicates that SMA thin film-based actuators can achieve high actuation force and actuation displacement compared to other mechanisms with relatively simpler designs.

Table 1: Comparison of different kinds of microactuators

Micro-actuator Type	**Actuation Force**	**Max. Actuation**	**Response time**	**Power Demand**	**Design**
Electro-static	Low (μN to mN)	Low (Up to 100 μm)	Low (<100 μs)	Low (< 1mW)	Intricate
Piezo-electric	High (mN to N)	Low (Up to 5 μm)	Low (< 1 μs to few ms)	Low	Intricate
Thermal	High (100 μN to tens of mN)	High (Up to 100 μm)	Low (Up to 10 ms)	High (Up to 5 V)	Simple

Magnetic	High (mN to N)	High (µM to several mm)	High (µs to ms)	High (Up to 12 V electro-magnets)	Intricate
Shape Memory Alloy	High (mN to N)	High (Up to mm)	High (ms to s)	High (Up to 0.5W)	Simple

The NiTi/Kapton polyimide bimorph structure is also helpful as microactuators due to their high recoverable strain, high force-to-weight ratio and high corrosion resistance of the deposited NiTi films. Some smart materials popularly used as microactuators are electrostatic, electromagnetic, piezoelectric, bimetallic and thermo-pneumatic; however, shape memory alloy provides the highest energy density and a wide range of actuation at lower voltage[6]. The flexibility of the NiTi/Kapton polyimide bimorph structure is key for its application as different customizable actuators. The flexible polyimide substrate helps generate the two-way shape memory effect in the bimorph, which translates into multiple actuation cycles on Joule heating. Also, the transformation temperature range can be manipulated by changing the composition of the film, thus making it suitable for both high temperature and low temperature actuation.

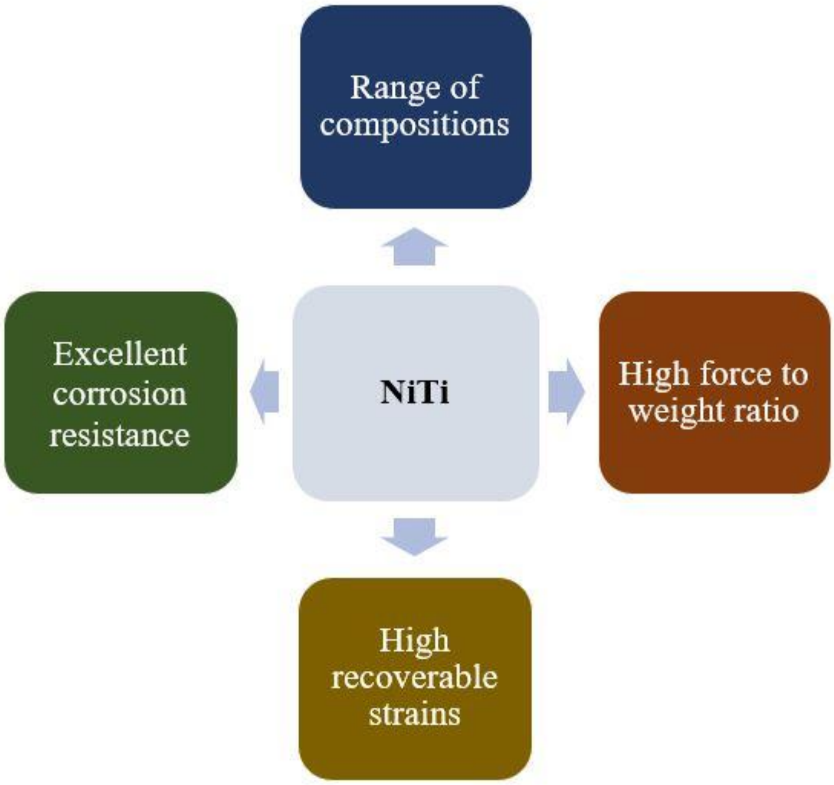

Fig 1.2: Key Material Properties of NiTi SMA Based Alloys Enabling Advanced Functional Applications.

1.2Shape Memory Effect

The shape memory effect can be defined as the ability of the material to regain its original shape when an external stimulus, such as heat or stress, is applied to it. The effect happens due to a reversible crystallographic transformation. Shape memory alloys such as NiTi, NiTiCu, CuAlMn, NiTiHf, etc., have different crystal structures depending on the temperature. The high temperature phase is called as Austenite phase, which has a generally cubic structure. The low temperature phase is referred to as the Martensite phase with a monoclinic structure. Also, an intermediate R phase with a rhombohedral structure exists, but its stability depends on specific conditions, such as substituting a small amount of Ni with Fe or Al. The shape memory effect occurs due to transformation between the Austenite and Martensite phases as shown in Figure 1.3.

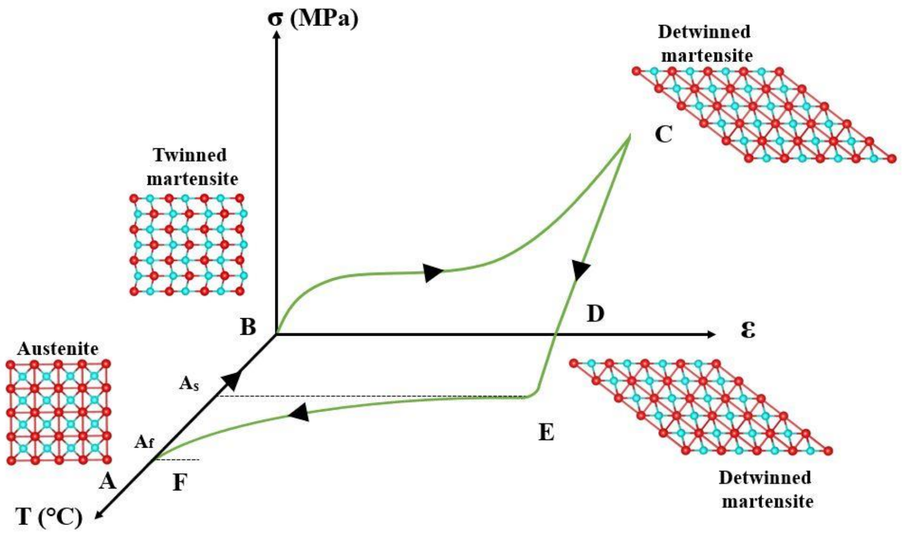

Fig 1.3: SMA Phase Transformation Curve

The transformation cycle starts at point A in the curve, where SMA is in the Austenite phase above the Austenite finish temperature (A_f). As the SMA cools down to Martensite finish temperature (M_f) and reaches point B, its crystal structure changes to monoclinic, and the material becomes twinned Martensite. Only the crystal structure of the SMA changes on cooling, but no visible shape change is observed from A to B. The application of stress at B changes the orientation of monoclinic Twinned Martensite to Detwinned Martensite to reach point C. The stress has to be enough to start the detwinning of SMA. This transformation from Austenite to Twinned Martensite and then to the Detwinned Martensite phase, following path A-B-C in the phase transformation curve, is a forward transformation. The reverse transformation occurs during heating, in which the detwinned Martensite at point C is heated back to point A. The temperature above A_f rearranges the structure to a uniform cubic, i.e., Austenite phase and the SMA regains its original shape before deformation. The simultaneous application and removal of stress and temperature on the SMA results in the desired macroscopic (visible) actuation.

1.3 Thin film deposition for device fabrication

The NiTi SMA bimorph-based mirrors and actuators in this work have been fabricated using thin film deposition techniques. The deposition techniques employed were thermal evaporation and e-beam evaporation techniques which are discussed below.

1.3.1 Thermal Evaporation Technique

It is one of the simplest thin film deposition techniques. It is based on the principle of Joule heating. The deposition process takes place in the vacuum chamber. The vacuum in the chamber is created with the help of two different vacuum pumps. The initial low vacuum of 0.05 mbar can be generated with a rotary pump, while the creation of a higher vacuum is taken care of by a diffusion pump. A minimum vacuum level of 5×10^{-5} mbar is generated for deposition. The source material (NiTi in our case) is put in a tungsten boat inside the vacuum chamber. The tungsten boat is supplied with high power to reach a red-hot condition. At this state, the source material placed in it vaporizes and deposits on the substrate placed vertically above the boat. The film deposition is high-speed and uniform. This technique was used for actuator fabrication since the deposition is not dense enough. Dense films suitable for mirror application were obtained with e-beam deposition, which is discussed next.

1.3.2 E-beam evaporation Technique

This technique utilizes a high-power electron beam to evaporate the source material directly. The requirement and generation of a vacuum in the deposition chamber is similar to that of thermal evaporation. However, the source material is placed here in a graphite crucible for evaporation. A tungsten coil is placed just below the crucible, which is supplied with high power of 3 to 6 kW to generate a high-velocity electron beam. The electron is deflected towards the crucible with the help of beam-deflecting magnets. The electron beam directly interacts with the source material and vaporizes it. Due to the direct heating of the source material, vaporization of high melting point materials is easy, and highly dense films are obtained, which are helpful for mirror applications. Substrate pre-straining and heating were applied with the help of additional fixtures.

1.4Motivation of Thesis

The complexity in design and fabrication is a major limitation of traditional micromirrors and microactuators. The complex design leads to a bulky and rigid assembly, which is challenging. Hence, simplifying the actuation mechanisms and the related manufacturing techniques is of prime concern. The motivation of this work is to develop NiTi SMA thin film-based flexible mirrors and actuators with thermal evaporation and e-beam evaporation techniques. Further, altering the substrate condition before deposition improves the performance of the SMA thin film-based mirror and actuator, including pre-straining of the substrate and laser annealing. Fabrication of a customized flexible actuator is also a challenge which is addressed in this work. Laser-assisted micromanufacturing was employed to cut the bimorph structure into flexible actuators with a single laser stroke. The developed mirrors and actuators will be utilized in a Stewart platform mechanism for laser beam steering applications.

1.5 Objectives of Thesis

The main aim of the thesis is to develop NiTi thin film-based flexible structures as microactuators and micromirrors in opto-mechatronics applications. To achieve this, the following main objective will be addressed.

1. **Influence of substrate pre-straining and heating on the SMA bimorph-based mirror.**
2. **Influence of laser annealing of Kapton polyimide substrate towards bimorph actuator fabrication.**
3. **Laser-assisted micromachining towards actuator fabrication.**

4. **Application of NiTi SMA thin film-based bimorph in the Stewart platform.**

1.6 Significant contribution

The fabricated NiTi/Kapton polyimide structure with different deposition techniques in conjunction with laser-assisted manufacturing is useful as an actuator and mirror. The structure simplifies the fabrication and application of the mirror by eliminating the need for an external actuation mechanism. Further, laser energy can be utilized to convert the same bimorph structure into a customized actuator, such as an optical shutter. The application of SMA bimorph structure in a Stewart platform assembly paves the way for low-power and lightweight assembly for laser beam steering and scanning.

1.7 Organization of Thesis

The thesis is divided into eight chapter as mentioned below:

Chapter 1: Introduction
Provides the general introduction, and background of the topic, motivation, objectives, signification contribution and outline of the thesis.

Chapter 2: Literature Review.
Consist of comprehensive literature survey of NiTi thin film bimorph-based structures with different deposition techniques for actuators and mirror applications.

Chapter 3: Experimental Setup & Theoretical Simulation
Description of deposition techniques and relevant equipment involved in fabrication of bimorph structure and finite element modelling in COMSOL Multiphysics Software to study the tip displacement of the mirror in cantilever configuration.

Chapter 4: Study of fabricated NiTi/Kapton polyimide bimorph-based mirror.
Parametric investigation of process parameter of mirror fabrication on the characteristics of mirror.

Chapter 5: Laser Annealing of Kapton polyimide substrate.

Describes the influence of laser annealing of Kapton polyimide substrate on the properties of thin film-based actuators.

Chapter 6: Laser Assisted Micromachining.
Describes the application laser assisted micromachining on bimorph structures for customized mirror and actuator fabrication.

Chapter 7: Application in Stewart platform arrangement.
Explains the utilization of NiTi SMA based bimorph for fabrication of Stewart platform assembly and application in laser beam steering.

Chapter 8: Conclusion and Scope for Future Work.
Outcome of the work and possible future scope

Chapter 2

This chapter consists of a comprehensive literature survey of NiTi thin film bimorph-based structures with different deposition techniques for actuators and mirror applications

Literature Review

2.1 Shape Memory Alloy based Thin Films

NiTi SMA based thin films have found their applicability both as actuator and mirror in MEMS devices. The NiTi film deposition has been explored in prior literature with different physical vapor deposition (PVD) techniques. These PVD techniques illustrated in fig 2.1, include thermal evaporation, e-beam evaporation, sputtering, ion beam deposition, arc plasma ion plating, plasma spray and pulsed laser deposition[7–13].

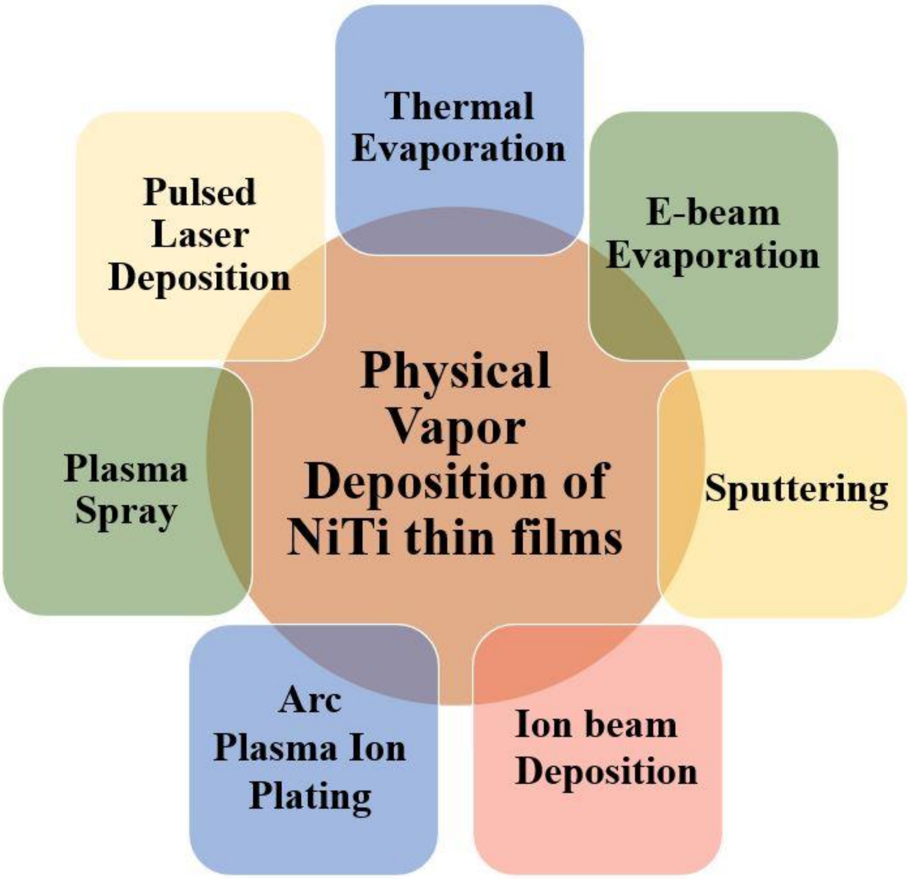

Fig 2.1: PVD techniques used for deposition of NiTi based thin films.

Pulsed laser deposition, ion beam deposition, arc plasma ion plating and sputtering deals with a common issue of low deposition rate and face a difficulty in depositing large area substrates. Also, with sputtering and plasma-based techniques the film density is usually low which is undesirable for mirror application. These issues are taken care in thermal evaporation and e-beam deposition making them suitable for fabrication of flexible bimorph mirrors and actuators. The fabrication of NiTi thin film-based mirrors and actuators with the said techniques have been extensively explored in the literature which is discussed in subsequent sections.

2.2 NiTi Thin Film based Actuators

NiTi thin films have promising applications as microgrippers, microvalves, micro robots, thermal switches and other MEMS applications owing to their large force and displacement generated compared to the other mechanisms. Both binary and ternary NiTi alloys have been utilized for microactuator fabrication through thermal evaporation and e-beam evaporation technique. Different NiTi binary and ternary NiTi SMA thin film-based actuators are illustrated in figure 2.2. T. Mineta et al. have fabricated NiTi and NiTiCu thin film based microactuators on copper substrate as shown in figure 2.2 (a), with flash evaporation technique[14]. The copper substrate was dissolved in HNO_3 post annealing and spring actuators with 18 µm and 33 µm thickness were developed which were able to produce the elongation percentage of 20 to 100% with a generated force of up to 80 mN. Makino et al. fabricated a micropump by depositing a 6 µm thick NiTi film on Si substrate using flash evaporation illustrated in figure 2.2 (h) [15]. NiTi thin film was used as a diaphragm for operation of the micropump in pressurization and evacuation modes. The SMA actuator produced a maximum displacement of 95 µm at the centre with a pressure of 200 kPa. Recently, Jayachandran et al. in year 2021 developed an NiTi SMA thin film bimorph-based belt for waste heat energy harvesting[16]. Figure 2.2 (c) illustrates the bimorph -based belt structure in which NiTi film was deposited on a Kapton polyimide belt of size 45 cm x 2 cm using flash evaporation. The thickness of the substrate was 50 µm. The Kapton belt was held in a customized substrate which can rotate the belt at 20 rpm while deposition. The heat energy was harvested using a two-pulley system connected by the bimorph belt and the maximum energy harvested was 75 %. In another study by the same research group, P Karna et al. investigated the capability of the NiTi bimorph actuator towards laser- based actuation[17]. They fabricated the bimorph structure on a 50 µm Kapton polyimide substrate using thermal evaporation. The non-contact based actuation was affected using a 50 W fiber laser at varying laser power, scanning speeds and number of passes displayed in fig 2.2 (d).

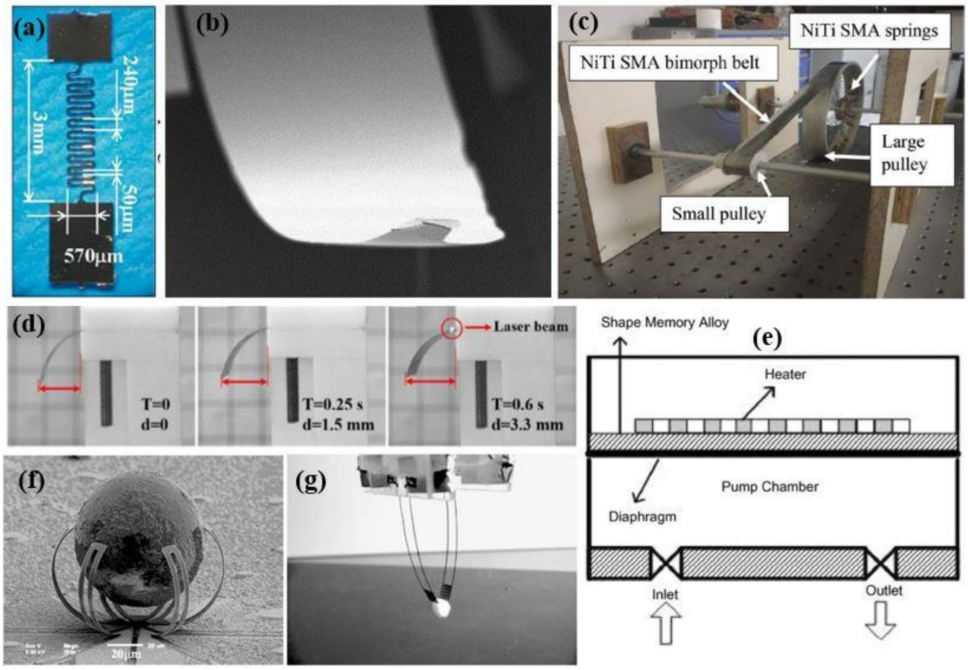

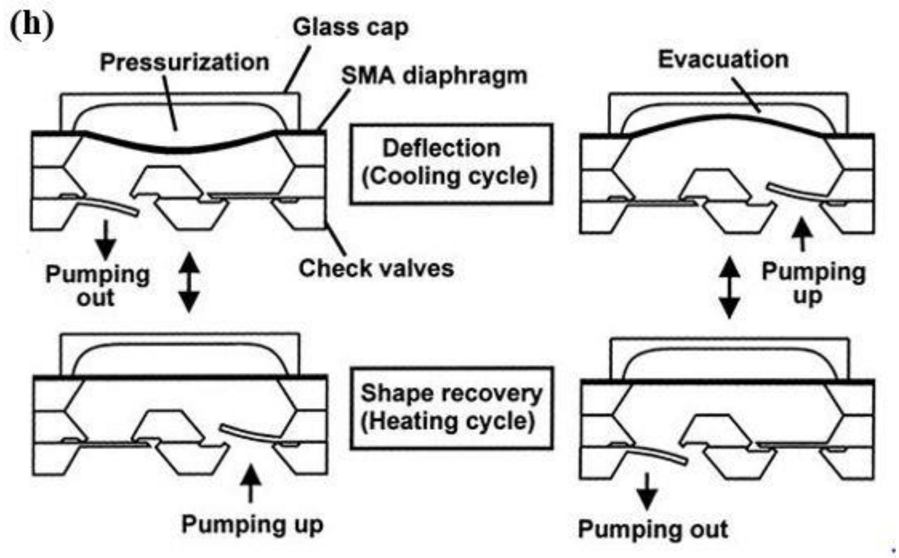

Fig 2.2: NiTi SMA thin film-based actuators[14–20].

Thermal evaporation technique deals with an issue of loss of Ti in the deposited film compared to the source material due to difference in vapor pressure of Ni and Ti. This issue was addressed by Adams et al. where they deposited NiTi thin film on SiO_2 coated Si wafer by co-evaporation[18]. Ni was evaporated by thermal evaporation while electron beam was used for evaporation of Ti simultaneously. Photoresist was used to separate NiTi film from SiO_2 to produce freestanding NiTi actuator with a thickness of about 1 μm exhibited in fig 2.2 (b). Narayane and Taiwade fabricated NiTi SMA thin film-based actuator using e-beam evaporation[21]. They fabricated bi-layer and tri-layer sandwich structure composite for soft robotics applications in a three-arm gripper shown in fig 2.2 (f) and (g).

2.3 NiTi Thin Film based Mirrors

Binary and ternary NiTi alloy based thin films have been extensively studied for micromirror applications. Rigid as well as flexible mirrors have been fabricated for various opto-mechatronics applications. Generally used micromirrors use reflective surfaces such as Si for mirror substrates and their reflectivity was increased by depositing different reflective films. The SMA thin film have mostly been employed in actuation mechanisms of such mirrors. Y Q Fu et al. have shown the applications of NiTi thin films-based mechanisms for mirrors. Different configurations such as single and multiple cantilevers, and four arms have been investigated for NiTi/Si and NiTi/Si_3N_4 mirror structures as shown in fig 2.3 (a), (b) and (c). Jayachandran et al. have explored the capability of e-beam evaporation towards mirror fabrication[12]. Kapton polyimide substrate of thickness 50 µm was deposited with a 40 µm NiTi film to attain the mirror structure. The fabricated mirror has shown high reflectivity in visible range which can be utilized in interferometry applications with the setup displayed in fig 2.3 (d).

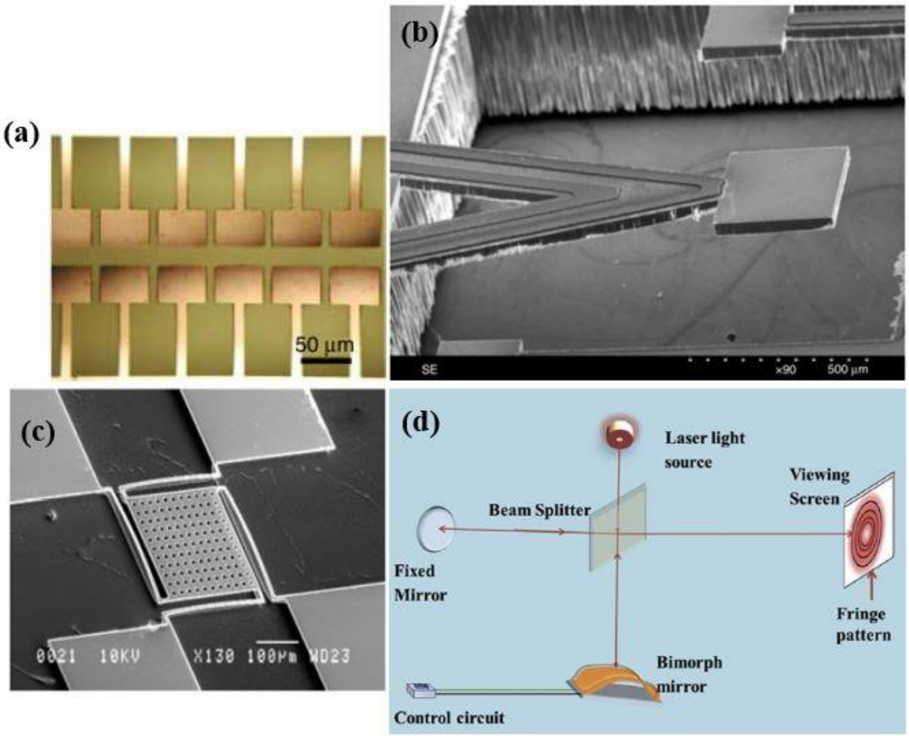

Fig 2.3: NiTi SMA thin film-based mirrors[12,22].

2.4 Laser Processing

2.4.1 Laser Annealing

The fabrication of NiTi/Kapton polyimide bimorph was attempted using methods including sputtering, thermal evaporation and e-beam evaporation. Despite applying a wide range of deposition methods and promising actuation characteristics offered by NiTi/polyimide bimorph, issues such as less film adhesion on the substrate and inadequate deposition limit its applicability. The wettability of Kapton polyimide is less, which brings about the mentioned issues. Various techniques, such as substrate preheating, in situ heating, bimorph annealing, and laser treatment, have been explored to resolve the issues. Along similar lines, the laser annealing of polyimide before the deposition process can be an effective technique. Laser annealing causes surface modifications in polyimide, which can be favourable for better deposition characteristics.

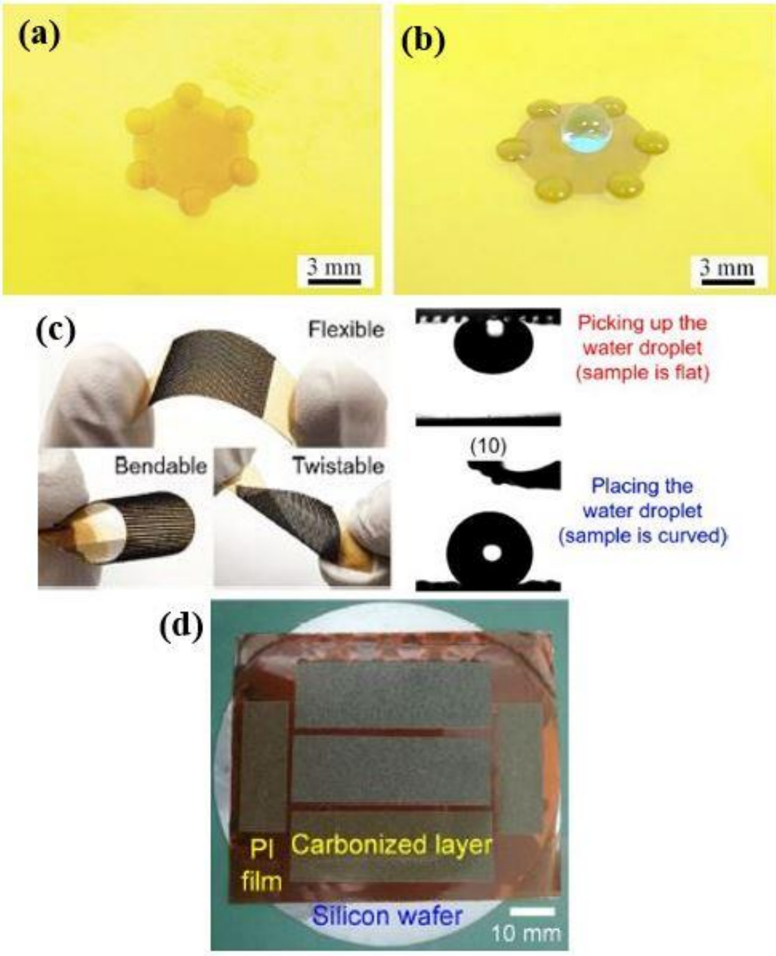

Fig 2.4: Laser treated Kapton polyimide films for improved hydrophilicity and hydrophobicity.

The effects of laser irradiation on the surface properties of polyimide have been studied in the past. The effects of 1064 nm pulsed Nd: YAG laser on the morphology and wettability of polyimide were explored by Liu et al[23]. Nam et al. studied the polyimide surface's wetting characteristics after treatment with a 10.6 μm CO_2 laser[24]. They demonstrated the generation of graphene on polyimide, which led to an increment in the hydrophobic nature of the polyimide surface shown in fig 2.4 (c). Furthermore, the wettability change of the polyimide surface was examined by Hiraoka and Lazare, where polyimide was irradiated with 185 nm and 254 nm KrF UV laser[25]. Z Ball et al. have investigated the effects of multi-spot irradiation of KrF laser on polyimide's electrical conductivity and ablation characteristics[26]. High absorptivity of UV wavelength by polyimide generally results in photoablation and carbonization, thereby reducing the substrate thickness[27–29]. Near UV wavelengths, such as 355 nm, have lesser absorption in the polyimide, leading to variation in surface modification depending on the laser fluence. Du et al. have studied the effects of various laser intensities and overlap of 355 nm Nd: YAG laser on the hydrophobicity of the polyimide shown in fig 2.4 (a) and (b) [30]. Low laser intensities form micro stripes that result in an increase in hydrophobicity surface with pulse overlap. However, high laser intensities resulted in microgroove formation, which produced a superhydrophilic surface.

2.4.2 Laser Assisted Micromachining

Laser assisted micromachining of thin films has been explored in past studies for patterning and channel formation. Laser machining of CuAlFeMn quaternary shape memory alloy using a CO_2 laser was investigated by S. Santosh et al[31]. They have successfully demonstrated the retention of shape memory effect after laser machining with variation in transformation temperatures. An optimal combination of laser power, cutting speed, stand-off distance and gas pressure was determined for higher material removal rate and lower surface roughness. Pfleging et al. utilized a 248 nm excimer laser for ablation of passivating silicon nitride, $Tb_{0.4}Fe_{0.6}/Fe_{0.5}Co_{0.5}$ and $Fe_{0.6}Co_{0.4}/SiO_2$ layer coated on silicon wafer[32]. This resulted in passivation properties in the non-ablated region and bulk properties of silicon in the ablated region for solar cell applications.

In another study, laser beam machining of silicon wafers was attempted by Daemi et al. to study the precision of micromachining of the machines[33]. Furthermore, the removal of fragile silicon substrate was also tried to achieve a freestanding micromachined structure. NiTi and TiN films deposited on silicon wafers were micromachined using a femtosecond laser, and then the silicon substrate was etched off to produce freestanding SMA actuators and microheaters revealed in fig 2.5 (a) and (b) [34]. Fiber laser has also been utilized to micromachine thin NiTi tubes for the fabrication of vascular stents by Liu et al. [35]and stainless-steel sheets of 1 mm thickness for biomedical applications by Panigrahi and Patel as shown in fig 2.5 (e) and (f) [36]. In another study, C. Leone et al. have demonstrated the cutting of CFRP sheet by multi passes in a complex structure as shown in fig 2.5 (d) [37]. 3D MEMS structures have also been fabricated using fiber laser by Serap Celen[38]. Figure 2.5 (c) illustrates the laser micromachined MEMS structure fabricated on titanium sheet.

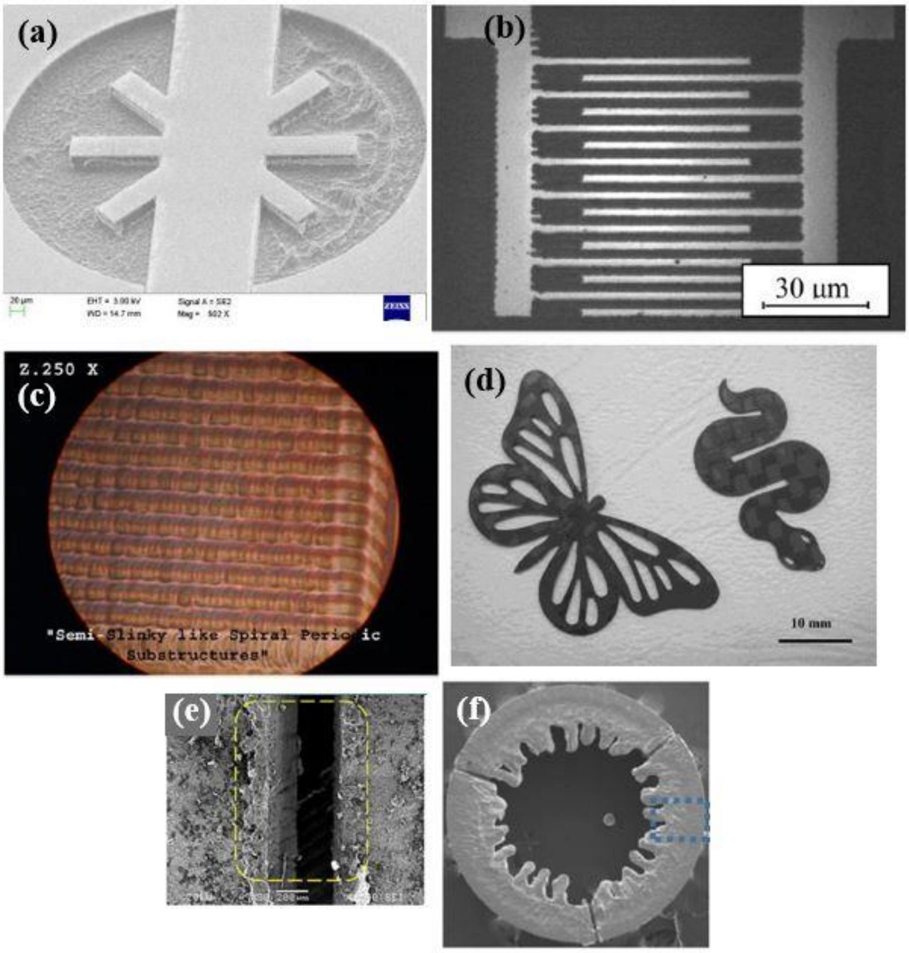

Fig 2.5: Laser assisted micromachined thin films for various applications[34–39].

2.5 Modelling of SMA thin films

The miniaturized form of NiTi in thin film structures allows for integration into micro-scale systems, but also introduces unique mechanical and thermal behaviours due to size constraints, surface effects, and interaction with substrates. Consequently, accurate simulation of their actuation behavior under thermal and mechanical loads is essential for effective design and performance prediction. Several modelling strategies have been explored in the past to simulate the complex thermomechanical behavior of NiTi SMA thin films. Among these, phenomenological constitutive models are widely used due to their ability to capture key characteristics such as the shape memory effect, pseudo elasticity, and hysteresis. Modelling of thin films are based on models used for simulation of bulk or wire. Auricchio et al. introduced three-dimensional constitutive models for SMAs to predict phase transformation under mechanical and thermal loading[40]. These models simulate pseudoelastic behavior as well as thermal-induced shape recovery. Similarly, the models developed by Lagoudas and co-workers incorporate internal state variables to track martensite volume fraction and transformation history[41,42]. These models are thermodynamically consistent and capable of simulating rate-dependent and cyclic behavior under coupled thermal-mechanical loading. Ozturk and Bhattacharya have studied the thermal response of NiTi SMA thin films with layered microstructures under different geometries using numerical simulations[43]. The study analysed the influence of geometry, heat source intensity and spacing on temperature evolution and phase transformation. The study gives an understanding about optimization of thermal response of SMA thin films; however, the application towards actuator application was lacking. The performance of NiTi thin film as a composite actuator was studied by Sun and Jiang. They simulated NiTi/Si composite actuator in ANSYS and studied the phase transformation and deflection of the actuator with temperature[44]. These studies can be extended to understand the actuation behavior and designing of NiTi/Kapton polyimide thin film-based actuators. Furthermore, the performance prediction of these actuators will facilitate beneficial for device fabrication towards opto-mechatronics applications.

2.6 Thermomechanical Properties of SMA thin films

The actuation performance and reliability of the shape memory alloy thin film-based actuators depend on their thermomechanical properties. which are strongly influenced by film's composition, microstructure and fabrication method[45,46]. The thermal properties include transformation temperatures, thermal conductivity and specific heat of the SMA film. The key transformation temperatures signifying phase change in the SMA film are Martensite start temperature (M_s), Martensite finish temperature (M_f), Austenite start temperature (A_s) and Austenite finish temperature (A_s). These temperatures provide the information about the temperature window of the actuation of the film. These temperatures are tunable based on their composition, processing, annealing and ageing of the film[47]. **Table 2** provides information about transformation temperatures for different SMA compositions.

Table 2: Transformation temperatures of different SMA thin films

Composition	M_s (°C)	M_f (°C)	A_s (°C)	A_f (°C)
NiTi[48]	50	20	65	120
NiTiCu[49]	53.8	8.3	73.1	113.5
CuAlMn[50]	-39	-52	-26	-12

Thermal conductivity and specific heat of the SMA films also play important roles in determining response time, energy efficiency and heat dissipation for operation at high frequency and input power. SMA thin films exhibit large recoverable strains up to 8% which makes them attractive alternative for scientific community as a high displacement actuator. Strain recovery is the foremost mechanical property defining the application for SMA thin films. High strain recovery enables efficient and repeatable actuation of the microactuator with high energy density. Moreover, SMA thin film exhibit high fatigue resistance, which makes them appropriate choice for applications requiring long cycle times. Lastly, surface quality and microstructure including grain size, texture, and defect density strongly influence the reproducibility and stability of thermomechanical behavior. These, in turn, are governed by deposition methods (e.g., sputtering, thermal deposition) and post-deposition heat treatments[11,51–53].

2.7 Summary

This chapter discusses the prior art studies pertaining to different applications of NiTi thin films as actuators and mirrors and their fabrication using deposition and laser processing techniques used in this work. NiTi films deposited with both thermal evaporation and e-beam evaporation have shown promising applications as actuators as well as mirrors. Free standing NiTi films have been used as springs, diaphragm for micropumps and microgrippers. The bimorph structure has also been explored as actuator for microgrippers and heat energy harvesting belt. For mirrors, NiTi thin films has mostly been used as supporting mechanisms however, the e-beam deposited film on Kapton polyimide substrate was explored and proof of concept was shown as a mirror structure.

Literature have also delved into the laser-based manufacturing for polyimide and other thin films. Laser energy has been used for treatment of polyimide surface to alter its hydrophobicity and hydrophilicity based on the requirements. High ablation has been achieved with UV and near-UV wavelength lasers, however, high wavelength CO_2 lasers are useful for graphene formation. Thus, for laser annealing we have opted for ear-UV 355 nm Nd: YAG laser which can create high roughness for better film deposition and adhesion. Lasers are effective in micromachining of thin films ranging from polymers to metal alloys. NiTi films have been micromachined in the past for micro wrappers, vascular tubes and microheater applications. Also, various polymers have been micromachined using low power fiber lasers. However, literature regarding laser micromachining of bilayer structure was not available. In this regard, we have investigated the process capability of a 1064 nm fiber laser for micromachining of Niti/Kapton polyimide bimorph structure for fabrication of customized actuators such an optical shutter.

Chapter 3

This chapter describes the methodology and relevant equipment involved in fabrication of bimorph structure and finite element modelling in COMSOL Multiphysics Software to study the tip displacement of the mirror in cantilever configuration.

Experimental Setup and Theoretical Simulation

3.1 Methodology

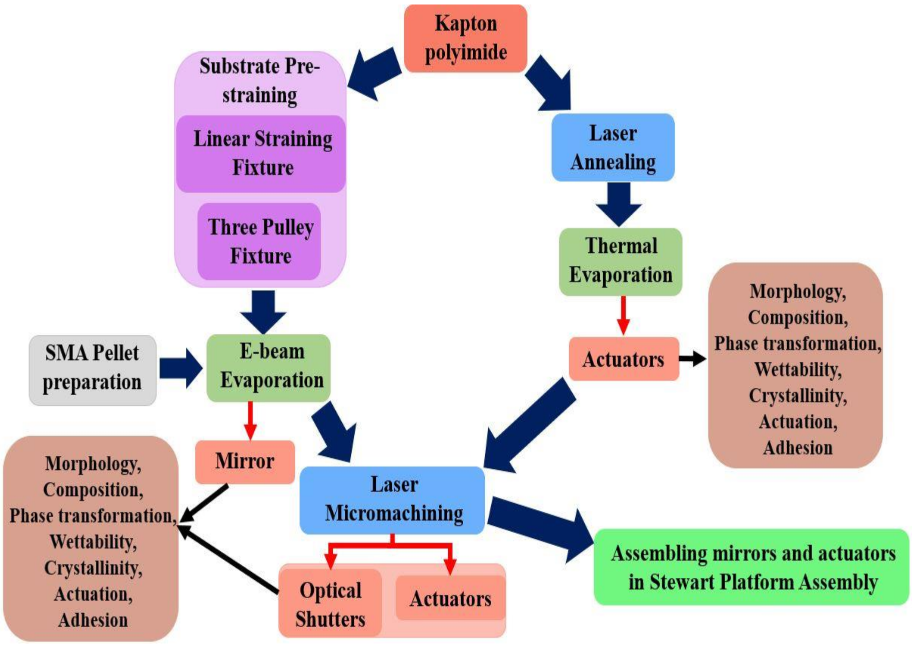

Fig 3.1: Methodology adopted for mirror and actuator fabrication in this work

The fabrication of the flexible mirrors and actuators in this work has followed the methodology shown in the fig 3.1. For mirror fabrication, thin film of NiTi was deposited on Kapton polyimide in pre-strained condition. The deposition was performed in e-beam evaporation unit. The pre-straining has been applied with the help custom fabricated fixtures. The open belt was pre strained by linear straining fixture discussed in section 4.3.1. The closed belt of Kapton polyimide was pre-strained in a three-pulley arrangement shown in section 4.1.1. NiTi pellet was prepared in vacuum arc melting and then supplied to e-beam unit for deposition process. The fabricated structure had mirror finish was which characterized for different properties as a mirror. Also, the same structure can be micromachined using fiber.

In another method, laser energy was used to anneal the surface of Kapton polyimide before deposition. The annealed substrate was deposited with thermal evaporation technique for actuator fabrication. The fabricated actuators were tested for structural and functional characteristics. Further, the actuators can be micromachined with fiber laser for customized actuator fabrication. The relevant thin film deposition and laser processing techniques are discussed further in this chapter.

3.2 Pellet Fabrication

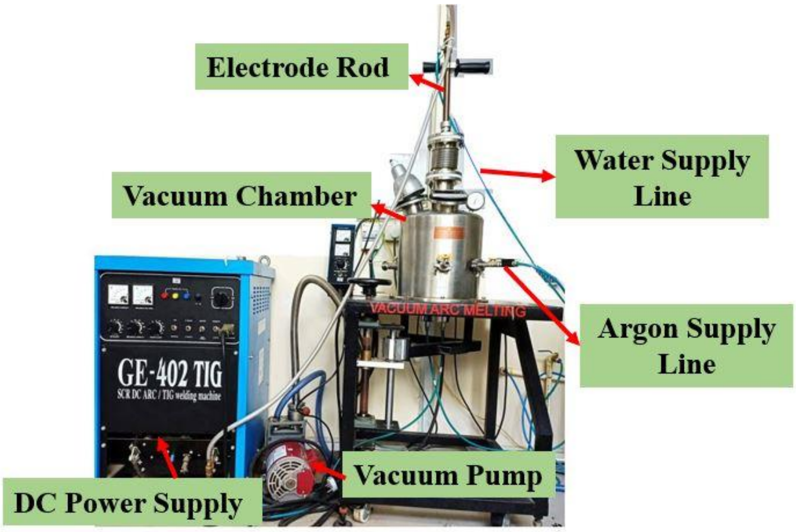

Fig 3.2: Experimental setup for fabrication of NiTi pellets to be utilized in deposition.

For composition control of binary and ternary NiTi alloy after deposition, the composition of the source material needs to be adjusted properly. This adjustment can be done by adding the input materials in measured quantity and converting them into a single pellet. This process was done with a vacuum Arc Melting unit illustrated in figure 3.2. Wires and flakes can be added in a copper crucible where pellet formation takes place. The crucible is a part of a vacuum chamber in which a vacuum was created with the help of rotary pump. Then argon gas was supplied in the chamber to provide an inert atmosphere inside the chamber. The power to generate electric arc was supplied through the electrode rod powered by a DC power supply. The tungsten electrode held in the electrode rod generates the electric up to a certain distance from the copper crucible. The remelting and solidification of the pellets were done thrice to homogenize the composition of the pellet.

3.3 Thin Film Fabrication

3.3.1 Thermal Evaporation

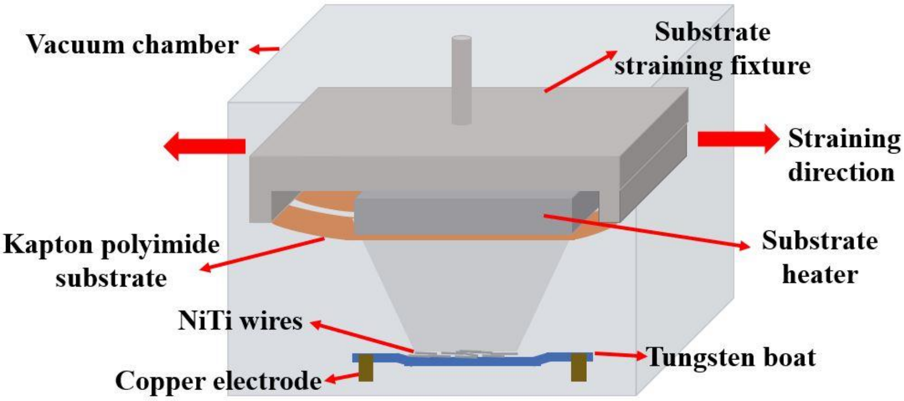

Fig 3.3: Schematic of thermal evaporation technique for NiTi thin film deposition

NiTi SMA thin film was deposited on laser-annealed substrates using the thermal evaporation technique (Thermal deposition unit- Hydro Pneo Vac Technologies) shown in figure 3.3. The chamber has the provision for accommodating different substrate holders as per the substrate and application required. For Kapton polyimide substrate, plain flat substrate holder, and two different pre-straining holders were available. For deposition in belt form, the substrate was a three-pulley arrangement where strain can be applied by moving the pulley. In another fixture, polyimide substrate can be held in linear form and strain can be applied. Pre-strain was applied so that after deposition when the bimorph is removed from the fixture, the elastic recovery of the polyimide generates strain in the deposited NiTi film. The strain is helpful in improving SMA and actuation characteristics of the bimorph. The deposition process was carried out in the chamber pressure of 5 x 10^{-5} mbar, which was created using a rotary pump and diffusion pump. The source to substrate distance and the deposition time varies depending on the source and substrate material.

3.3.2 E-beam Evaporation

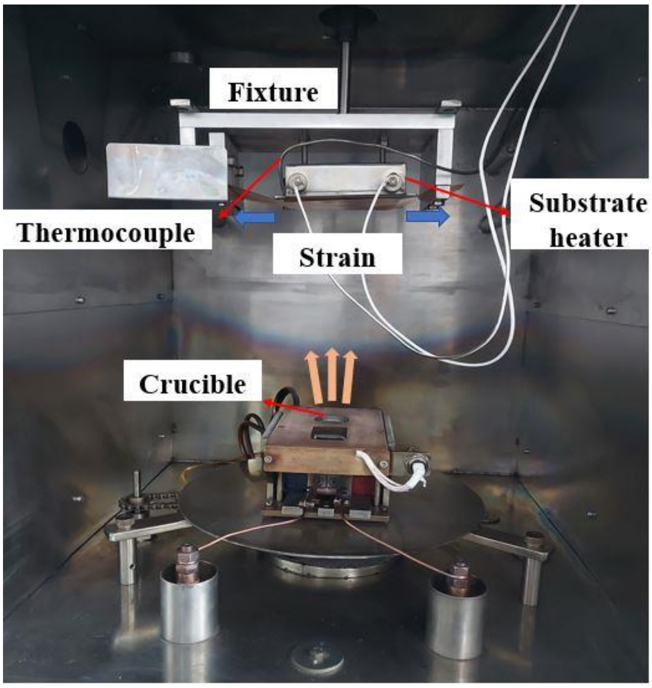

Fig 3.4: E-beam evaporation technique for NiTi thin film deposition

The thin film of NiTi shape memory alloy (SMA) was deposited on Kapton polyimide substrates by utilizing the E-beam evaporation technique (Hydro Pneo Vac Technologies) shown in figure 3.4. The Kapton polyimide substrate of thickness 75 μm was held in the deposition chamber with the help of substrate holders mentioned in the previous section. The deposition was performed in the chamber with a 2 x 10^{-5} mbar pressure. The source material can be NiTi wires or pellets fabricated in Vacuum Arc Melting discussed in next section. The source material was placed in a graphite crucible for deposition. The tungsten coil was supplied with high power to generate the electron beam. The generated electron beam was directed to the source material in the graphite crucible with the help of beam-deflecting magnets. The deposition time varies depending on the energy supplied to the tungsten coil and the thickness of the film required.

3.4 Laser Assisted Manufacturing

3.4.1 Laser Annealing of Substrate

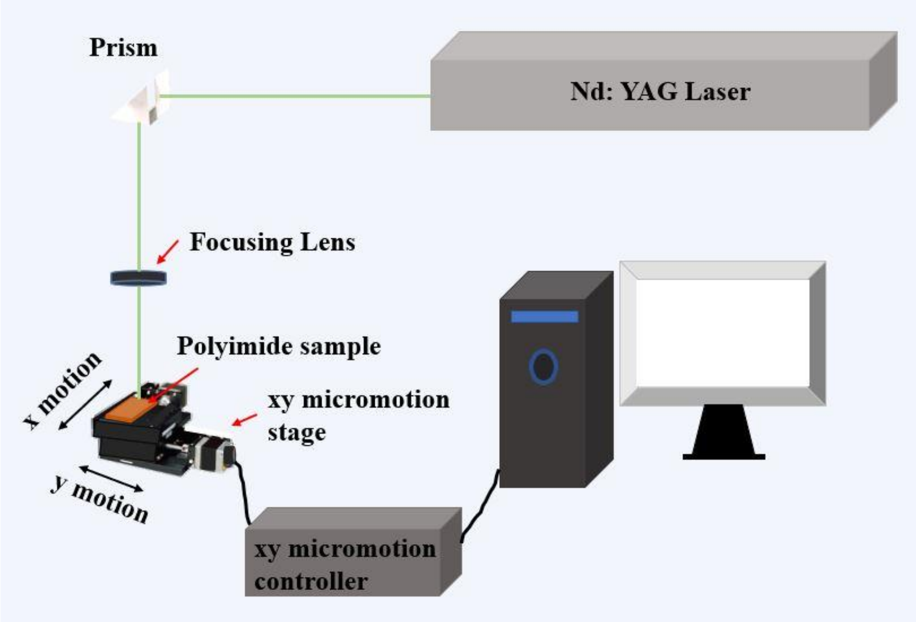

Fig 3.5: Schematic for laser assisted annealing of Kapton polyimide substrate.

Kapton polyimide substrates of size 75 mm x 44 mm were laser annealed using Nd: YAG laser (Spectra-Physics- Quanta Ray). The laser wavelength used for annealing was 355 nm, which is near the UV range. The polyimide substrates were pasted on glass slides to flatten the natural curvature of polyimide during the laser annealing performed on the setup shown in fig 3.5. The laser annealing was performed at laser fluences of 500 mJ/cm^2, 1000 mJ/cm^2, 1200 mJ/cm^2, and 1630 mJ/cm^2 with a line % LO of 50%, 70%, and 90%. The laser pulse energy has a Gaussian profile; thus, for uniformity of the laser modifications throughout the sample surface, the laser spot has to be applied in an overlap condition. This has to be achieved by controlling the speed of the stage in both the x and y directions. The overlap between the consecutive laser spots is the spot overlap (in the x direction), and the overlap between the consecutive line patterns in the y direction is the line overlap (% LO). A constant spot overlap of 95% was applied in all the laser annealing samples.

3.4.1 Laser Assisted Micromachining

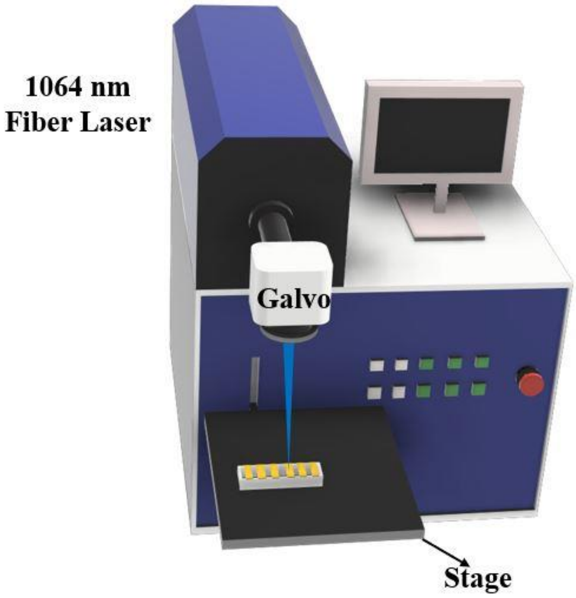

Fig 3.6: Schematic for laser assisted micromachining of NiTi/Kapton polyimide bimorph.

The bimorph structure was pasted on 3D printed structures of dimensions 24 mm x 100 mm x 10 mm with a wall thickness of 2 mm for laser micromachining with the setup shown in fig 3.6. The laser micromachining was performed using a 1064 nm fiber laser (Scantech laser) with a focused spot size of 50 µm. The maximum power output of the laser was 50 W. The laser head is equipped with a focusing lens and a galvo. The motion of the laser beam is controlled by galvo as per the input fed. A single line cut was attempted using varying laser power (LP), laser speed (LS), spot diameter (SD), and laser travel direction (LT) to determine the optimized micromachining parameters. As the laser performs micromachining in a raster scan pattern, the study was attempted by employing transverse and longitudinal directions of laser travel. The laser scanning of the bimorph in a raster pattern was considered to be in the transverse direction of laser travel. Furthermore, when the laser scanning direction was perpendicular to transverse, it was termed the longitudinal direction of laser travel. It was termed longitudinal as only a single line scan was achieved.

3.5Simulation of electrical actuation

3.5.1 Model geometry and Material Properties

The 3D model of NiTi/ Kapton polyimide bimorph was developed in COMSOL Multiphysics software with NiTi film of thickness 1.3 μm assembled on top of Kapton polyimide substrate of 75 μm[54,55]. Figure 3.7 (a) illustrates the flowchart of the process followed for the simulating the electrical actuation of bimorph structures fabricated at varying strains. The size of the bimorph structure considered for simulation was 4 cm x 2 cm, which was the sample size used for the experimental study of electrical actuation. The Kapton polyimide substrate was applied with different pre-strain conditions along the length. The bimorph was in a cantilever configuration such that its bottom edge is fixed and top edge is free for actuation. An electric current was supplied using point contacts at the fixed end on the NiTi film. The electric current of 0.25 A was provided across the terminal points that were the maximum current drawn by the bimorph during the experimental study.

(a)

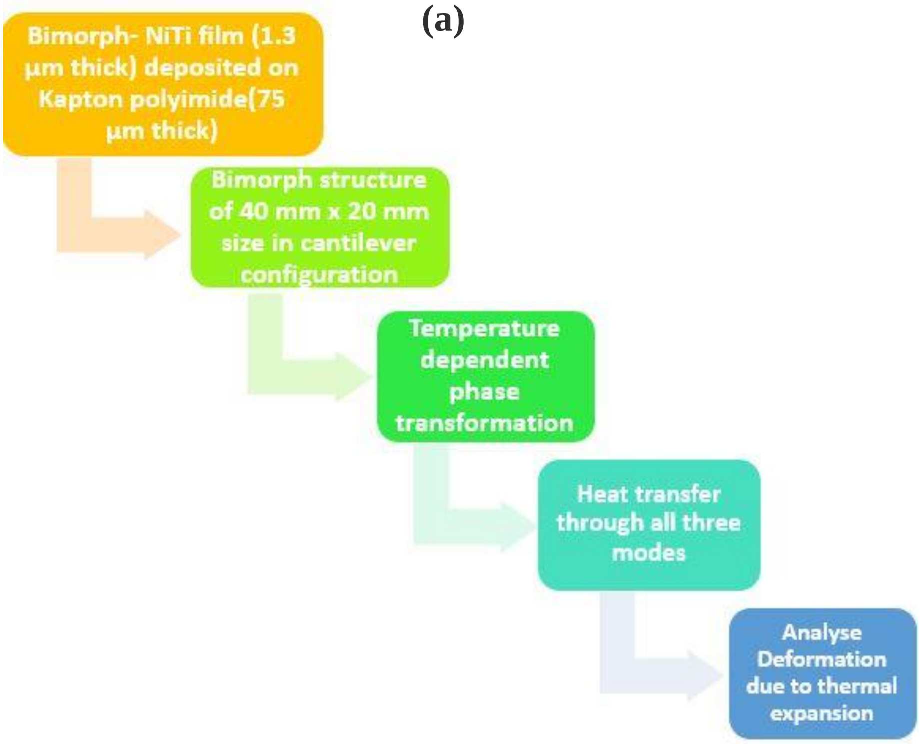

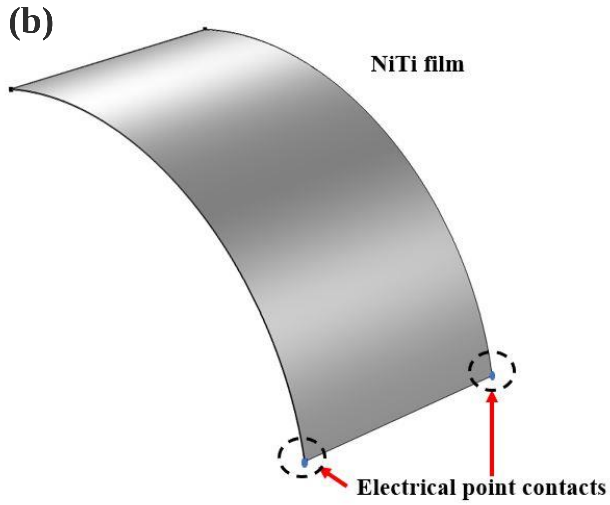

Fig 3.7: (a) Flowchart for simulation of electrical actuation of NiTi/Kapton polyimide bimorph-based mirror in cantilever configuration. (b) bimorph actuator with electrical contacts for the supply of electric current.

The electrical contacts were provided as point contacts on the vertices of the fixed edge of NiTi film (encircled blue dots) as shown in fig 3.7 (b). The NiTi film heats up due to Joule heating and the top end of the bimorph actuates according to the thermal expansion equation. The Physics applied to the geometry for heating was electromagnetic heating while actuation was studied by thermal expansion Physics in COMSOL Multiphysics. The thermal expansion of both NiTi and Kapton polyimide substrate depends on coefficient of thermal expansion of both materials and the current temperature of the bimorph structure. The solid-state phase change in the NiTi film was characterized by Martensite volume fraction (ξ) which varies with temperature according to equation 1 in section 3.5.2. The coefficient of thermal expansion of NiTi (α_n) was also considered linearly varying with Martensite volume fraction as per equation 2. The variation in coefficient of thermal expansion of NiTi thin film and increment in temperature induces strain in the bimorph structure. This strain is translated into the actuation of free end of bimorph. The heat generated in the NiTi film travels via three modes i.e. conduction, convection and radiation. The relevant equations are mentioned in section 3.5.2. This heat transfer results in reverse phase transformation of NiTi and actuation during heating cycle while forward phase transformation of NiTi and cooling of bimorph during cooling cycle. The material properties for NiTi and Kapton polyimide considered for simulation are listed in table 3. The geometry was meshed using sweep mesh. Further phase transformation and heat transfer governing equations along with the boundary conditions are discussed in the next section.

Table 3: Properties of NiTi/polyimide bimorph

Parameters	NiTi	Polyimide
Youngs Modulus	Martensite phase E_M= 30 GPa Austenite phase E_A= 83 GPa	2.5 GPa
Density	6450 kg/m^3	1420 kg/m^3
Thermal conductivity	Martensite phase σ_M =8.6 W/mK Austenite phase σ_A =18 W/mK	0.20 W/mK
Poisson's ratio	0.33	0.34
Coefficient of thermal expansion	Austenite phase α_A=11 x 10^{-6} 1/K Martensite phase α_M=6.6 x 10^{-6} 1/K	20 x 10^{-6} 1/K
Surface Emissivity	0.15	0.80
Specific heat at constant pressure	837.36 J/kgK	1090J/kgK

3.5.2 Assumptions and Boundary Conditions

Following assumptions were made for carrying out the simulation study of the electrical actuation of bimorph:

1. Adhesion between NiTi and Kapton is perfect, with no film porosity.
2. Film thickness is uniform throughout, and the film is electrically continuous in all conditions.

3. No spring back in Kapton.
4. Heat is transferred through all three modes.
5. Kapton substrate is not decomposing at higher temperatures.

Certain material properties of NiTi thin film were temperature-dependent which were considered to vary linearly with temperature during the reverse phase transformation. The related equations are given below[56]:

Martensite volume fraction:

$$\xi = \begin{cases} 1 & ; T \leq A_s \\ \left(\frac{A_f - T}{A_f - A_s}\right) & ;\ A_s < T < A_f \\ 0 & ; T \geq A_f \end{cases} \quad \ldots\ldots(1)$$

A_f – Austenite finish temperature (°C), A_s – Austenite start temperature (°C), T – Instantaneous temperature of the film (°C). A_s and A_f for each model were taken from the obtained values from the DSC results.

Coefficient of thermal expansion:

$$\alpha_n = \begin{cases} \alpha_M & ; T \leq A_s \\ \xi.\alpha_M + (1-\xi)\alpha_A & ;\ A_s < T < A_f \\ \alpha_A & ;\ T \geq A_f \end{cases} \quad \ldots\ldots\ldots\ldots\ldots\ldots(2)$$

α_n - Coefficient of thermal expansion for NiTi film at any temperature (1/°C), α_M – Coefficient of thermal expansion for Martensite phase (1/°C), α_A – Coefficient of thermal expansion for Austenite phase (1/°C).

Thermal conductivity:

$$k_n = \begin{cases} k_M & ;\ T \leq A_s \\ \xi.k_M + (1-\xi)k_A & ;\ A_s < T < A_f \\ k_A & ;\ T \geq A_f \end{cases} \quad \ldots\ldots\ldots\ldots\ldots\ldots(3)$$

k_n – Thermal conductivity for NiTi at any temperature (W/mK), k_M – Thermal conductivity for Martensite phase (W/mK), k_A – Thermal conductivity for Austenite phase (W/mK).

The heat generated was transferred via the three modes given below:

1. Conduction within NiTi and Kapton polyimide and conduction from NiTi to Kapton polyimide.
2. Convection from all the surfaces to the ambient air.
3. Radiation from all the surfaces to the ambient air.

The heat transfer via the above-mentioned modes in COMSOL Multiphysics follows the equations given below:

Conductive heat transfer:

$$\boldsymbol{q_1 = -(k_{p}.\nabla T + k_n.\nabla T)}\text{.......... (4)}$$

k_p - Thermal conductivity of Kapton polyimide (W/mK), k_n - Thermal conductivity of NiTi (W/mK), q_1 - conductive heat transfer per unit area (W/m^2), and ∇T- Temperature gradient in space (K/m).

Convective heat transfer:

$$\boldsymbol{q_2 = h_a(T - T_{amb})}\text{.........(5)}$$

h_a – Convective heat transfer coefficient of air (20 W/m^{2}K), T_{amb} - Ambient temperature (20 °C) and T-Temperature of the outer surface of the bimorph, and q_2 - convective heat transfer per unit area (W/m^2).

Radiative heat transfer:

$$\boldsymbol{q_3 = \varepsilon_k \sigma\left(T_k^4 - T_{amb}^4\right) + \varepsilon_n \sigma\left(T_n^4 - T_{amb}^4\right)} \text{ ... ... (6)}$$

ε_k - Emissivity of the surface of NiTi film, ε_n - Emissivity of the surface of Kapton polyimide, T_{amb} - ambient temperature (20 °C), T_k *and* T_n - surface temperature of Kapton polyimide and NiTi respectively (°C), σ = Stefan Boltzmann constant (5.67 x 10^{-8} W/m^{2}K), and q_3 = radiative heat transfer per unit area (W/m^2).

Thermal expansion equation:

The different coefficients of thermal expansion for Kapton polyimide and NiTi resulted in different thermal expansion of both materials. The final strain generated in the bimorph is the equation given below:

$$\boldsymbol{\epsilon = \alpha_n(T_n - T_{amb}) - \alpha_k(T_k - T_{amb})} \text{ ... . (7)}$$

α_k - Coefficient of thermal expansion for Kapton polyimide (1/°C), α_n - Coefficient of thermal expansion for NiTi (1/°C), T_k *and* T_n - current temperature of Kapton polyimide and NiTi respectively (°C). The different thermal expansions of both layers of bimorph will develop a net displacement at the free end of the bimorph. The polyimide substrate was assumed to be under the influence of pre-strain for theoretical calculations. The unstrained, 1% pre-strained, and 3% pre-strained conditions were considered by applying initial strain on the substrate. The NiTi film was considered free of pre-straining conditions in the simulation.

3.5.3 Influence of pre-straining of substrate

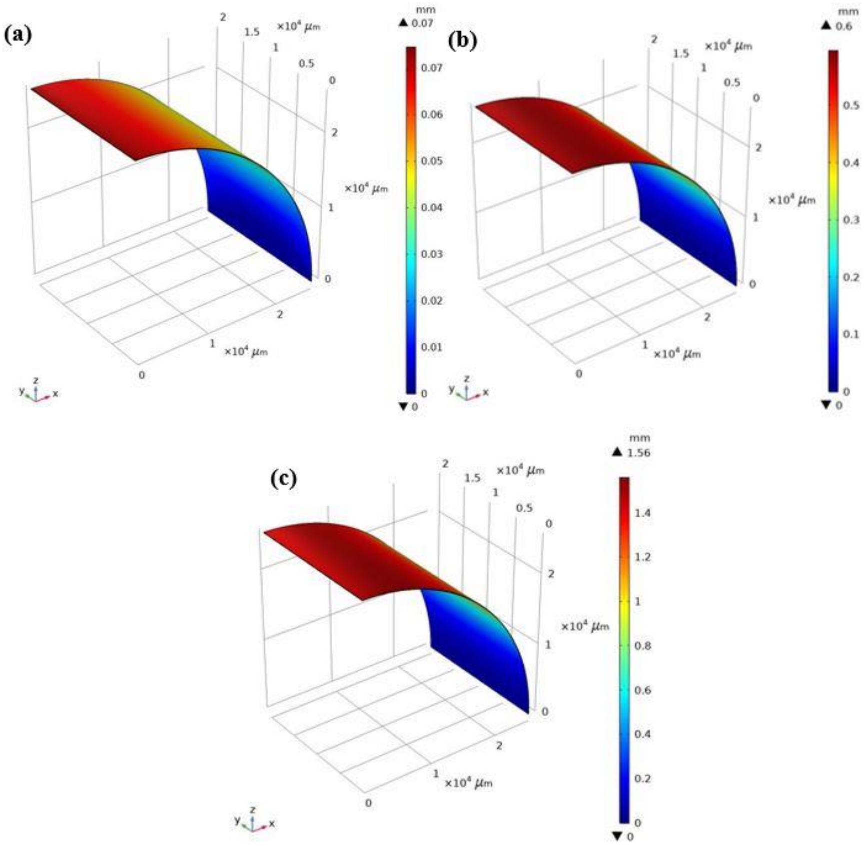

Fig 3.8: Simulated tip displacements of the SMA bimorph mirrors at varying pre-strain condition of the substrate.

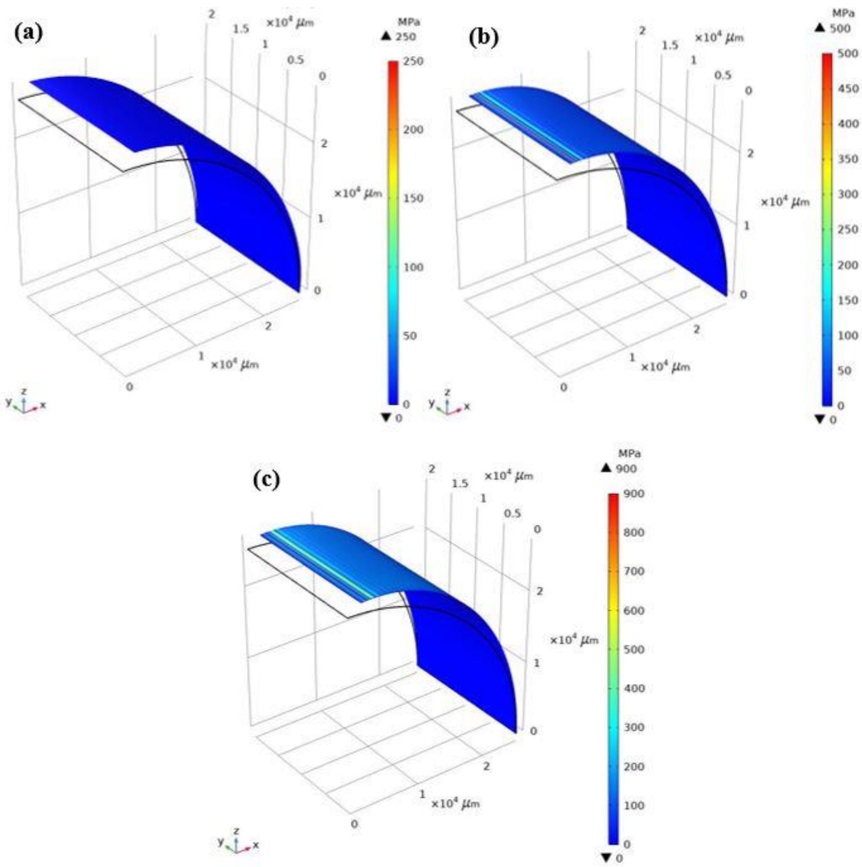

Fig 3.9: Simulated stresses generated on the SMA bimorph mirrors at varying pre-strain condition of the substrate.

The simulated results suggest that increasing the pre-strain on the substrate increases the tip displacement. The unstrained bimorph showed a tip displacement of 69.5 μm which increased to 162 μm for 3% pre-straining, as shown in fig. 3.8. The simulated models were considered to have no spring back or strain recovery, which resulted in overestimated tip displacements in models as compared to the experimental data. Moreover, there was no tip displacement obtained experimentally in the 3% pre-strained sample due to the damaged film which is discussed in chapter 4. However, the simulated results for 3% pre-strained sample have depicted the highest tip displacement as a result of high pre-strain and intact NiTi film. With the increase in tip displacement, the maximum stress developed in the polyimide increases, which is evident from fig. 3.9.

3.6 Summary

- This chapter thoroughly discusses about the methodology for bimorph fabrication in this study. The variation in substrate conditions during deposition and the chamber condition were also discussed.
- The deposition process was carried out with thermal evaporation and E-beam evaporation technique.
- The process laser annealing of Kapton polyimide substrate and laser assisted micromanufacturing of the bimorph structure were established in this chapter.
- The theoretical simulation of the electrical actuation of the bimorph structure was done at varying pre-straining condition of the substrate in COMSOL Multiphysics.
- The bimorph was considered to be in a cantilever configuration and the supply of 25 V and 0.25A with a frequency of 0.25 Hz was applied. With increase in pre-straining condition up to 3%, the tip displacement of the bimorph increased. Also, the maximum stress developed in the bimorph structure increased with pre-strain.

Chapter 4

This chapter explains the effect of pre-straining and heating of Kapton polyimide substrate on the properties of NiTi/Kapton polyimide thin film structure as a self-actuating mirror.

Influence of Substrate Pre-straining and heating on characteristics of NiTi bimorph-based mirror

4.1 Mirror Fabrication

4.1.1 Substrate preparation

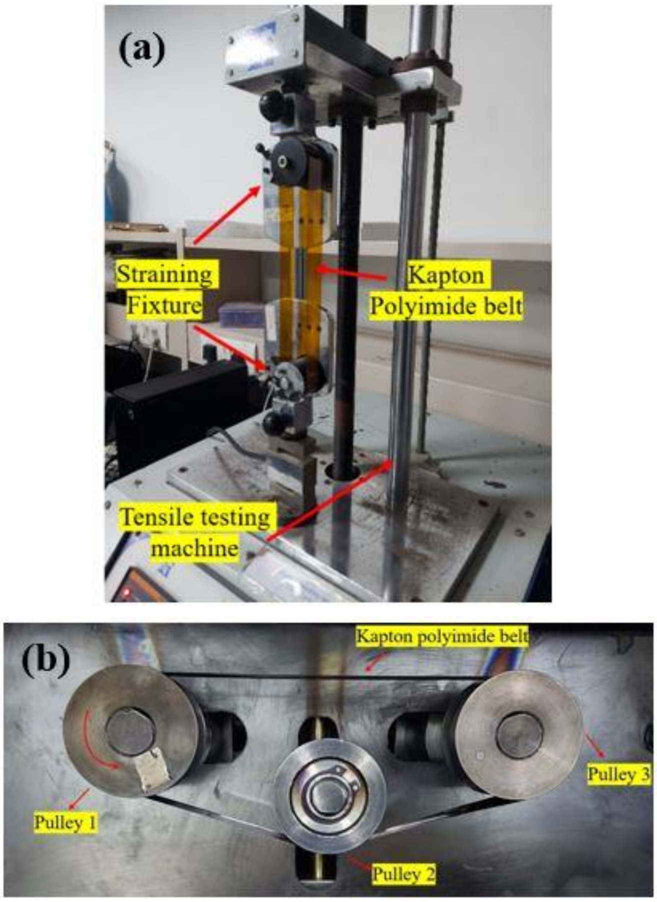

Fig 4.1: (a) Schematic of pre-straining setup for Kapton substrate in belt form. (b) Straining fixture for Kapton belt during deposition.

NiTi SMA thin film was deposited on Kapton polyimide substrate in the form of the belt using the E-beam evaporation technique (E-beam belt deposition unit- Hydro Pneo Vac Technologies). The Kapton polyimide belt of size 50 cm x 2 cm was first strained in a tensile testing machine shown in fig 4.1 (a). The Kapton polyimide substrate in the form of belt was held in the machine with the help of two pulleys. The initial length of the belt was measured and the distance between the pulleys is increased gradually such that the length of belt increases by 1% and 3%. Then the strained belt was taken out of the machine and placed in straining fixture as shown in figure 4.1 (b). The straining fixture is a three-pulley arrangement in which pulley 1 and pulley 3 are fixed while pulley 2 can be moved in the vertical direction to increase or decrease the strain on the flexible substrate. The pre-strained belt was placed in this fixture and pulley 2 was moved in vertically downward direction to achieve the length of the belt up to desired straining level. The substrate-loaded fixture was placed inside the deposition chamber and deposition was performed in the strained condition of the substrate. The pre-straining conditions applied for belts were unstrained, 1%, and 3% pre-strained conditions.

4.1.2 Thin Film Deposition

(a)

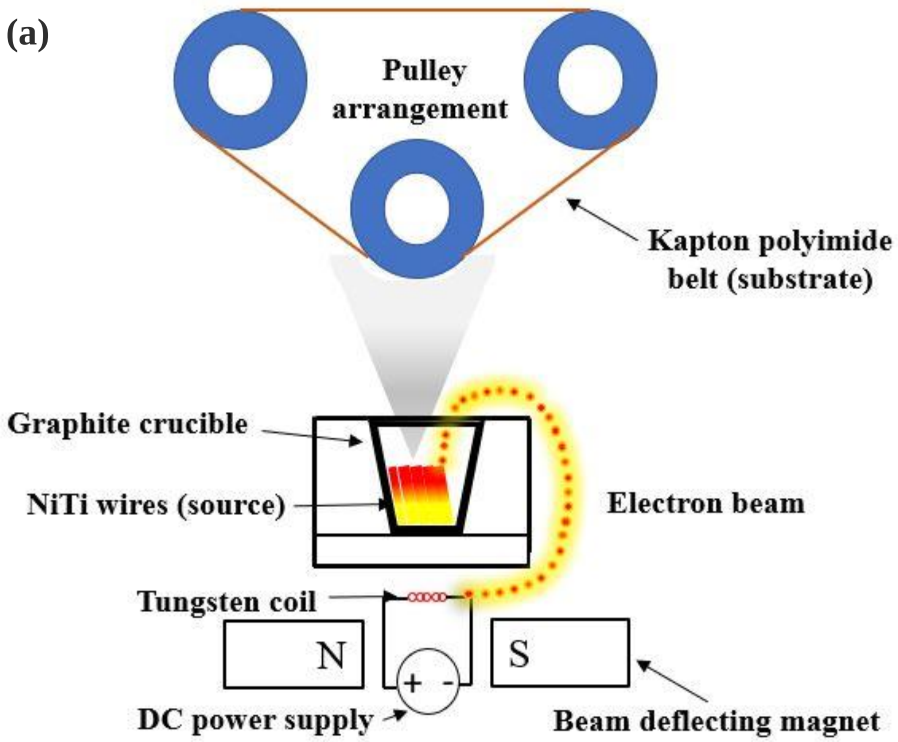

(b)

Fig 4.2: (a) Schematic of E-beam evaporation technique.
(b) NiTi/Kapton polyimide belt after the deposition process.

The deposition was done in the e-beam deposition unit. The source material for deposition was in the form of NiTi wire (54.2% Ni by weight) of size 4 mm x 1.2 mm. The Kapton polyimide substrate in pre-strained condition was held above the graphite crucible which holds the source material. For uniform deposition throughout the belt length, the pulleys were rotated with the help of external motor attached for substrate rotation. The pulleys were rotated at constant speed of 20 rpm during the deposition. The deposition process was carried out in the chamber pressure of 2 x 10^{-5} mbar, which was created using a rotary pump and diffusion pump. The deposition process was carried out at 5 kV DC and 340 A DC, supplied by an external power source for 240 s to 300 s. The schematic of the deposition process in the E-beam evaporation technique is displayed in fig. 4.2 (a). The fabricated bimorph mirror is shown in fig 4.2 (b) which was characterized for compositional and functional properties as a mirror.

4.2 Bimorph Characterization

4.2.1 Morphology and Composition

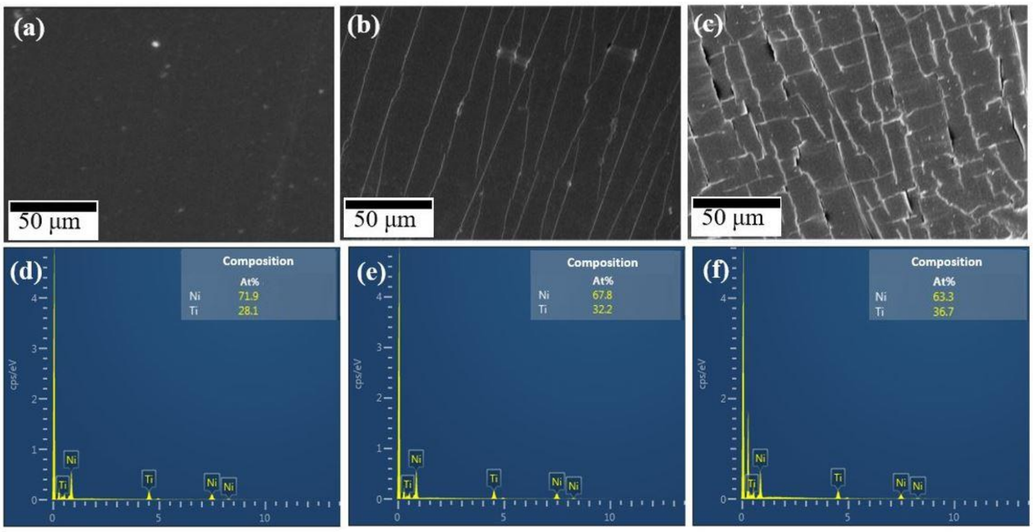

Fig 4.3: SEM images of deposited NiTi films on (a) unstrained, (b) 1% pre-strained, and (c) 3% pre-strained Kapton substrate. EDS images showing the composition of NiTi films deposited on (d) unstrained, (e) 1% pre-strained, and (f) 3% pre-strained Kapton substrate.

The surface morphology of NiTi thin film deposited using E-beam evaporation at varying pre-strains of the substrate is shown in fig. 4.3 (a), (b), and (c). The film on unstrained and 1% strained samples is uniform; however, strain marks are visible in the later sample. Less strain does not affect the performance characteristics of the bimorph as the film continuity is still intact. But the SEM image of bimorph with 3% pre-strain reveals the development of cracks in the film due to a large spring back in the Kapton polyimide substrate. The crack development in the deposited film might have negatively affected the performance of the bimorph. The compositions of the deposited NiTi films were determined by EDS analysis, which is displayed in fig. 4.3 (d), (e), and (f). All the deposited NiTi films were Ni-rich in composition, which has greatly affected their shape memory capabilities. There is a difference in evaporation temperatures of Ni and Ti. The power supply to the tungsten filament was constant which led to constant energy of the generated electron beam hitting the source material. However, Ni has low evaporation temperature as compared Ti which induce faster evaporation of Ni than Ti from the molten pool created in the graphite crucible. Thus, the deposited films were having high Ni content in all samples. Deposition time was 240 s to 300 s. With high deposition time the Ni content increases in the film. Pre-straining does not affect the composition of deposited NiTi film but will contribute to the smoothness and uniformity of the film.

4.2.2 Phase transformation study

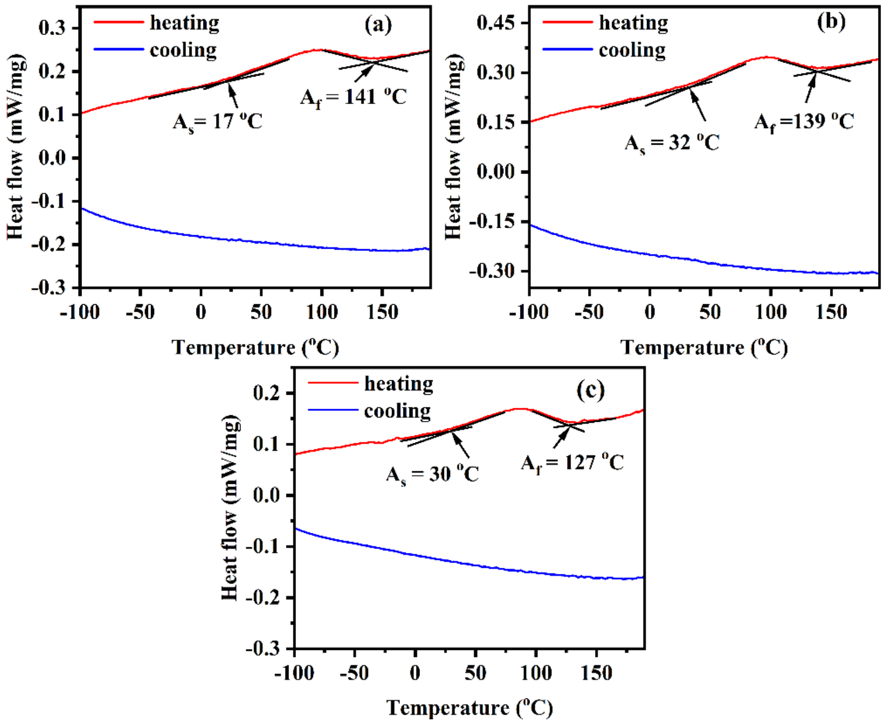

Fig 4.4: Phase transformation behavior of NiTi/Kapton polyimide bimorph with (a) unstrained, (b) 1% pre-strained, and (c) 3% pre-strained substrate.

Figure 4.4 depicts the phase transformation behavior of the bimorph samples. The endothermic (heating) cycle represents the reverse martensitic transformation, i.e., from Martensite to Austenite. The forward transformation from Austenite to Martensite phase is shown in the exothermic (cooling) cycle. The phase transformation temperatures for the studied samples in the heating cycle are shown in table 4. It has been stated that an increase in Ni content in NiTi thin film reduces Austenite finish temperature (A_f)[48,57]. Similar behavior was observed in the reverse transformation with both A_f and thermal hysteresis the least for the bimorph with the highest Ni content. The cooling cycle does not show any significant peak for the forward phase transformation. It has been reported in studies that an increase in Ni content by even 1% can drastically reduce the value of M_s (Martensite start temperature)[11,48]. As a consequence of high Ni content, Martensite transformation temperatures were very low and not detected in the DSC analysis till the temperature of -100 °C. The pre-straining of Kapton polyimide substrate also influences the transformation of the deposited film. The polyimide substrate was pre-strained during the deposition process. The NiTi film can deposit on the strained substrate in the twinned martensite phase or mixed twinned martensite and austenite phase. As the bimorph will be removed from the fixture, the polyimide recovers large strain owing to the strain recovery, thereby stressing the deposited film at room temperature. The stressing of the martensite phase results in the formation of the detwinned martensite phase[31], which can be directly transformed into the austenite phase on increasing the temperature of the stressed film. The stress generated in the NiTi film due the recovery of the Kapton polyimide substrate affects its transformation temperature. During reverse transformation (Martensite to Austenite), the generated stress hinders the phase transformation. Due to the hinderance, the energy requirement for phase transformation increases compared to unstressed phase transformation which results in higher transformation temperatures during reverse transformation cycle. Also, during the forward transformation (Austenite to Martensite) the stress results in start and finish of the transformation at much lower temperatures compared to unstrained film. Due to this reason along with the high Ni content in the film we were unable to observe forward transformation peaks in the DSC analysis.

Table 4: Transformation temperatures of the fabricated bimorph

Sample	A_s (°C)	A_f (°C)
Unstrained	17	141
1 % strain	32	139
3 % strain	30	127

4.2.3 Mirror Characteristics and Contact Angle measurements

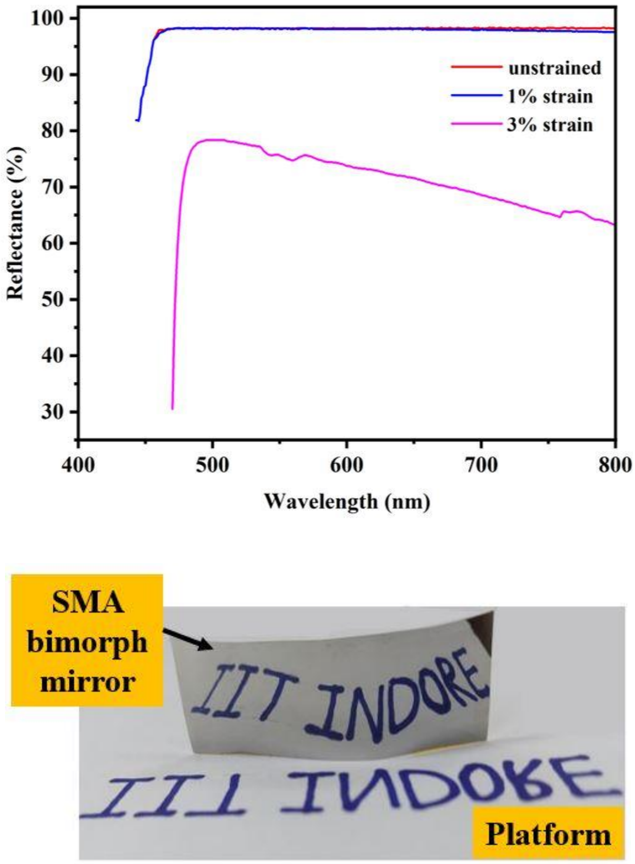

Fig 4.5: (a) UV Visible study of bimorph with varying pre-strain and (b) Depiction of the reflective surface of the bimorph.

The optical reflectivity of the NiTi/Kapton polyimide bimorph was analyzed using UV-Visible spectroscopy. Figure 4.5 (a) depicts the wavelength versus reflectance curve derived from the aforesaid study. The bimorph in the UV range (less than 450 nm wavelength) has shown negligible reflectivity. The optical reflectivity of visible light in the wavelength range of 450 nm to 800 nm was 98.3 % for unstrained bimorph. Pre-straining of 1% did not affect the reflectivity of bimorph significantly as the spring back of polyimide was not high. As a consequence, only strain marks appear in the SEM image of the deposited film, but there was no damage to the film. However, pre-straining of 3% resulted in cracks in the deposited film due to high substrate spring back, which is visible in the SEM image. The cracked film might cause dispersion of some fraction of incident light which reduces the reflectivity of bimorph. This resulted in a drop in reflectivity to 78.3 % for near UV wavelength, which dropped further for near IR wavelength. The high reflectivity of the NiTi/ polyimide bimorph will be potentially applicable as a flexible micromirror by utilizing Joule heating of the bimorph in the interferometry[12]. Figure 4.5 (b) manifests the mirror-like reflectivity and finish of the bimorph which will be desired for the micromirror application.

4.2.4 Electrical Actuation

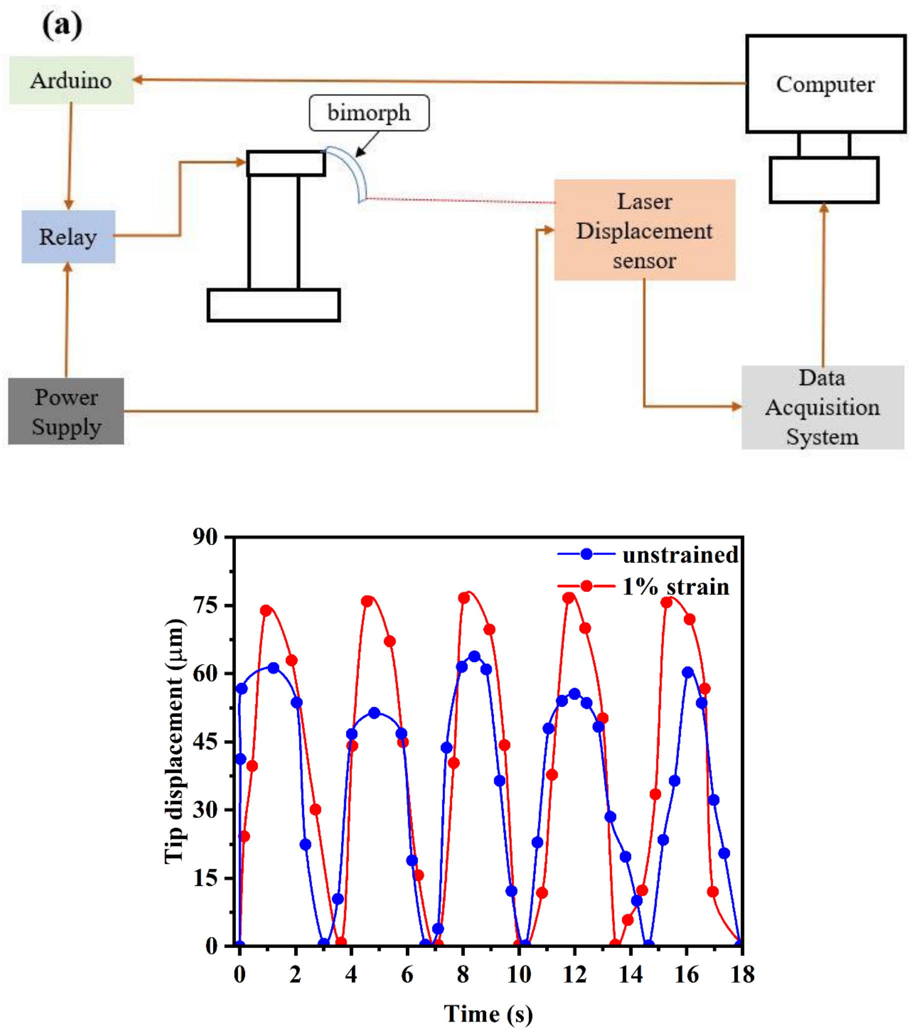

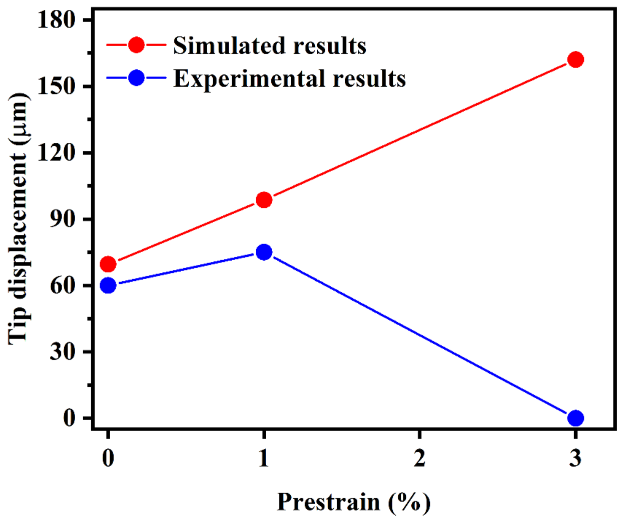

Fig 4.6: (a) Schematic of Electrical actuation setup, and (b) Experimental determination of actuation of bimorph with unstrained and 1% pre-strained substrate. (c) Comparison of Simulated and experimentally determined tip displacements for different pre-strain on the substrate.

The basic setup for electrical actuation of bimorph and its actuation sensing is displayed in fig. 4.6 (a). The bimorph with dimensions of 4 cm x 2 cm was cut and connected to the circuit in a cantilever configuration for the investigation of electrical actuation. The power for Joule heating was supplied by a power supply connected to a relay. The relay has been switched on and off through the computer using an Arduino, which was programmed for a frequency of 0.25 Hz. The power source also drives a laser displacement sensor which, in conjunction with the data acquisition system, gives a measure of the displacement of the bimorph tip. The bimorph does not draw any current up to an input voltage of 10 V. The maximum current drawn by the bimorph was 0.25 A at a 25 V supply, at which the measurements were made. On further increasing the voltage, the bimorph got burnt. The compositional deviation from Ni 50 at% plays an important role in degrading the actuation characteristics of NiTi, due to which higher actuation power was required.

Figure 4.6 (b) shows the experimentally determined tip displacement at mentioned conditions for the fabricated samples. The tip displacement for unstrained bimorph was 60 μm which increased to 75 μm for bimorph with 1% pre-strain. When power was supplied to the NiTi film, it heats due to Joule heating and reverse phase transformation starts resulting in actuation of the bimorph structure. During the actuation, the bimorph structure becomes straight compared to the initial curved configuration. On cooling to room temperature, the Kapton polyimide substrate regains its curved shape. Due to this curvature, strain is generated in the film at room temperature thereby inducing forward transformation. The EDS analysis in section 3.1 indicates that the composition of NiTi film on 1% pre-strained bimorph was close to NiTi50% as compared to the unstrained bimorph. This change of film composition towards equiatomic NiTi may have resulted in better actuation in 1% pre-strained bimorph. However, the bimorph with 3% pre-strain did not show any movement on supplying the power even after having the film composition closest to equiatomic NiTi. This was due to the crack generation in NiTi film, owing to the spring back of the Kapton substrate after deposition. The cracks in the deposited film resulted in an electrical discontinuity in it, and thus, no electric current flows through the film in bimorph with 3% pre-strain.

The comparison of experimentally obtained tip displacement with simulated results is illustrated in figure 4.6 (c). The simulation model has been discussed in chapter 3, where the tip displacement was linearly increasing with increase in pre-strain of Kapton polyimide. The unstrained bimorph in simulation showed 69.5 μm tip displacement, however, the experimentally observed value was 60 μm. The overestimation of tip displacement was also observed with simulation results of pre-strained bimorphs. This overestimation is due to consideration of linear variation of thermal and SMA properties of the NiTi film such as Martensite volume fraction and specific heat with temperature. More accurate results can be obtained by adding non-linearity to these properties. For 3 % pre-strain, simulation result was 162 μm while experimentally no actuation was observed due to film damage discussed above. This error can be eliminated by adding film discontinuity of NiTi in the simulation for 3 % pre-strain bimorph.

4.3Influence of Substrate Pre-straining and Heating

4.3.1 Mirror Fabrication

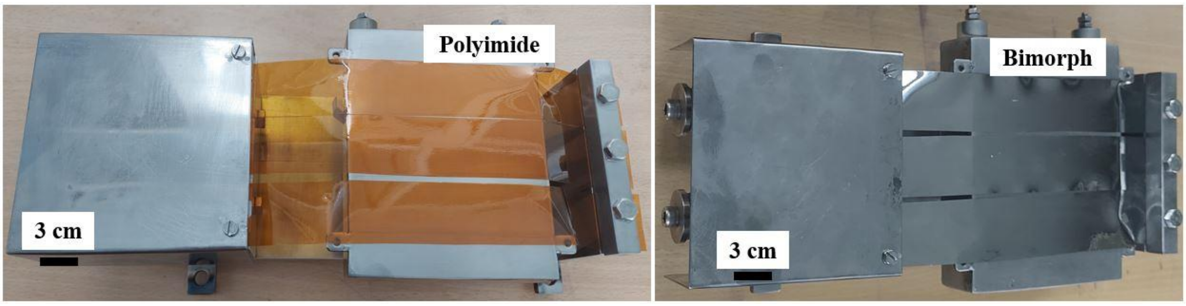

Fig 4.7: Fixture for linearly straining the Kapton polyimide belt during deposition

The influence of substrate heating on the film deposition and substrate to film adhesion has been investigated in various studies. This section of the work is aimed to achieve the same along with the pre-straining. The pre-straining fixture discussed in the previous section had the provision for rotation of the Kapton polyimide substrate during the deposition process. However, with the three-pulley arrangement, the substrate was not always in contact with holder surface and which hinders continuous substrate heating. Substrate pre-straining and heating were applied simultaneously with the help of a custom-made fixture. Fig 4.7 illustrates the pre-strained Kapton polyimide belts of size 200 mm x 30 mm, which were linearly strained in the fixture. Also, the belts were in continuous contact with the substrate heater during the strained condition. The substrate was subjected to pre-strain condition of unstrained, 1% and 2% pre-strain. Additionally, the substrate temperature applied were room temperature, 50 °C, 100 °C, 150 °C and 200 °C. The deposition was performed using e-beam evaporation technique at chamber pressure of 5 x 10^{-5} mbar. The deposition was performed at 5.4 kV voltage and 190 mA and 240 mA supply current. The time of deposition was 198 s with a source material of NiTi: Ti in ratio of 70:30 by weight.

4.3.2 Bimorph Characterization

4.3.2.1 Structural Analysis

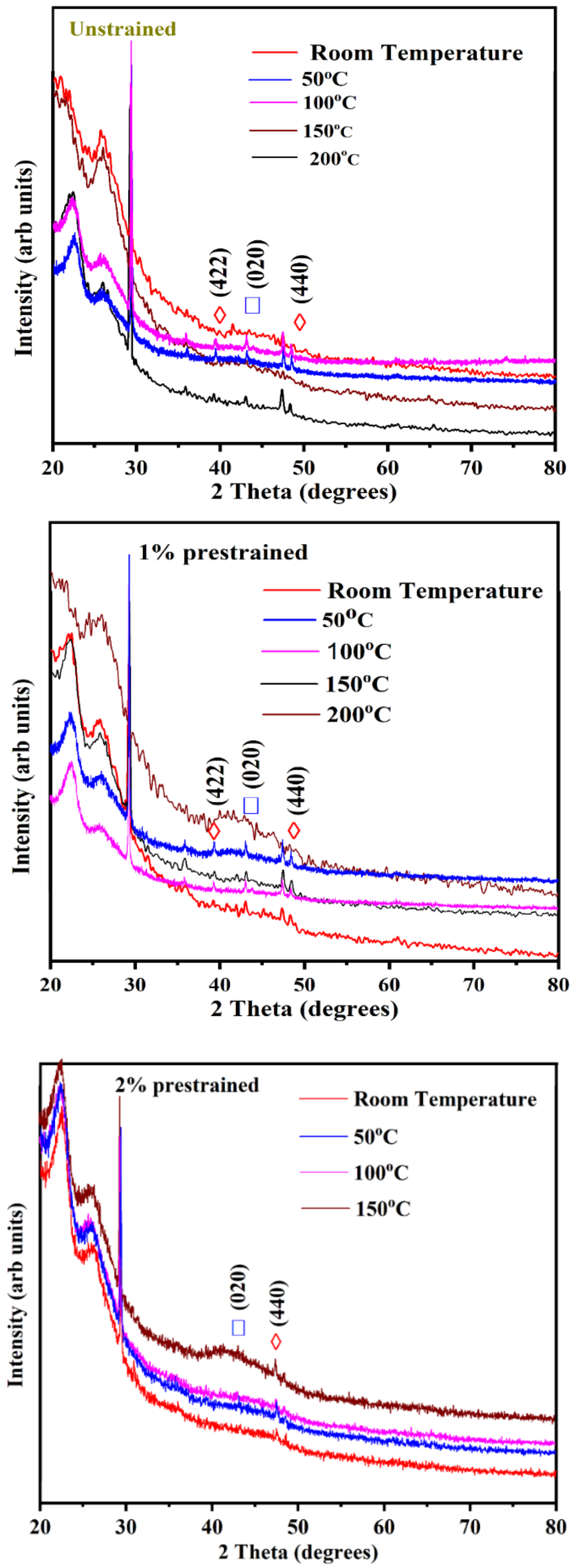

Fig 4.8: XRD analysis of deposited NiTi films at varying pre-strain and temperature of the substrate.

The XRD analysis of the fabricated NiTi/Kapton polyimide bimorph mirrors at various process parameters was performed in the 2θ range of 20° to 80° at a scan rate of 2°/min. The deposited film thickness was 900 nm and due to less thickness, the scan results show peaks of both NiTi film and the Kapton polyimide substrate. The two humps and a large peak before 30° in fig 4.8 correspond to Kapton polyimide. The peaks of NiTi thin film are visible in region of 40° to 50°. Peak (020) in fig 4.8 corresponds to Martensite phase (B19') while peaks (422) and (440) are of Ti_2Ni. As the substrate pre-strain is increasing, the crystallization phases in the film have reduced. At the same pre-strain condition of the substrate, the higher substrate temperature leads to increment in crystallization of the NiTi phases.

4.3.2.2 Wettability Study

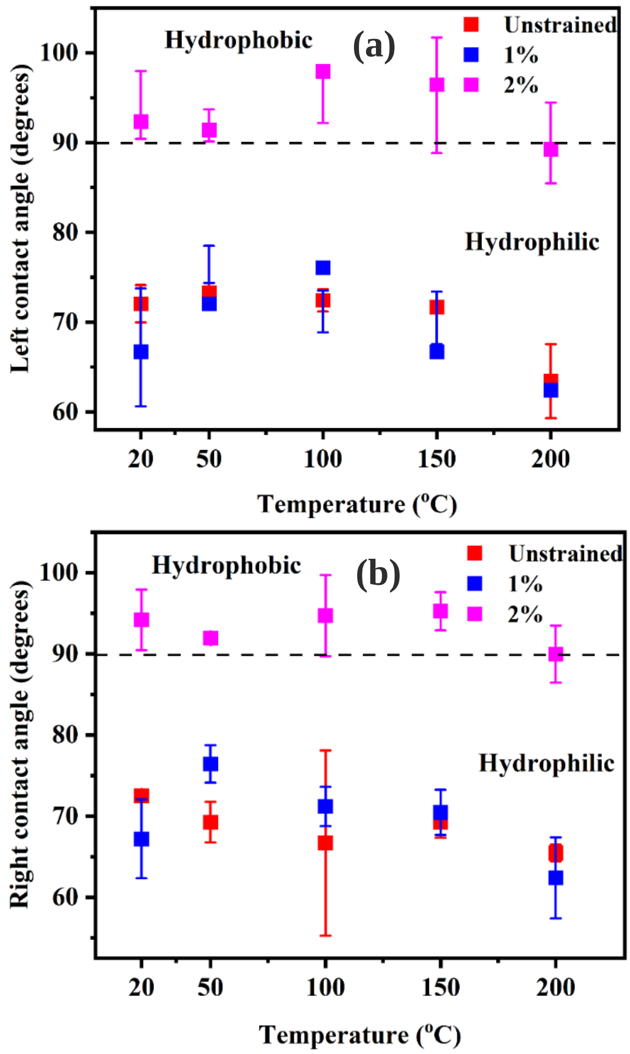

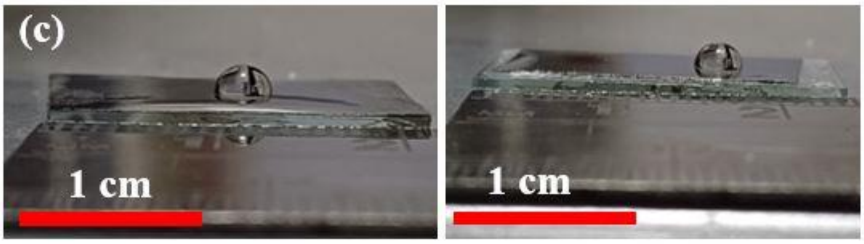

Fig 4.9: (a) and (b) Measured left and right contact angles of deposited NiTi films at varying pre-strain and temperature of the substrate. (c) Droplet of DI water placed on the hydrophobic surface of the bimorph.

The deposited films were tested for their hydrophobicity using a contact angle meter. Fig 4.9 (a) and (b) shows the variation of the left and right contact angles of the bimorph mirrors fabricated at varying pre-strain and temperature condition. At all the pre-strain values the increase in substrate temperature during deposition has led to increase and then decrease of hydrophobicity of the film. The substrate temperature of 150 °C has shown the best hydrophobicity at all pre-strain conditions. The film deposited at 2% pre-strain has shown the hydrophobic surface where contact angles were above 90°. This was due to the higher power supply during the deposition at this pre-strain condition. The higher power supply produces a denser film which resulted in hydrophobic films. The hydrophobicity of the film can be visibly seen by just dropping a DI water droplet on the mirror surface. The whole droplet sits on the surface of the mirror as shown in fig 4.9 (c).

4.3.2.3 UV-Visible Study

The mirror characteristics were studied using a UV -Visible spectroscopy. At all the pre-strain and substrate temperatures the fabricated bimorph mirrors have shown a reflectivity of more than 90% for a wavelength range of 400 nm to 800 nm. For some films fabricated at 2% pre-strains, the reflectivity has been nearly 100% as shown in fig 4.10 (c), where denser and high-quality films were achieved. Also, at certain substrate temperatures with unstrained and 1% pre-strained samples, the reflectivity has varied in a zigzag pattern. This pattern can be a result of phenomenon called as interference in thin film due to reflected light. Due to this phenomenon, some of the incident light on the interface of the NiTi film and Kapton polyimide substrate reflects from the interface and remaining transmits through. The reflected light from the interface interferes with the light reflected from the top surface of the NiTi film. Destructive interference reduces the intensity while constructive interference increases, thus, we see a zigzag pattern in the reflectivity as shown fig 4.10 (a) and (b), depending upon the interference.

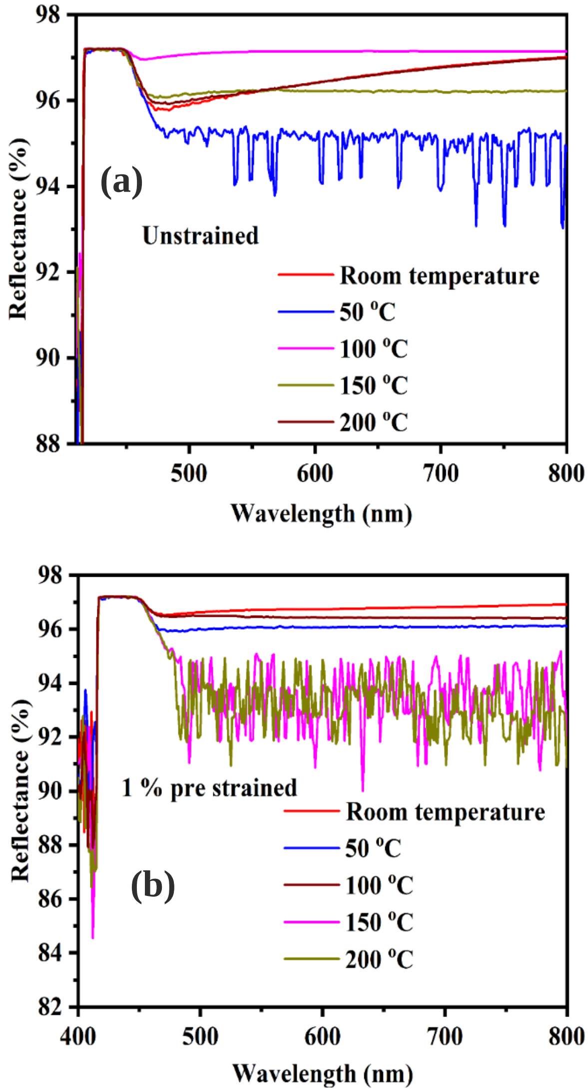

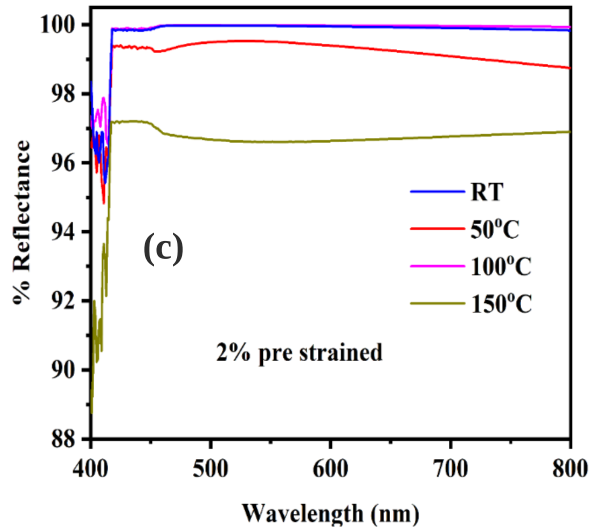

Fig 4.10: Reflectance study of deposited NiTi films at varying pre-strain and temperature of the substrate.

4.3.2.4 Phase Transformation Analysis

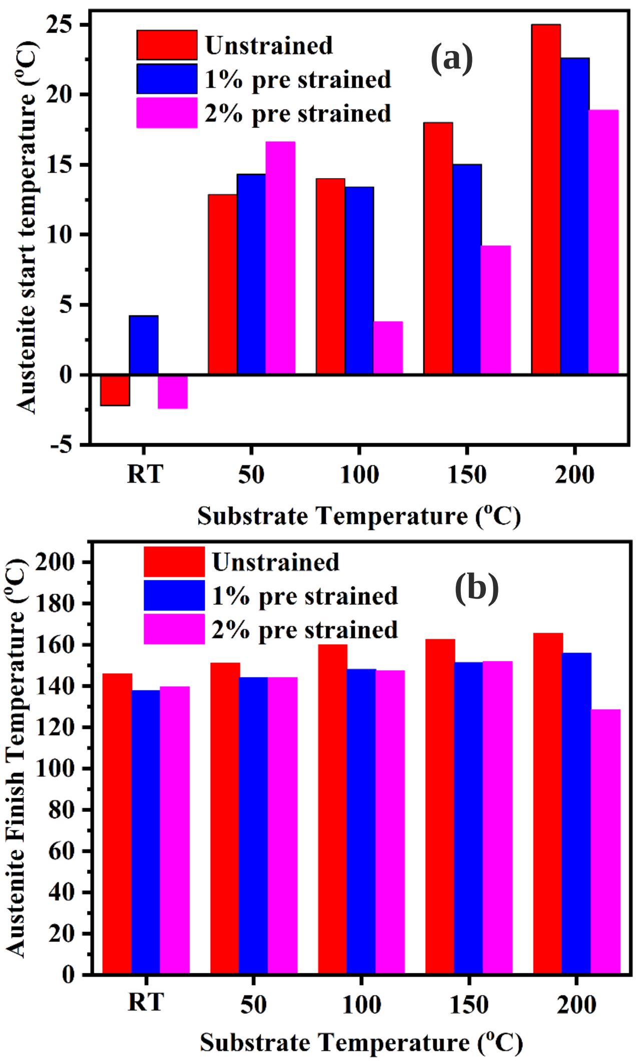

Fig 4.11: (a) and (b) Phase transformation analysis of deposited NiTi films at varying pre-strain and temperature of the substrate.

4.3.2.5 Adhesion Test

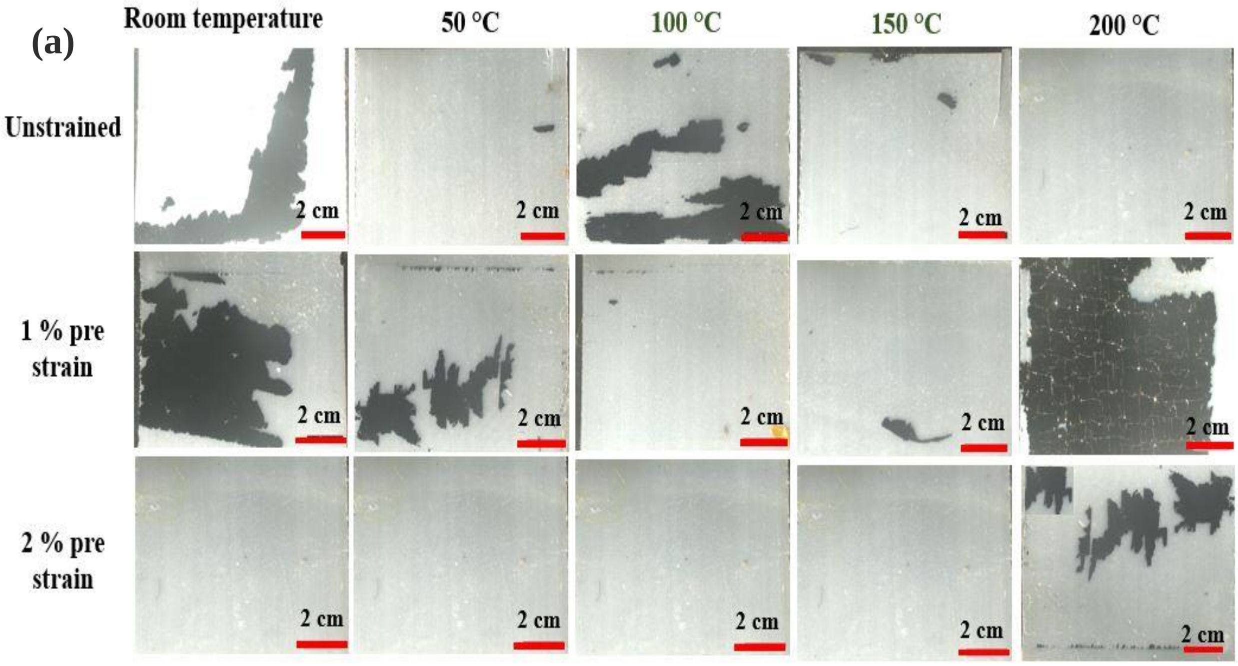

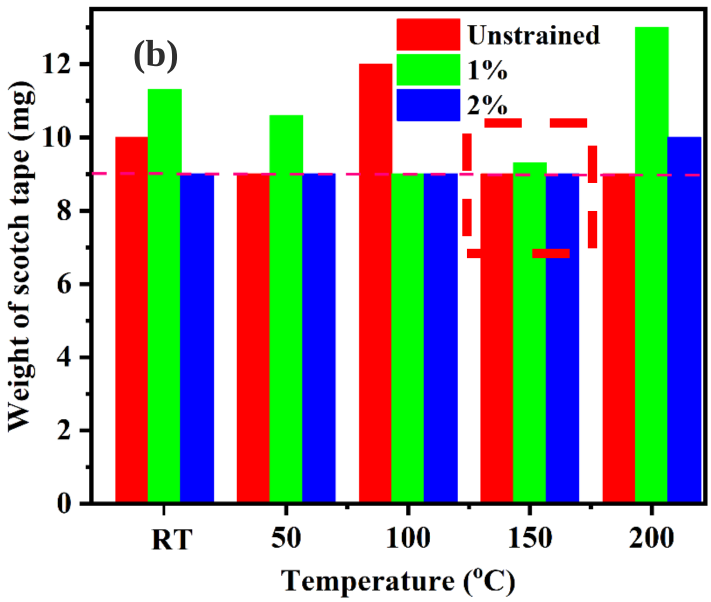

Fig 4.12: (a) Images of the Scotch tape after removal form the samples. **(b)** Measured weight of the Scotch tape after the test.

The adhesion of the deposited NiTi films with the substrates were tested with a Scotch tape. Fig 4.12 (a) shows the optical image of plain scotch tape of the mentioned size, which weighed 9 mg. The following images show that the film adhered to the tape after the test. The scotch tape was weighed before and after the test to quantify the material removed. The amount of material removed from the bimorph surface after the Scotch tape removal is depicted in fig 4.12 (b). Substrate heating has improved the substrate-to-film adhesion which is visible in the results. The weight of Scotch tape after removal form bimorph fabricated at room temperature were 10 mg, 11 mg and 9 mg respectively for unstrained, 1% pre-strained and 2 % pre-strained condition. The best adhesion was observed at 150 °C substrate heating, where the measured weights of the Scotch tape after test were 9 mg, 9.5 mg and 9 mg respectively for unstrained, 1 % pre-strained and 2 % pre-strained bimorphs. The substrate heating of 200 °C resulted in a reduction in substrate-to-film adhesion. Thus, the optimum substrate temperature can be 150 °C, where improved hydrophobicity, phase transformation and film adhesion were achieved.

4.4 Summary

NiTi thin film was fabricated on a flexible Kapton polyimide substrate employing the E-beam evaporation technique. The study focused on the effects of pre-straining and heating of the substrate during deposition on the attributes of the NiTi/Kapton polyimide bimorph as a flexible micromirror. The outcomes of the study are summarized below.

- The electrical actuation of the structure in the cantilever configuration resulted in a maximum tip displacement of 75 μm for 1% pre-strained bimorph at 25 V and 0.25A with a supply frequency of 0.25 Hz. The simulated tip displacements for all the considered conditions were higher than the experimental values. Moreover, the bimorph with 3% pre-strain does not show any displacement during the experiment due to discontinuous film.
- The SEM showed a smooth surface for unstrained bimorph, and pre-straining induces strain marks on the bimorph. Higher pre-strain damages the film after deposition due to the spring back of the flexible substrate. The composition analysis revealed the distinction in the compositions of NiTi/polyimide structure.

- Variation in the amount of nickel in the NiTi film has affected the transformation temperatures. A_f increased with the increasing Ni content.
- An excellent optical reflectance of 98.3% was observed for unstrained and 1% pre-strained bimorph in the visible region, which has applicability as a flexible micromirror.
- Hydrophobic films have been achieved with denser film at substrate heating of 150 °C.

Chapter 5

This chapter describes the influence of laser annealing of Kapton polyimide substrate on the properties of thin film-based actuators.

Laser Annealing of Kapton polyimide substrate towards improvement in characteristics of NiTi/Kapton polyimide actuators

5.1 Actuator Fabrication

5.1.1 Laser Annealing

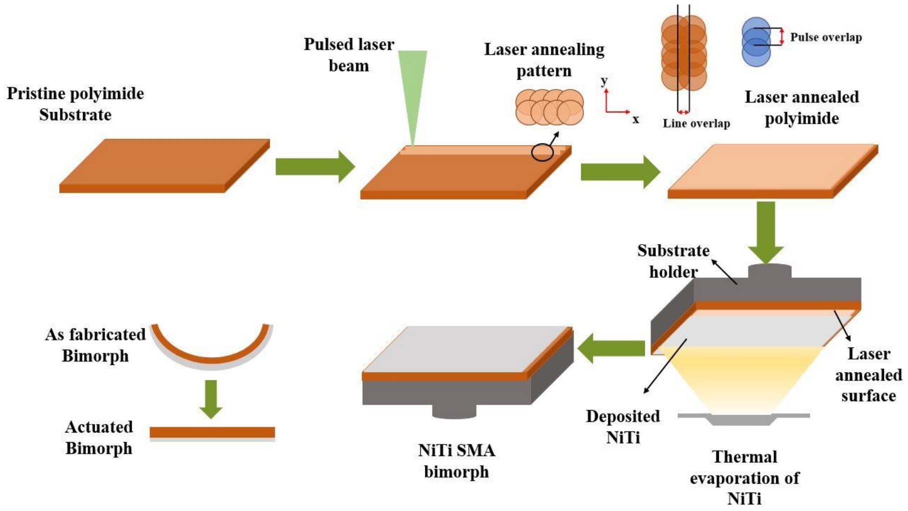

Fig 5.1: Schematic of Laser annealing and NiTi thin film deposition on polyimide

Kapton polyimide substrates of size 75 mm x 44 mm were laser annealed using Nd: YAG laser (Spectra-Physics- Quanta Ray). The laser wavelength used for annealing was 355 nm, which is near the UV range. The polyimide substrates were pasted on glass slides to flatten the natural curvature of polyimide during the laser annealing performed on the setup shown in fig 5.1. The laser annealing was performed at laser fluences of 500 mJ/cm², 1000 mJ/cm², 1200 mJ/cm², and 1630 mJ/cm² with a line % LO of 50%, 70%, and 90%. The laser pulse energy has a Gaussian profile; thus, for uniformity of the laser modifications throughout the sample surface, the laser spot has to be applied in an overlap condition. This has to be achieved by controlling the speed of the stage in both the x and y directions. The overlap between the consecutive laser spots is the spot overlap (in the x direction), and the overlap between the consecutive line patterns in the y direction is the line overlap (% LO) illustrated in fig 5.1. A constant spot overlap of 95% was applied in all the laser annealing samples.

5.1.2 Thin Film Deposition

NiTi SMA thin film was deposited on laser-annealed substrates using the thermal evaporation technique (Thermal deposition unit- Hydro Pneo Vac Technologies). NiTi wire (54.2% Ni by weight) and Ti wire of size 4 mm x 1.2 mm were the source materials for deposition. As the vapor pressure of Ni is low compared to Ti, thus Ni evaporates faster and deposits in a higher amount than Ti. To compensate for this loss of Ti in the deposited film, excess Ti in the form of wire was added to the source material. The source material was NiTi: Ti in the ratio of 70:30 by weight. The deposition process was carried out in the chamber pressure of 5 x 10^{-5} mbar, which was created using a rotary pump and diffusion pump. The deposition process was carried out at 450 A for 60 s.

5.2 Actuator Characteristics

5.2.1 Optical Analysis

The optical images of the laser-annealed polyimide at various fluences and % LO are illustrated in fig 5.2. The annealing at a fluence of 500 mJ/cm^2 and 50% LO does not induce a visible change on the polyimide's surface, illustrated in fig 5.2 (a). A higher % LO resulted in the formation of a visible pattern, which can be due to the crystallization of more surface molecules and an increment in the breaking of polymer bonds. Crystallization also resulted in peak formation in XRD spectra. Similarly, the intensification of the patterns at the same % LO with increasing laser fluences can be explained. The laser fluence of 1200 mJ/cm^2 and 90% LO have created uniform patterns on polyimide, suggesting vaporization and material removal from the surface. There has been visible roughness on the polyimide surface after annealing with a laser fluence of 1630 mJ/cm^2. This higher roughness results from the vaporization of polyimide molecules from the upper layer leaving behind soot.

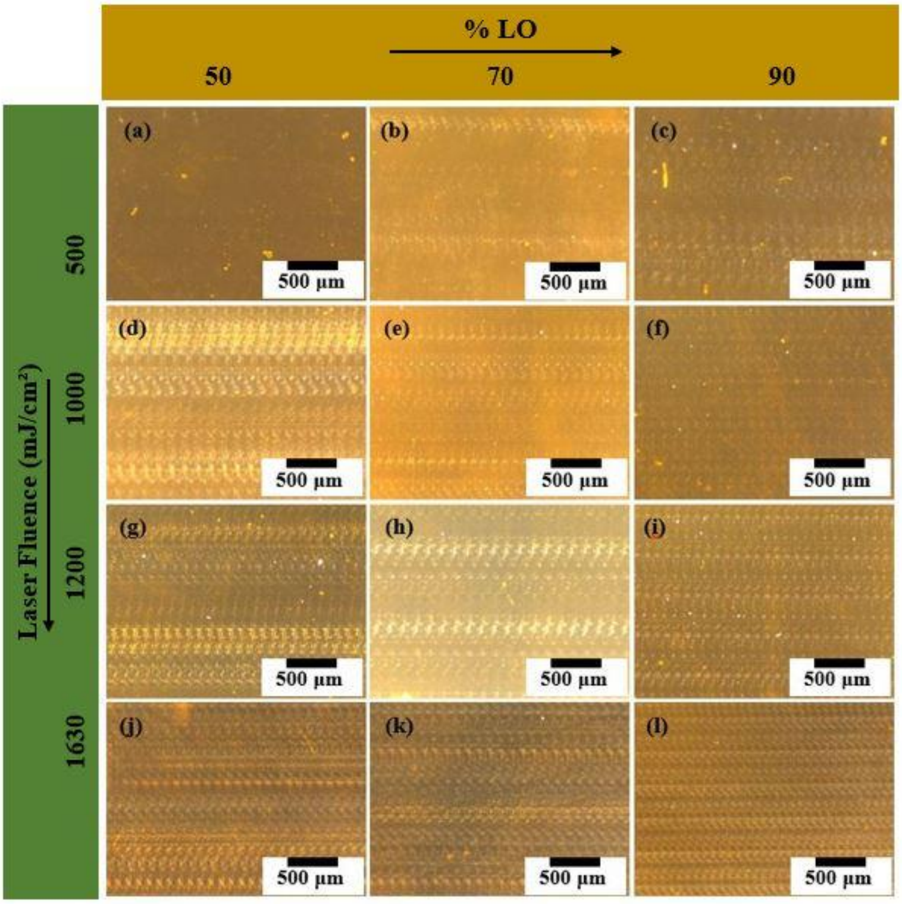

Fig 5.2: Optical images of polyimide laser treated at (a), (b), (c) 500mJ/cm² (50%, 70% and 90% line overlap), (d), (e), (f) 1000 mJ/cm² (50%, 70% and 90% line overlap), (g), (h), (i) 1200 mJ/cm² (50%, 70% and 90% line overlap) and (j), (k), (l) 1630 mJ/cm² (50%, 70% and 90% line overlap).

5.2.2 Structural Analysis

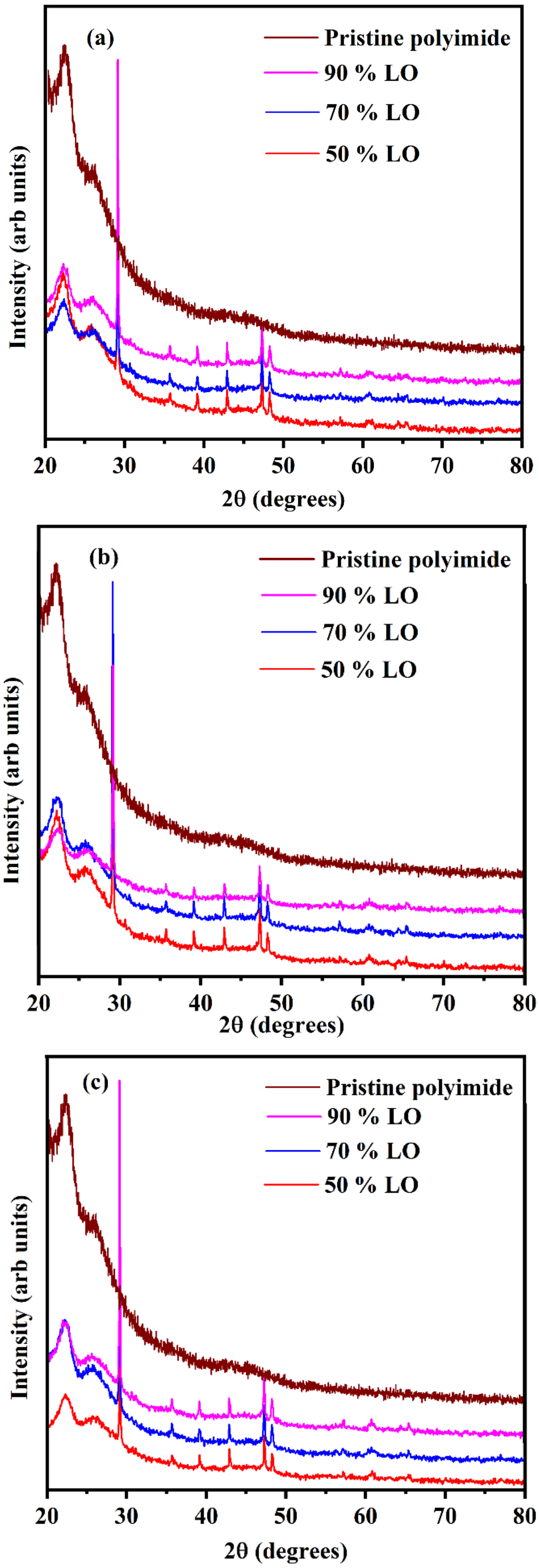

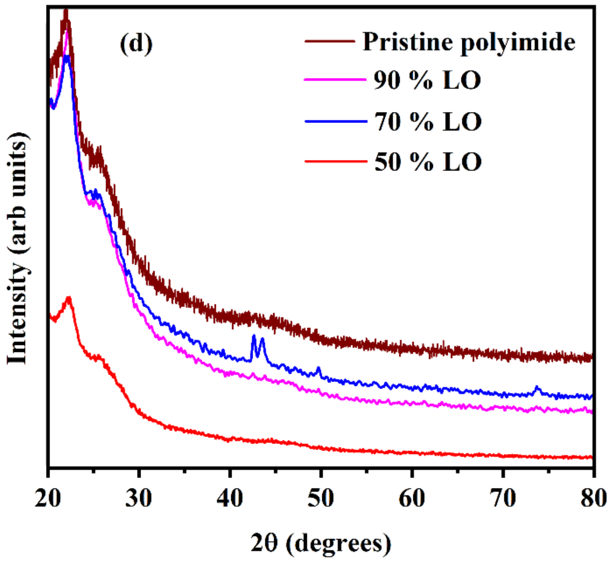

Fig 5.3: XRD analysis of the Kapton polyimide substrate after laser annealing at laser fluences of (a) 500, (b) 1000, (c) 1200 and 1630 mJ/cm^2 and varying % LO.

The XRD spectrum of pristine polyimide is illustrated with the brown graph in fig 5.3. Two broad peaks were observed in the 2θ range of 20° to 30°, which are characteristic amorphous peaks of polyimide[58]; moreover, a hump was present between 40° to 50°. The laser annealing of polyimide at fluences of 500 mJ/cm^2, 1000 mJ/cm^2, and 1200 mJ/cm^2 caused the formation of sharp peaks at 29°, 35.8°, 39.1°, 43°, 47.2°, 48.3° and 60.6°. These peaks signify the formation of crystalline domains in the polyimide after annealing [58]. The formation of crystalline peaks can be attributed to the melting and resolidification of the polyimide at the surface due to the photothermal action after laser interaction. Higher laser fluences and % LO induce high heat to the polyimide surface, thereby producing bigger XRD peaks up to 1200 mJ/cm^2, suggesting improved crystallinity of polyimide.

At laser fluence 1630 mJ/cm^2, higher laser fluence led to soot formation on the polyimide surface. Soot is loose carbon particles formed on the polyimide's surface due to the decomposition of surface molecules. Its presence reduces the adhesion of polyimide with the deposited NiTi film. Thus, soot must be cleaned off the polyimide's surface before deposition. However, soot cleaning exposes the subsurface layer of polyimide, thereby producing lesser crystalline domains. Thus, only characteristic broad peaks were seen in fig 5.3 (d). Moreover, peaks at

42.6°, 43.5°, and 73.8° were noticed at a laser fluence of 1630 mJ/cm^2 at 70% LO suggesting better crystallinity than the other two LO at 1630 mJ/cm^2. With laser fluences up to 1200 mJ/cm^2, an increase in the LO from 50% to 90% has marginally improved the crystallinity owing to an increment in intensities of the crystalline peaks between 29° to 61°.

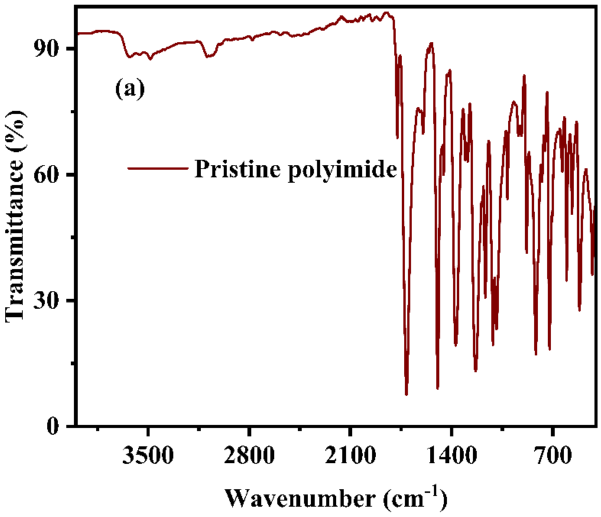

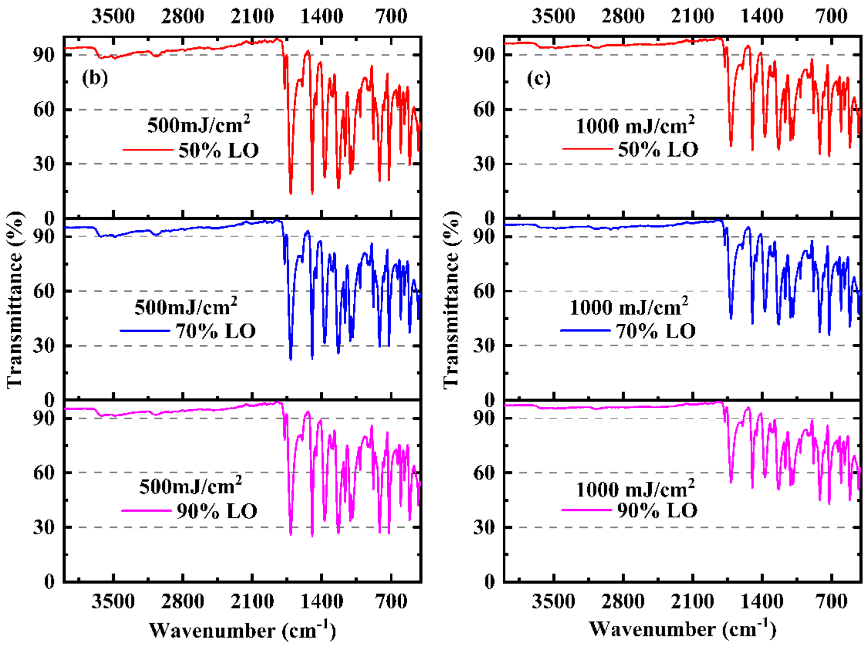

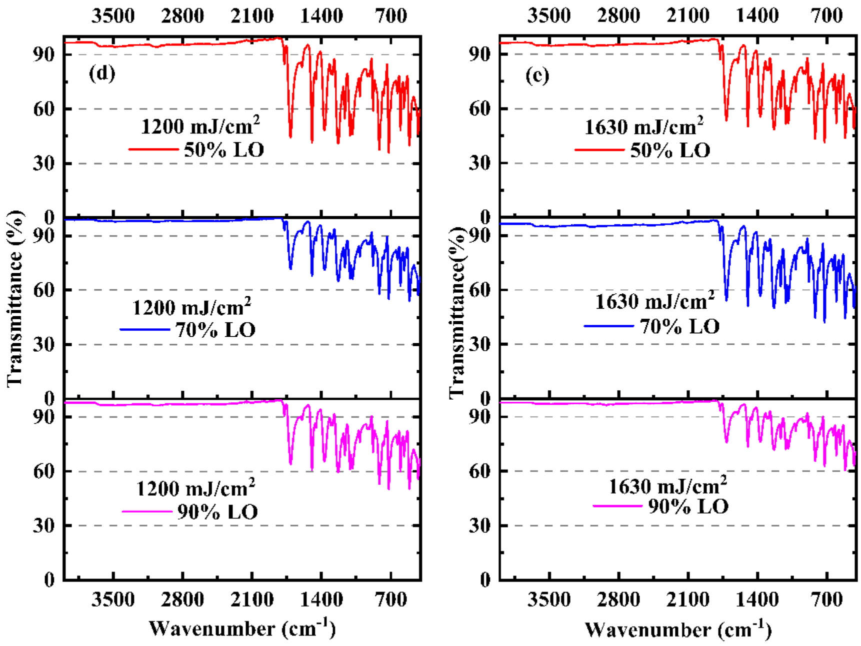

Fig 5.4: IR spectra for (a) pristine polyimide, and (b), (c), (d), and (e) Polyimide treated with laser at various laser fluences and line overlaps (LO).

Table 5: Transmission wavenumbers in FT-IR spectra of pristine polyimide

Peak position (cm^{-1})	Identification
3450 to 3650	—OH bonds[59]
3097 to 3056	aromatic =C—H stretching[59]
1777, 1715	C═O stretching[59–61]
1601, 1498	aromatic =C═C stretching[59–61]
1455	skeleton vibration of phenyl rings[59–61]
1370	cyclic imide (=C—N—) stretching[59,60]
1238	Asymmetric stretching of aromatic ether (C—O—C)[60]
1167, 1115, 1091 and 1016	Para substituted phenyl, in-plane hydrogen rocking[59,60]
883	out of plane waging vibration of isolated hydrogen in (1, 2, 4, 5)[59,60]

818	out of plane waging vibration of two adjacent hydrogens[59,60]
723	cyclic imide[60,61]
605	bending vibration of C—O—C[59]
635	C=O deformation[59,61]
567	rocking band of cyclic imide[59]
515	out of plane ring bending

The changes on the polyimide surface with laser annealing were also examined using FT-IR spectroscopy in transmission mode. The spectra of the pristine and laser-annealed polyimide's visible, near-infrared, and infrared bands have been determined. The corresponding spectra are shown in figure 5.4. The infrared bands were assigned according to the absorption band available for pristine polyimide[58]. Table 5 presents information about the transmittance peaks obtained in the spectroscopic study of the pristine polyimide.

Fig 5.4 (b), (c), (d), and (e) depict the variation in peak intensity of the polyimide samples with varying laser fluences. The laser annealing of polyimide does not create any new peaks in the spectra. As the laser fluence has increased, the peaks between 3450 to 3650 cm^{-1} and 3097 to 3056 cm^{-1} have progressively diminished, suggesting loss of OH bonds due to moisture removal and aromatic =C—H stretching, respectively. The laser annealing has resulted in modification in the crystallinity and structure of the polyimide surface, indicated by slight shifts in the peak positions [60] [62]. Laser treatment up to a fluence of 1200 mJ/cm^2 improved the crystallinity of polyimide, which was also evident from the XRD spectra. The laser fluence of 1630 mJ/cm^2 at all LO resulted in soot formation at the polyimide surface[26],[63],[64],[65]. Furthermore, laser irradiation on the polyimide surface induces surface changes which lead to a change in the transmittance of the samples. From Beer's law, the absorbance of a material is related to its concentration, as given in equation 4[66].

$$A = \varepsilon l c \qquad \ldots\ldots(4)$$

where A is absorbance, ε is absorptivity ($Mol^{-1}cm^{-1}$), l is optical path length (cm), and c is the molar concentration of material (Mol). The significant increase in transmittance of polyimide with an increase in laser fluence from 1000 mJ/cm^2 to 1630 mJ/cm^2 suggests the loss of surface molecules. This increment implies that less material concentration of polyimide was available for analysis. Thus, the absorbance of polyimide reduces with an increase in transmittance, according to equation 5.

$$A = 2 - \log_{10}(\%T) \quad \text{….(5)}$$

where A is absorbance and %T is percentage transmittance. This increment in transmittance with the increase in laser fluence can be derived from fig 5.4. At all fluences, an increase in % LO increases the transmittance indicating progressive destruction of imide rings.

5.2.3 Surface Morphology

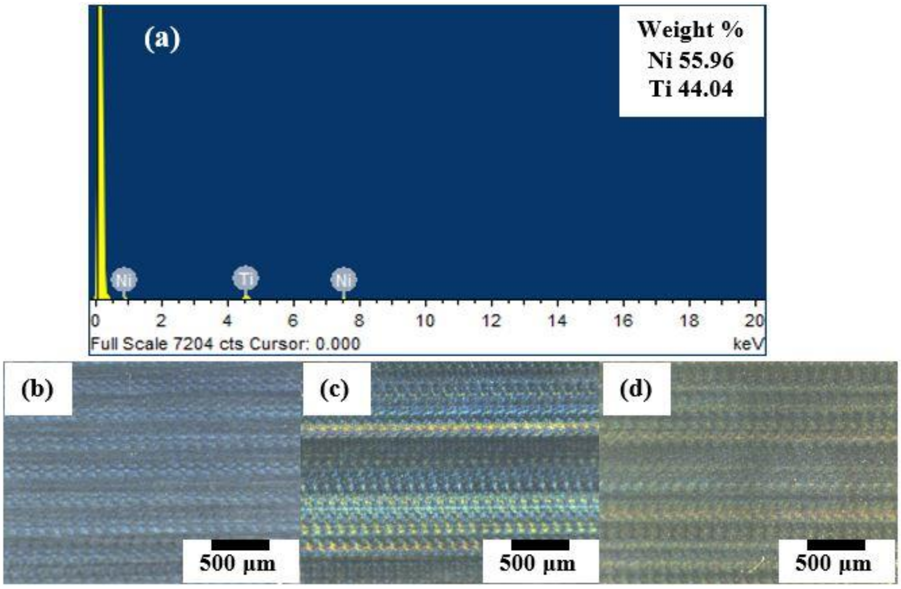

Fig 5.5: (a) Composition of the deposited NiTi film and Optical images of NiTi coated polyimide laser annealed at fluences of 500 mJ/cm^2 and 1630 mJ/cm^2 with line overlaps of (b) 50%, (c) 70%, and (d) 90%.

The microscopic images of laser-annealed bimorphs are shown in fig 5.5. The annealing patterns on polyimide are visible even after the deposition of NiTi on the surface. Out of the 12 different laser-patterned polyimide samples, the optimal three were utilized for deposition. The selection criteria for the best laser-treated polyimide substrates are explained in section 5.2.4. At laser fluence of 500 mJ/cm^2 and 90 % LO subdued pattern appeared as a result of photothermal reaction during annealing. However, the photophysical process at a laser fluence of 1630 mJ/cm^2 leads to the formation of deep ablation patterns, which are readily observable even after the deposition. This can be attributed to a higher degree of material removal during laser annealing resulting in the formation of intricate grooves. The EDS analysis of the deposited film shows that the composition was Ni-rich. All the films were deposited simultaneously with thermal evaporation, which gives the same film composition for all the samples. However, different surface conditions for every sample due to laser annealing may result in different film adhesion and subsequent characteristics.

5.2.4 Wettability and Adhesion

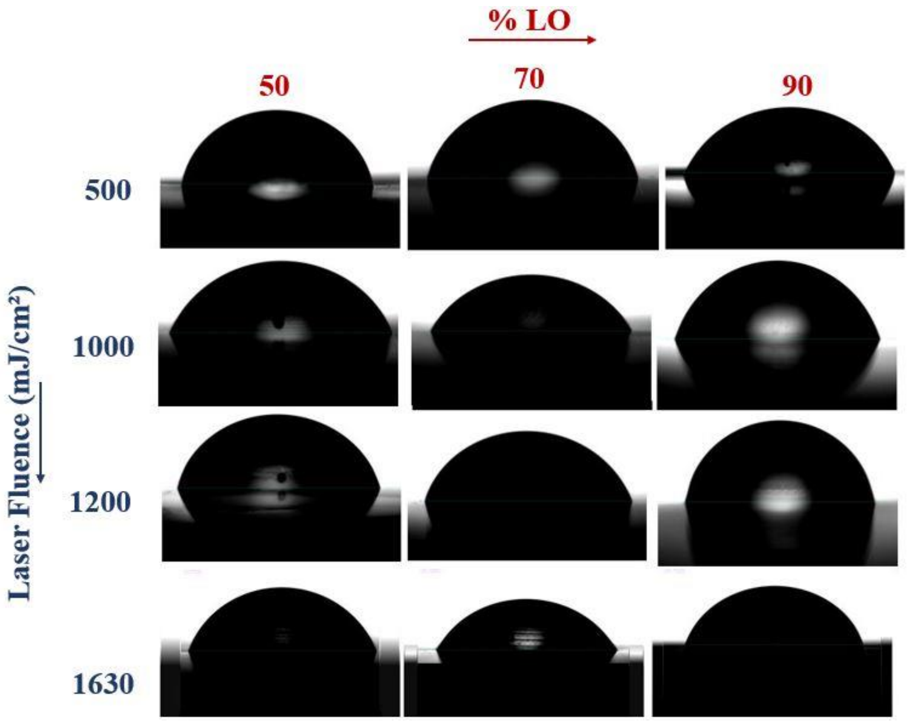

Fig 5.6: Images of water droplets on the surface for polyimide laser treated at fluences of 500mJ/cm^2, 1000 mJ/cm^2, 1200 mJ/cm^2, and 1630 mJ/cm^2 with varying % LO.

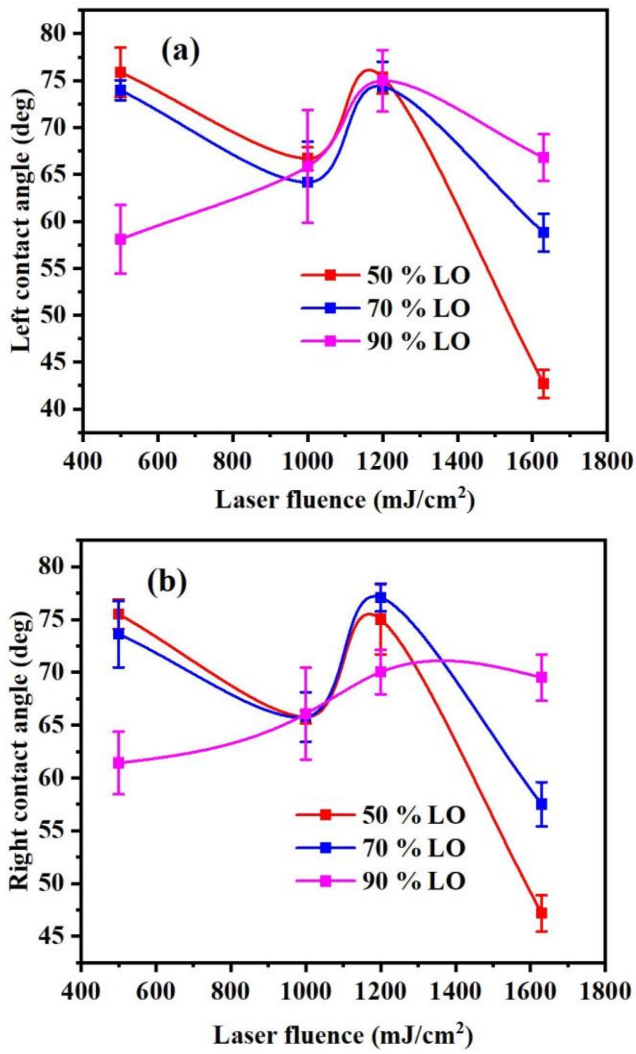

Fig 5.7: Contact angle measurements (a) Left and (b) Right, for polyimide laser treated at fluences of 500mJ/cm², 1000 mJ/cm², 1200 mJ/cm², and 1630 mJ/cm² with varying % LO.

The study of wettability or contact angle of the laser-annealed polyimide substrates can be instrumental in narrowing down to the highly suitable substrates for deposition from the several samples under consideration. The static contact angles for pristine polyimide were θ_1= 82° on the left side and θ_2 =82° on the right side. There has been a considerable reduction in the contact angle of polyimide after laser annealing at 500 mJ/cm^2 fluence at 90% LO, 1630 mJ/cm^2 fluence at 50% LO, and 1630 mJ/cm^2 fluence at 70% LO, as shown in fig 8. The obtained contact angles at the mentioned fluences and line overlaps are listed in table 6. The contact angles were higher at a laser fluence of 500 mJ/cm^2 with 50% and 70% LO owing to the loss of the hydrophilic ─OH group from the polyimide surface, which was indicated by increased transmittance in FTIR peaks in the 3450 to 3650 cm^{-1} range [67]. However, in the case of laser annealing at 500 mJ/cm^2 fluence at 90% LO, the reduction in contact angle may be due to the crystallized and roughened polyimide surface. The loss of the hydrophilic —OH group at 1000 mJ/cm^2 and 1200 mJ/cm^2 was too prominent to be compensated by surface crystallization, which eventually increases the contact angles. Annealing at 1630 mJ/cm^2 with 50% and 70% LO, the low contact angle was observed due to the material removal from the surface, also shown in section 3.2. At 1630 mJ/cm^2, an increase in % LO may have caused excess material removal, which caused a progressive reduction in contact angle.

Table 6: Static contact angles of laser-annealed polyimide utilized for deposition

Annealing parameter	Left contact angle (degrees)	Right contact angle (degrees)
500 mJ/cm^2 fluence at 90% LO	58.1±3.6	61.4±2.9
1630 mJ/cm^2 fluence at 50% LO	42.7±1.5	47.2±1.7
1630 mJ/cm^2 fluence at 70% LO	58.8±2.0	57.5±2.1

The reduction in wettability of polyimide has affected its adhesion characteristics with the deposited NiTi film, which was examined using the Scotch tape test. Fig 5.8 (b) shows the optical image of plain scotch tape of the mentioned size, which weighed 13 mg. The following images show that the film adhered to the tape after the test. The scotch tape was weighed before and after the test to quantify the material removed given in table 7.

Table 7: Weight of Scotch tapes before and after the test

Bimorph sample fabrication condition	Scotch Tape weight before the test (mg)	Scotch Tape weight after the test (mg)
Pristine polyimide	13	14
Polyimide annealed at 500 mJ/cm^2 and 90% LO	13	17

Polyimide annealed at 1630 mJ/cm^2 and 50% LO	13	14
Polyimide annealed at 1630 mJ/cm^2 and 70% LO	13	13

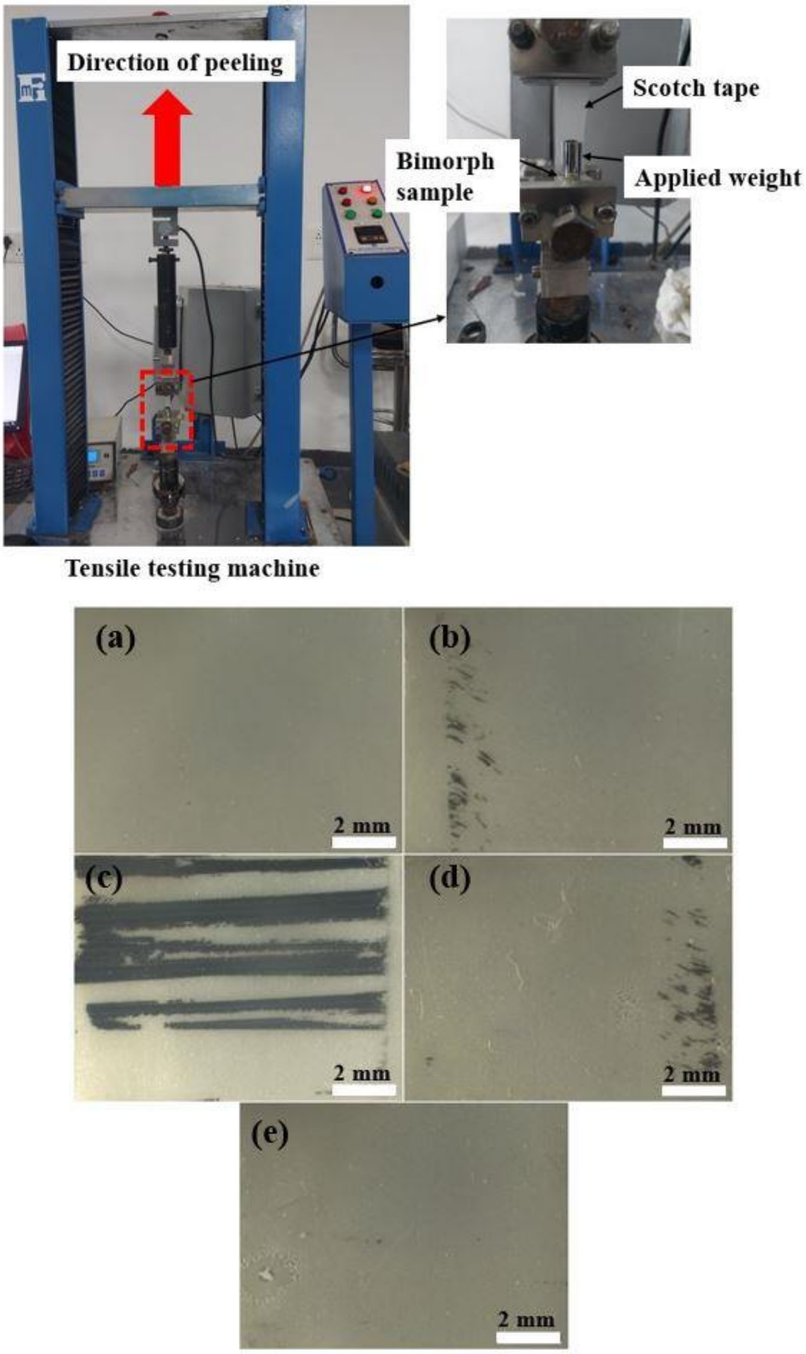

Fig 5.8: Tensile testing machine used for peeling of scotch tape. Optical images of scotch tape (a) Before test and after testing on bimorph fabricated on (b) pristine polyimide (c) polyimide annealed at 500 mJ/cm^2 with 90% LO (d) polyimide annealed at 1630 mJ/cm^2 with 50% LO (e) polyimide annealed at 1630 mJ/cm^2 with 70% LO.

The bimorph fabricated on pristine polyimide and the polyimide annealed at 1630 mJ/cm^2 and 50% LO exhibit similar adhesion with the removal of 1 mg material from the film. Annealing at 500 mJ/cm^2 with 90% LO resulted in the most negligible film adhesion, as the Scotch tape test removed the highest amount of film from the bimorph. Furthermore, the bimorph fabricated on polyimide treated at 1630 mJ/cm^2 with 70% LO does not exhibit a measurable film removal during the test. This may be because the polyimide laser annealed at 1630 mJ/cm^2 with 70% LO has displayed a combination of the rough surface and crystalline domains, as mentioned in sections 5.2.1 and 5.2.2. This combination has facilitated a better interaction between the polyimide surface and the deposited NiTi thin film. The mentioned sample has manifested significant improvement in actuation and adhesion characteristics.

5.2.5 Electrical Actuation

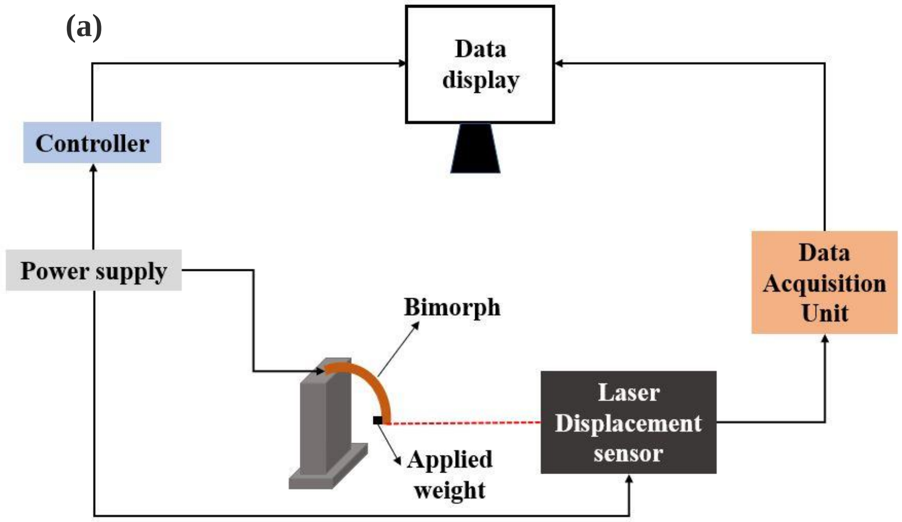

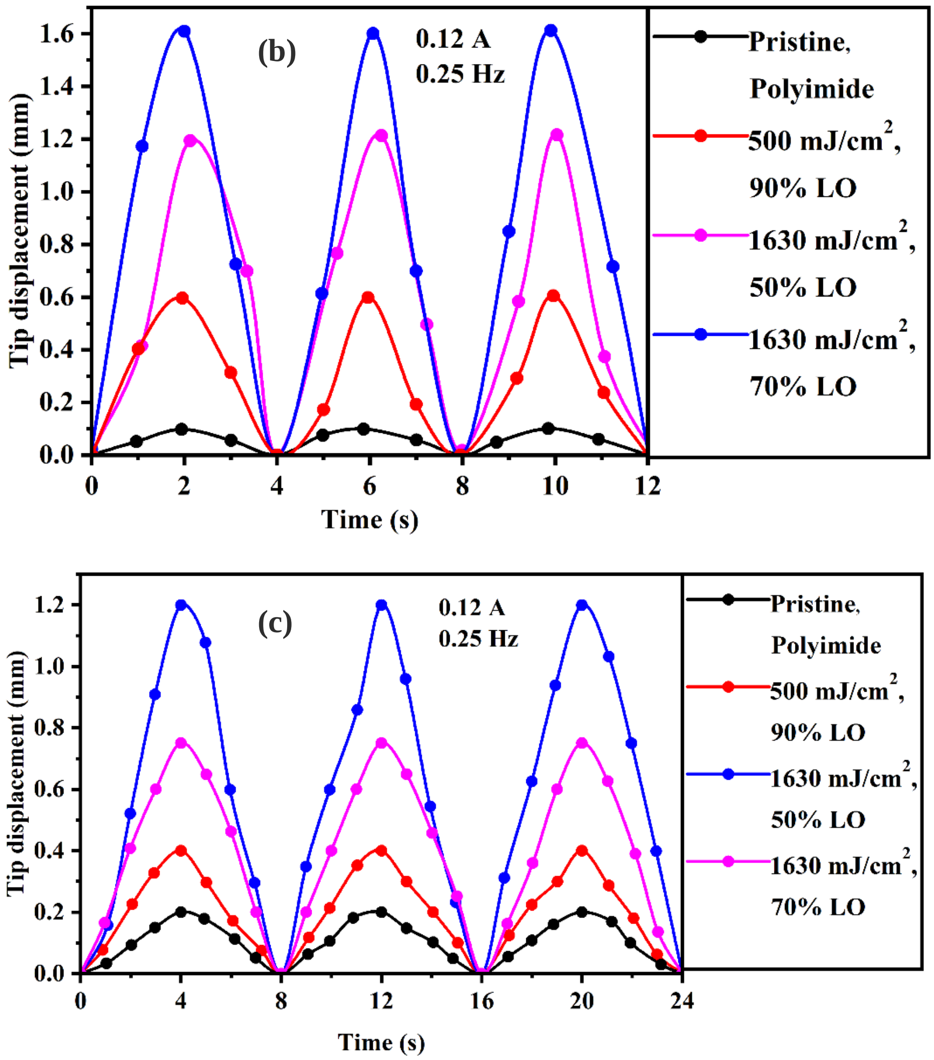

Fig 5.9: (a) Setup for studying electrical actuation of NiTi/ Kapton polyimide bimorph. Electrical actuation study of NiTi/Kapton polyimide bimorph fabricated on pristine and laser-annealed polyimide (b) without external weights and (c) with external weights.

The electrical actuation has been studied for bimorph fabricated on pristine polyimide and on laser annealed polyimide at a fluence of 500 mJ/cm^2 with 90% LO, 1630 mJ/cm^2 with 50% LO and 1630 mJ/cm^2 at 70% LO. The bimorph drew a maximum current of 0.12 A at a 20 V supply, which was used for the measurements. Further increment in the voltage led to the excess drawing of power by bimorph, thereby burning the bimorph. The results of the electrical actuation study without external weights are shown in fig 5.9 (b). The maximum tip displacement observed for bimorph with pristine polyimide substrate was 0.1 mm. Laser annealing of the substrate has helped improve the deposited film quality, which is evident from the increase in tip displacements. The displacements observed for bimorph with substrate laser annealed at a fluence of 500 mJ/cm^2 with 90% LO, 1630 mJ/cm^2 with 50% LO and 1630 mJ/cm^2 at 70% LO were 0.62 mm, 1.2 mm, and 1.6 mm respectively.

The mirror to be placed on the bimorph tip in the Stewart platform configuration weighed 45 mg. The exact weight was considered for actuation analysis with the application of external weight, as shown in fig 5.9 (c). The bimorph fabricated on the polyimide annealed at 1630 mJ/cm^2 and 50% LO has achieved a maximum tip displacement of 1.2 mm with the application of 20 V. However, the tip displacement was reduced in the other two laser-annealed samples. The application of external weight has affected the actuation of the bimorph due to the inertial effects. Moreover, the actuation frequency was halved from the unloaded test condition to achieve the maximum tip displacement. The tip displacement was nearly halved at the same actuation frequency as the unloaded condition.

5.3 Summary

The NiTi/polyimide was fabricated using the thermal evaporation technique. The study aims to investigate the impact of laser annealing on the polyimide substrate using 355 nm Nd: YAG laser, leading to better deposition quality and actuation characteristics. The results of the study are listed below:

- The laser fluence up to 1200 mJ/cm^2 at all % LO has created crystalline domains on the polyimide surface. No crystalline peaks were observed at a laser fluence of 1630 mJ/cm^2 and 50% LO indicating the removal of the top layer. Crystallinity again increases at 70% LO.
- The progressive increase in laser fluence induced the loss of surface molecules, which was indicated by an increase in transmittance. A similar pattern was observed at constant laser fluence with increasing % LO.

- The contact angles of polyimide annealed with 500 mJ/cm^2 fluence at 90% LO and 1630 mJ/cm^2 at 50% LO and 70% LO were 58.1°±3.6°, 42.7°±1.5°, and 57.5°±2.1° respectively, which are considerably less compared to pristine polyimide.
- The bimorph fabricated on the polyimide annealed at 1630 mJ/cm^2 and 70% LO exhibited the best adhesion between substrate and film, as no film was removed during the Scotch tape test.
- The electrical actuation shows a drastic increase in tip displacement of 0.1 mm for bimorph fabricated on pristine polyimide to 1.6 mm for bimorph fabricated on polyimide annealed at 1630 mJ/cm^2 and 70% LO. The application of external weights has reduced tip displacement in all the samples except for bimorph fabricated on polyimide annealed at 1630 mJ/cm^2 and 50% LO.
- The promising results of actuation tip displacement at both unloaded and loaded conditions can be further utilized for mechanisms in Opto mechatronics applications such as the Stewart platform.

Chapter 6

This chapter describes the application laser assisted micromachining on bimorph structures for customized mirror and actuator fabrication.

Laser Assisted Micromachining of NiTi/Kapton Polyimide bimorph towards fabrication of Microactuators

6.1 Fabrication

6.1.1 Pellet Fabrication

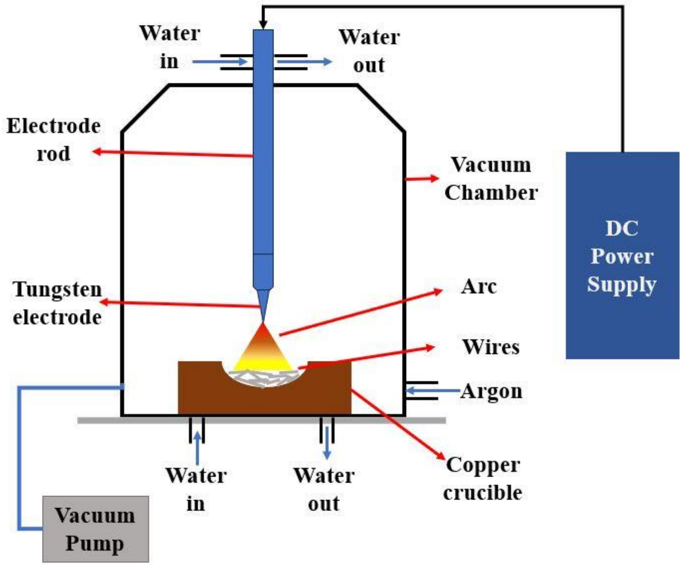

Fig 6.1: Pellet fabrication of NiTi with Vacuum Arc Melting

NiTi wires (45.8% Ti by weight) and pure Ti wires of size 4 mm x 1.2 mm were used to fabricate the pellets which were used as primary source materials for deposition. Fig 6.1 illustrates the schematic and for the fabrication of pellets of weight 1.5 g using a vacuum arc melting unit (Hydro Pneo Vac Technologies). The wires were placed in a copper crucible, which was water-cooled. The crucible is a part of a vacuum chamber in which a vacuum of 0.03 kg/cm^2 was created initially, and then argon was supplied to reach 0.53 kg/cm^2. The NiTi pellet formation was achieved at a supply voltage of 25 V and 150 A current. The lower vapor pressure of Ni than Ti brings about a higher deposition rate of Ni and leads to Ni-rich compositions of deposited thin film. This loss of Ti during deposition was compensated by adding excess Ti to the source material during pellet formation. Pellets with compositions of NiTi: Ti=80:20 (by weight) were employed for deposition.

6.1.2 Thin Film Deposition

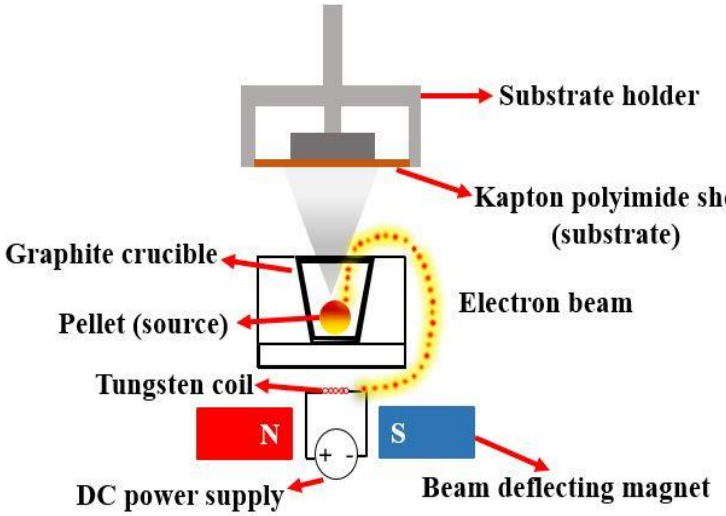

Fig 6.2: NiTi thin film deposition with E-beam deposition.

The thin film of NiTi shape memory alloy (SMA) was deposited on Kapton polyimide substrates by utilizing the E-beam evaporation technique (Hydro Pneo Vac Technologies). The Kapton polyimide substrate of thickness 75 µm was held in the deposition chamber in the form of belts of size 180 mm x 30 mm. The deposition was performed in the chamber with a 2 x 10^{-5} mbar pressure. The NiTi pellet fabricated by vacuum arc melting was placed in the graphite crucible. The tungsten coil shown in Fig 6.2 was supplied with a voltage of 4.2 kV and 190 mA to generate the electron beam. The generated electron beam was directed to the source material in the graphite crucible with the help of beam-deflecting magnets. The deposition was carried out for 260 seconds to fabricate the NiTi/Kapton polyimide bimorph structure.

6.1.3 Laser Assisted Micromachining

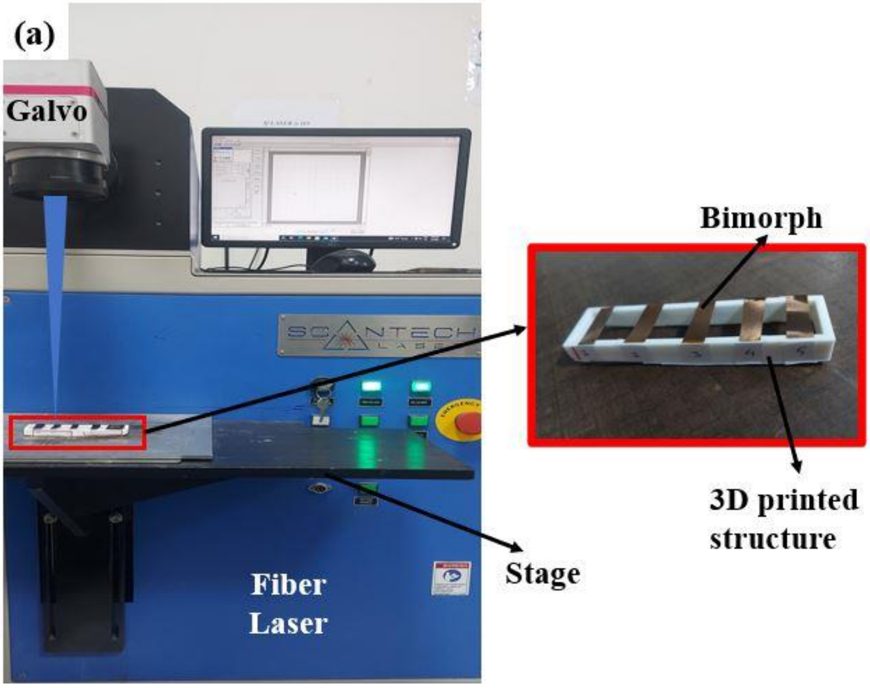

Fig 6.3: Laser Assisted Micromachining of bimorph structure with Fiber Laser.

The fabricated bimorph structure was pasted on 3D printed structures of dimensions 24 mm x 100 mm x 10 mm with a wall thickness of 2 mm. The schematic of the laser micromachining setup is depicted in Fig 6.3. The laser micromachining was performed using a 1064 nm fiber laser (Scantech laser) with a focused spot size of 50 µm. The maximum power output of the laser was 50 W. The laser head is equipped with a focusing lens and a galvo. The motion of the laser beam is controlled by galvo as per the input fed. A single line cut was attempted using varying laser power (LP), laser speed (LS), spot diameter (SD), and laser travel direction (LT) to determine the optimized micromachining parameters. As the laser performs micromachining in a raster scan pattern, the study was attempted by employing transverse and longitudinal directions of laser travel. The laser scanning of the bimorph in a raster pattern was considered to be in the transverse direction of laser travel. Furthermore, when the laser scanning direction was perpendicular to transverse, it was termed the longitudinal direction of laser travel. It was termed longitudinal as only a single line scan was achieved, as shown in Fig 6.4.

Minitab software optimized the micromachining parameters using the DOE (Design of Experiments) module.

6.2 Design of Experiments

6.2.1 Input Parameters

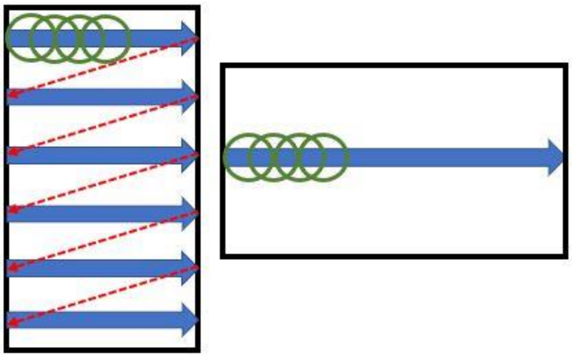

Fig 6.4: Different strategies of laser motion during micromachining.

Table 8: Different input laser parameters for design of experiments of micromachining

Parameter	Type	Values
Laser Power (W)	Numeric	3, 5, 7, 9
Laser Speed (mm/s)	Numeric	4, 5, 6
Spot Diameter (µm)	Numeric	50, 90
Laser Travel Direction	Text	T, L

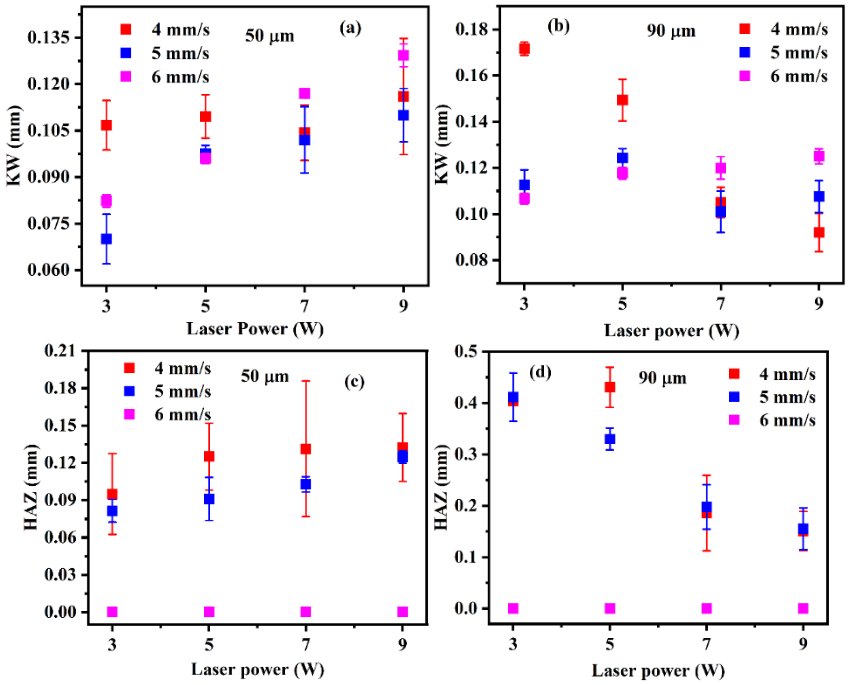

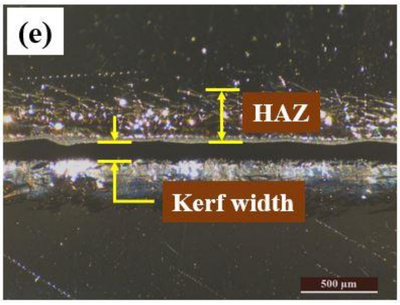

Fig 6.5: (a) and **(b)**Variation in kerf width and **(c)** and **(d)** heat affected in the bimorph at varying laser speeds and laser fluences with transverse direction of laser travel. © Depiction of kerf width and HAZ generated after micromachining.

Figure 6.5 (a) and (b) illustrate the variation in measurements of kerf width with varying laser power (LP) and laser speed (LS) for spot diameter (SD) of 50 μm and 90 μm, respectively. The single-line micromachined on the bimorph was performed with a transverse direction of laser travel (LT). The micromachining input parameters were selected based on existing literature on the laser cutting of polymers. The popular inputs have been LP, LS, and SD; however, in this study, the motion of the laser beam will be changed frequently for customized actuator fabrication, and thus, the direction of laser travel (LT) can also prove to be an important factor. The micromachining was attempted at a laser power of 3, 5, 7 and 9 W with laser speeds of 4, 5, and 6 mm/s to study the effects on kerf width (KW) and heat affect zone (HAZ) after micromachining. Kerf width is usually the effective width of the cut generated on the workpiece due to laser interaction. Heat affected zone in this study was limited to the region where the changes in the deposited film, such as roughening, cracks, delamination, and bulges, were observed. Figure 6.5 © depicts the kerf width and HAZ considered in this study. Measurements were taken at micromachined edges on 3 different locations, and the resulting average and standard deviations of KW and HAZ were plotted in figs 6.5 and 6.6. The micromachining was aimed to create accurate features with negligible or no damage to the surrounding film so that the finally fabricated actuator could be a ready-to-use product. Thus, both KW and HAZ were prime factors in determining the quality of the fabricated actuator, which were considered as outputs during the study.

Figure 6.5 is illustrating the variation in kerf width and HAZ at different laser parameters for transverse direction of laser travel. The raster scanning pattern of the laser beam can create higher variation in the KW and HAZ values. Additionally, the high values of standard deviation were observed for the laser speed of 4 mm/s. The combined effect of raster scanning and less scanning speed resulted in higher heat interaction with the thin film. As the deposited film is a shape memory alloy material, the heat interaction for longer duration induces phase transformation which brings about the actuation of the bimorph during the micromachining. Even the small amount of actuation during the laser interaction can create significant deviations in the output KW and HAZ. The KW at 50 μm SD ranges from 0.062 mm to 0.133 mm, which increases for 90 μm SD ranging from 0.092 mm to 0.175 mm. A similar effect of increase in spot size has been seen on HAZ, as shown in fig 6.5 © and (d), where 50 μm SD produces HAZ from 0.0625 mm to 0.186 mm and 90 μm SD creates 0.113 mm to 0.469 mm HAZ. The HAZ measurements for 4 mm/s and 5 mm/s laser speed have significant values, while 6 mm/s LS does not generate significant HAZ. High LS reduces the interaction time of laser with bimorph, which results in insignificant HAZ in view of the study. Also, the same LS could not generate a through cut even at 9 W laser power, creating microchannels.

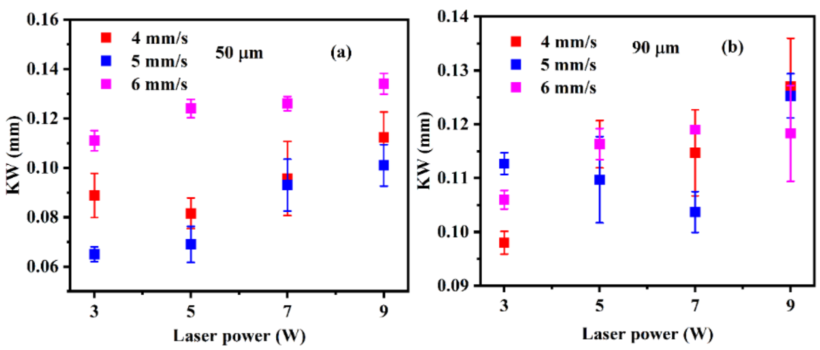

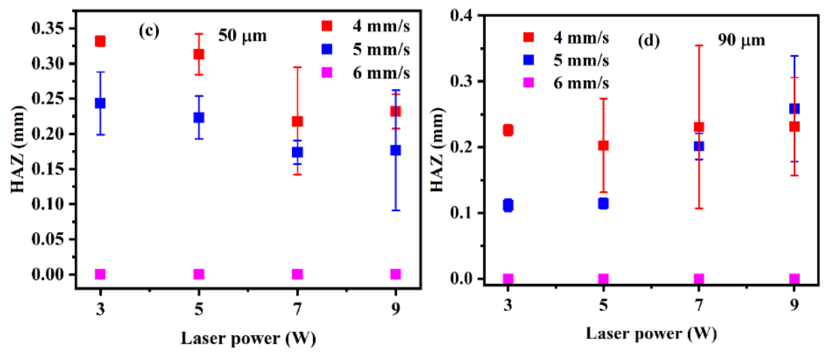

Fig 6.6: **(a)** and **(b)**Variation in kerf width and **(c)** and **(d)** heat affected zones (HAZ) in the bimorph at varying laser speeds and laser fluences with the longitudinal direction of laser travel.

Micromachining was also performed using the longitudinal direction of laser travel (LT) at all the parameters mentioned previously in this section. Figure 6.6 (a) and (b) represent the variation in measurements of KW with varying LP and LS for SD of 50 µm and 90 µm, respectively. The KW ranges from 0.062 mm to 0.138 mm for 50 µm SD and from 0.0959 mm to 0.133 mm for 90 µm. For longitudinal LT, the KW increases with SD, similarly to transverse LT. The increment in SD has increased the effective area of interaction of the laser beam with the bimorph, resulting in higher KW[68]. Similar to the transverse direction of laser travel, at 6mm/s LS, microchannels were created at all powers owing to only removing the deposited film. Lower speeds could generate micromachining cuts at all powers with varying degrees of KW and HAZ.

The HAZ variation for the input LP, LS and SD for longitudinal LT are depicted in fig 6.6 (c) and (d). For 50 µm SD, the HAZ varies from 0.09 mm to 0.342 mm and from 0.102 mm to 0.338 mm for 90 µm SD. The average HAZ has increased with SD for both transverse and longitudinal LT due to a higher area of energy interaction. Due to a more significant interaction area, the microchannels formed at 6 mm/s have a higher average KW for a 90 µm SD. The study further investigated the effect of the input process parameters on the KW and HAZ, finally leading to an optimized set of micromachining parameters. This was brought into effect by using the design of experiments explained in the further sections.

In this study, the effect of multiple input parameters on more than one output variables were investigated to achieve the optimum working condition. Micromachining of thin films with fiber laser depends on process parameters such laser power, laser speed, spot diameter and direction of laser travel. Design of Experiments has been one of the most efficient methods in the past studies to derive logical relationship between multiple input and multiple output parameters[69]. It provides a structured way of conducting the experiments involving multiple factors to identify optimal working conditions. Interestingly, the most influential input parameter of the can also be determined by analysing the experimental results. Thus, Design of Experiments has been employed in this work with four input parameters discussed in the previous section, namely LP, LS, SD, and LT, which were considered for studying the variation in the output parameters, i.e., KW and HAZ. LP has 4 levels, LS has 3 levels, SD has 2, and LT has 2. The input micromachining parameters are illustrated in the table 1. As the levels of input parameters were not the same, a full factorial design of the design of experiments was used to study the effects of multiple controlling parameters on the response or output variables. Furthermore, each micromachining condition has 3 replicates to increase the precision of the output. Replication also aids in drawing satisfactory conclusions about effects and interaction. The parameter selection for micromachining of the bimorph with laser was done in random order so that the levels of input factors should be changed after every run. Such kind of parameter selection is termed as randomization of experiments which is done to reduce the bias in the results arising from the external factors that can influence the experiments. Further it reduces the influence of current experimental run on the output of future experiments. The obtained data was analyzed to study the effects and interaction between the input parameters and arrive at the optimal micromachining condition.

6.2.2 Pareto Chart

The Pareto chart was used to determine the significance of any effect on the output in consideration. The effects extending past the reference line signify that it significantly impacts the output and is vital with 95% confidence. The standardized effects were plotted in the decreasing order of absolute values. The representation of the input parameters in Pareto chart are given in Table 9. Two separate charts were plotted for KW and HAZ, as shown in Fig 6.7. The reference lines of the chart for both KW and HAZ were 2.069.

Table 9: Parameters in Pareto chart

Input Parameter	Factor in Pareto chart
Laser Power (LP)	A
Laser Speed (LS)	B
Spot diameter (SD)	C
Laser Travel direction (LT)	D

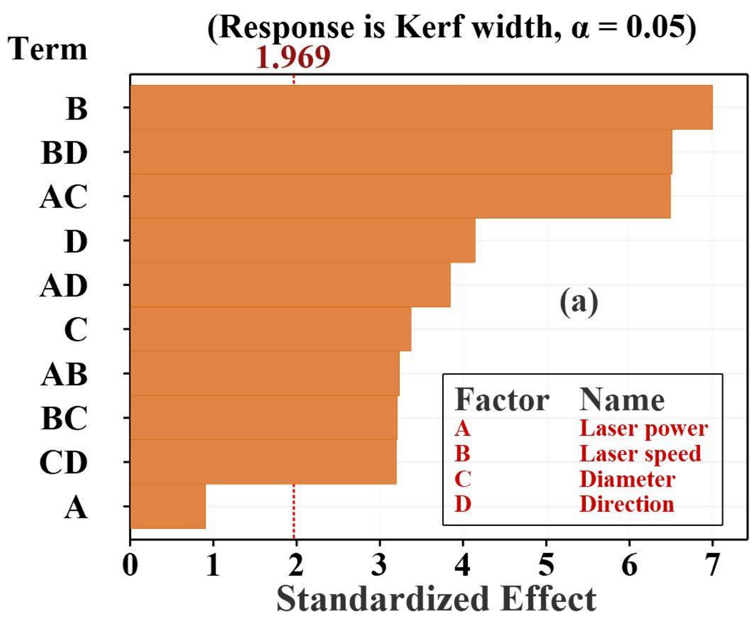

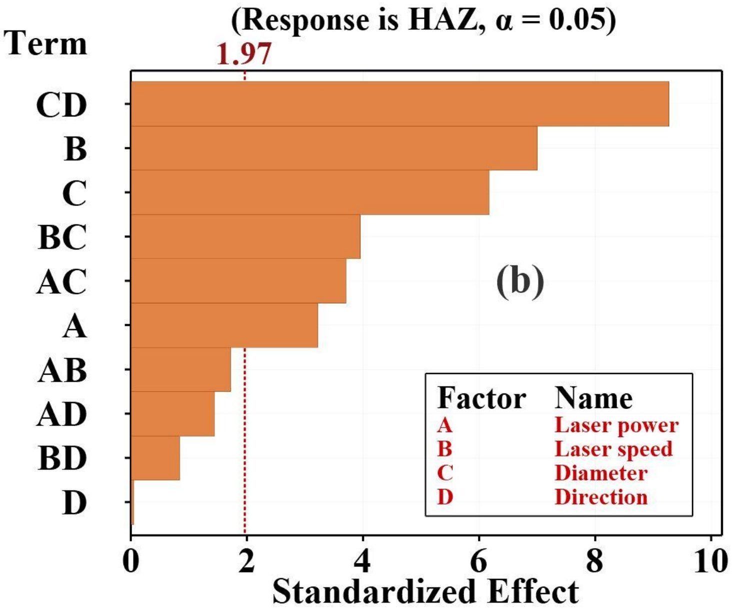

Fig 6.7: Pareto Chart for (a) Kerf width and (b) HAZ.

Figure 6.7 (a) depicts the Pareto chart for KW, which suggests that LP up to 9 W is individually ineffective towards the variation of the KW. Higher laser power results in excess energy interaction with the bimorph structure, producing carbonized edges after micromachining. As the high laser energy interacts with the polyimide substrate, it induces chemical degradation, producing smoke and carbonaceous particles, which remain at the micromachined edge and can deposit on the actuator surface[70]. The two most influential individual inputs for KW were LS and SD[71]. Considering the Pareto chart of kerf width only, the input parameter of laser power can be screened out. However, the importance of the input parameters for the cut generation can be finalized after the studying their influence on both HAZ and KW. It can be inferred from Fig 6.7 (b) that LS was the most influential factor for HAZ variation[71]. In view of the Pareto charts of both KW and HAZ, the input parameters LS and SD were individually most influential which will be discussed in section 6.2.3. The subsequent section studies the level of influence of the input parameters on the response and the relative strength of the effects.

6.2.3 Mains and Interaction Plots

The main effects plot is the plot of the mean output of the process at all levels of the input parameters for each parameter individually. It determines the significance of the input parameters for the generated output. The impact of a parameter is determined by the inclination of the line created in the plot. A horizontal line indicates no effect of the input parameter on the output, while as the inclination of the line from the horizontal increases, the effect increases.

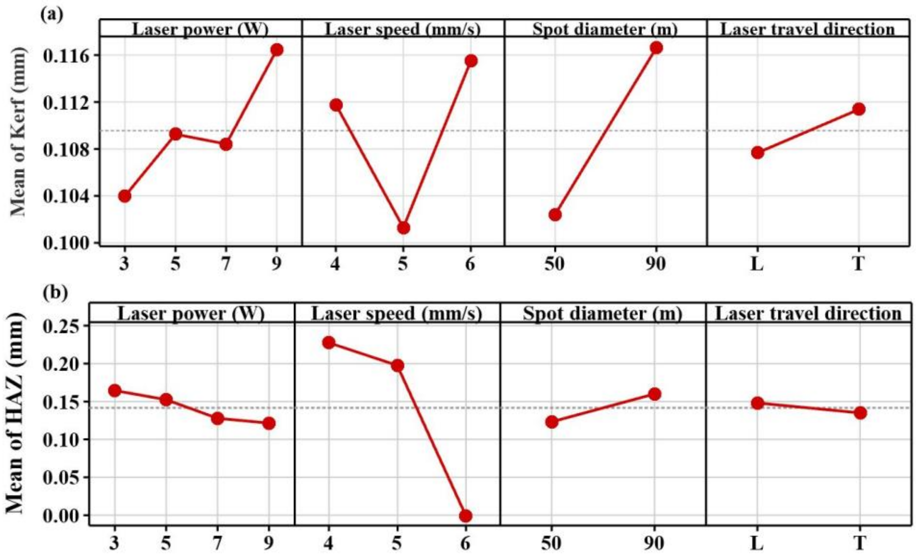

Fig 6.8: (a) Main effect plot of KW **(b)** Main effect plot of HAZ.

The main effects plots for the KW and HAZ are illustrated in Fig 6.8. Increment in LP has increased the KW, as indicated by a high inclination of the mean line for LP in Fig 6.8 (a). However, the effect of LP on HAZ was minimal, as shown by the lower inclination of the mean line of LP in Fig 8 (b). Both KW and HAZ were highly influenced by LS and had the least values for the micromachined edge for 5 mm/s LS. The negligible HAZ observed was in the case of 6 mm/s LS, which is also mentioned in section 6.2.1.

Furthermore, SD variation highly influenced KW while minimally changing the HAZ. The Pareto chart observed the same result, where LS was a significant parameter for KW variation. The increase in SD from 50 μm to 90 μm has increased the KW from a mean value of 0.102 mm to 0.117 mm. The study's least effective parameter was LT, as it has minimal effect on both KW and HAZ. This ineffectiveness is a desirable condition as, further in the study, we fabricated customized actuators with frequent changes in LT. Thus, the effect on KW and HAZ of the actuators was similar, irrespective of the direction of motion of the laser.

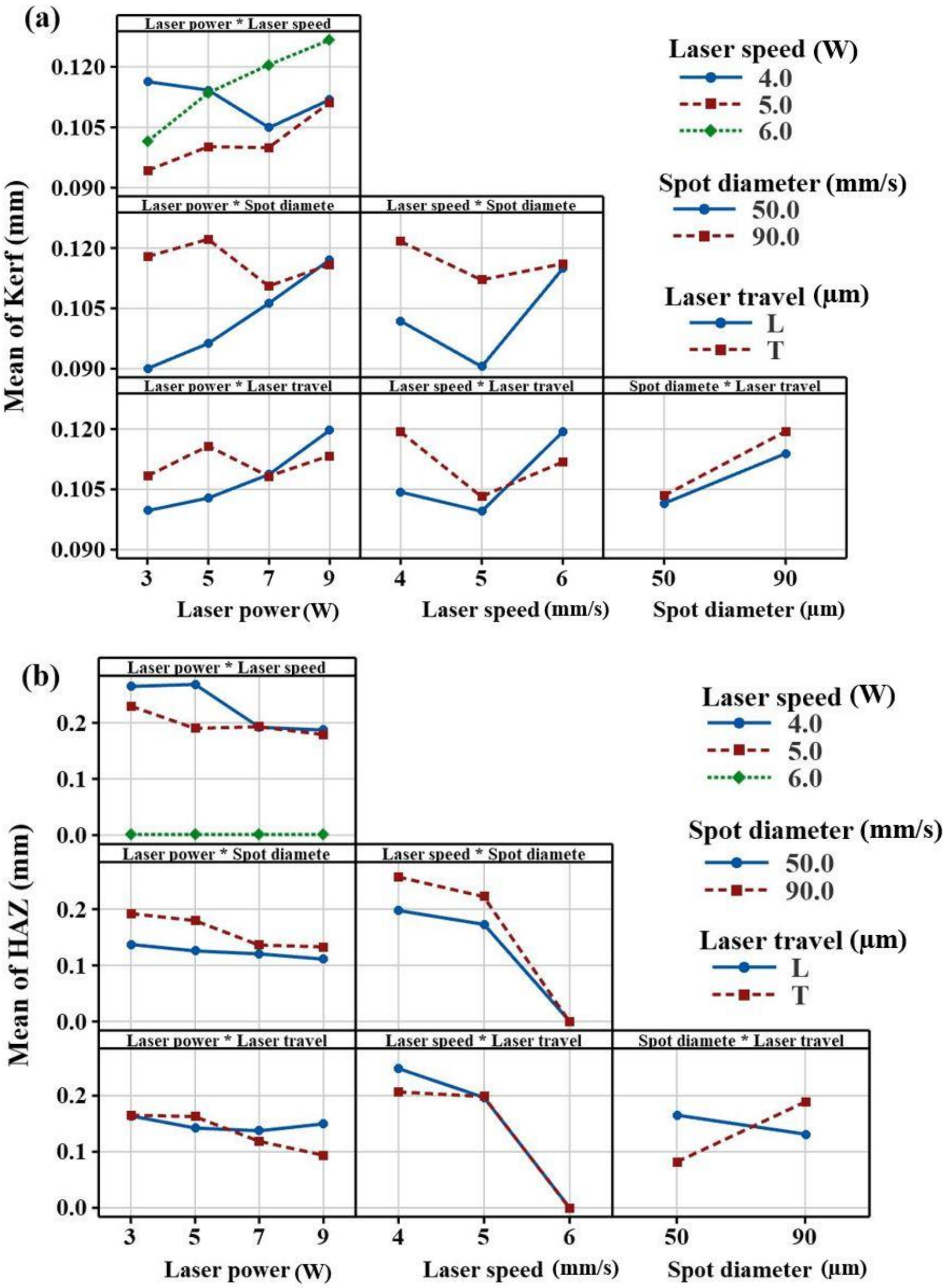

Fig 6.9: (a) Interaction plot of kerf width **(a)** Interaction plot of HAZ.

Figure 6.9 illustrates the interaction plot of the KW mean, which shows the relationship between input and observed responses. Parallel lines indicate that the interaction does not significantly affect the output[72].

Intersecting lines suggest a considerable impact of the interaction on the output. The interaction of LP and LS was significant at high LP and low LS values. Similar behavior has been observed for the interaction of LP with SD and LT. Furthermore, the combination of LS with SD and LT has significance at high values of LS for output KW.

The interaction plots of the second important output variable, i.e., HAZ, are shown in Fig 10. The interaction of SD and LT has been most significant for HAZ, although the individual parameters were least effective. Minimum HAZ was achieved at 50 μm SD and transverse LT. Unlike KW, HAZ was affected by low LP and LS values. At high LP, the variation in LS was less significant on the HAZ variation. Also, the combination of LP with SD and LT was ineffective on HAZ due to the minimal slope between the lines.

6.2.4 Microchannels formation

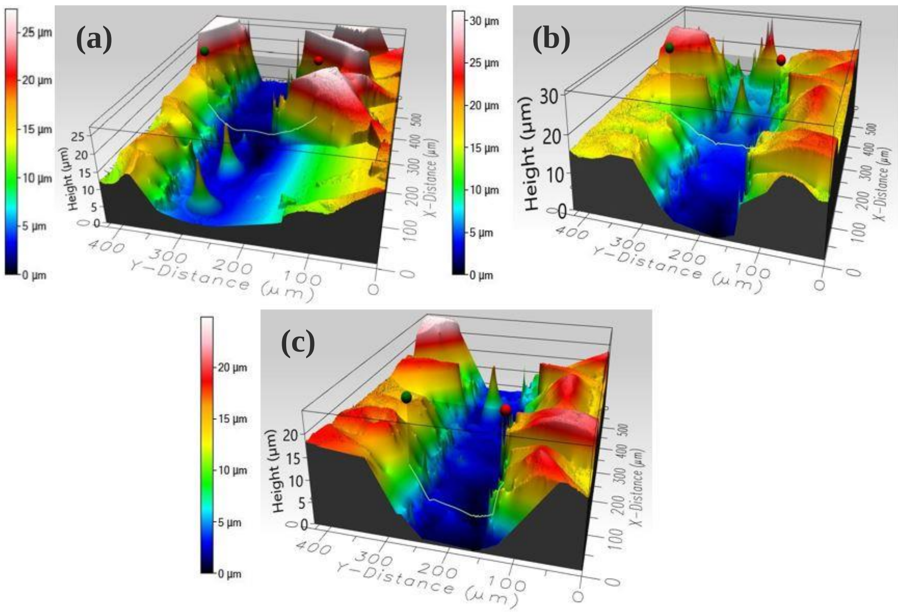

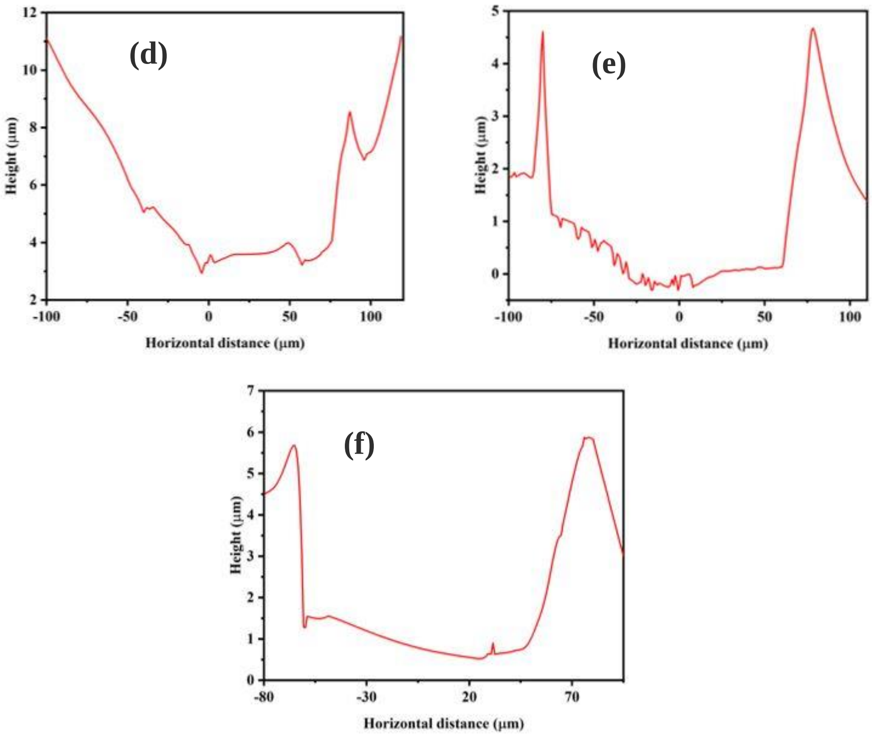

Fig 6.10: (a), (b) and (c) Optical profilometer measurements of the microchannels formed at laser speed of 6 mm/s. (d), (e) and (f) Measured depth of the micromachined channels.

As mentioned in previous sections, the micromachining attempted at 6 mm/s laser speed with all the processing conditions was unable to produce a through cut. However, microchannels were created on the bimorph by removing only the film, as shown in Fig 6.10 (a), (b) and (c). Due to high laser heat absorption near the micromachined channels, bulge and irregularity in the film have been observed, although the width of this heat-affected zone was less than 100 µm. The dimensions of the microchannel feature and the associated HAZ at a laser speed of 6 mm/s are illustrated in Fig 6.10 (c), (d) and ©. The micromachined channels' width varies from 105 µm to 134 µm. The bulged height increased with the laser power. The depth of the micromachined channels was more than 15 µm, but the deposited film was around 1.3 µm thick. This suggests the removal of polyimide along with deposited NiTi film from the microchannel region.

6.2.5 DOE verification and shape cutting

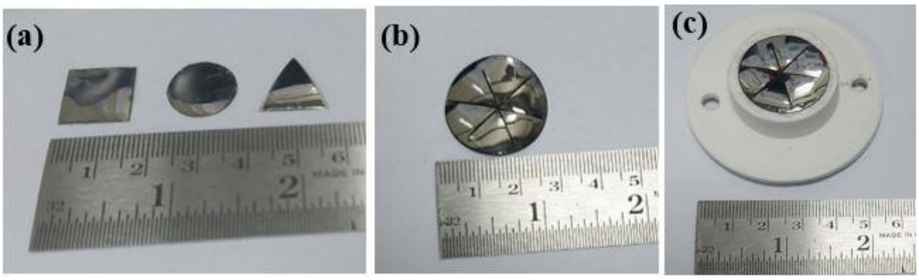

Fig 6.11: Different shapes fabricated out of bimorph structure at optimized laser micromachined parameters.

The optimized micromachining parameters were obtained using the design of experiments. The results for micromachining of a single line indicate that the optimized direction of micromachining was transverse; however, the variation in KW and HAZ with a change in laser travel direction was negligible. Thus, both cutting directions were feasible, which creates the possibility of micromachining of different shapes, as shown in Figure 6.11. Square and triangle of sides 15 mm and circle of diameter 10 mm were micromachined from the bimorph at the optimized parameters of 5 W laser power (LP), 5 mm/s laser speed (LS), and 50 µm spot diameter (SD), to confirm the feasibility of the process. Further, a customized shape was micromachined aimed at the application as an optical shutter. The shape was a 22 mm diameter circle with 6 nos. flaps (actuators) micromachined in a single pass of the fiber laser. The customized shape was pasted on a 3D printed structure, as shown in Fig 6.11 (c), to be used as an optical shutter.

6.3 Material Characterization

6.3.1 Film Thickness

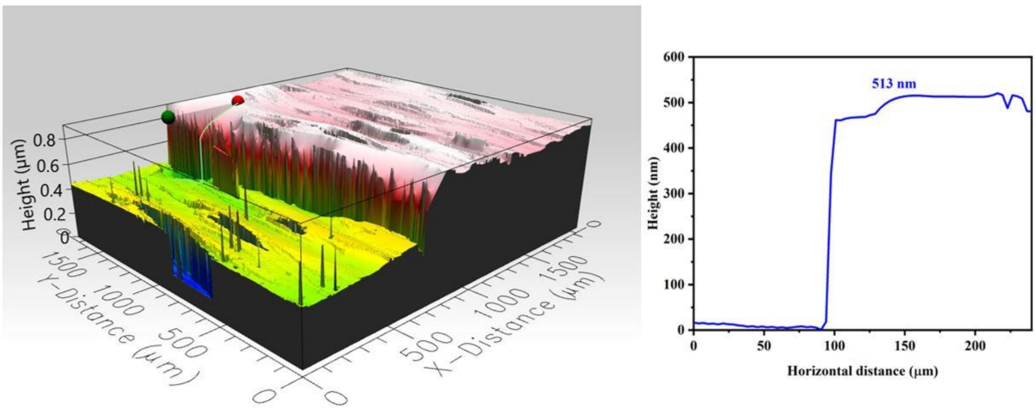

Fig 6.12: Measured thickness of the deposited NiTi on the Kapton polyimide substrate.

The thickness of the deposited NiTi film was measured with a 3D optical profilometer. The optical profilometer is based on the principle of optical profilometry and thus, requires the surface of the samples to be reflective for measurements. As the Kapton polyimide surface was not reflective in nature, the film thickness measurement was done on silicon wafer. The wafer was placed in the deposition chamber during the fabrication of bimorph structure and the deposition thickness was measured on the same which was found to be 513 nm as shown in fig 6.12.

6.3.2 Surface Morphology and Composition

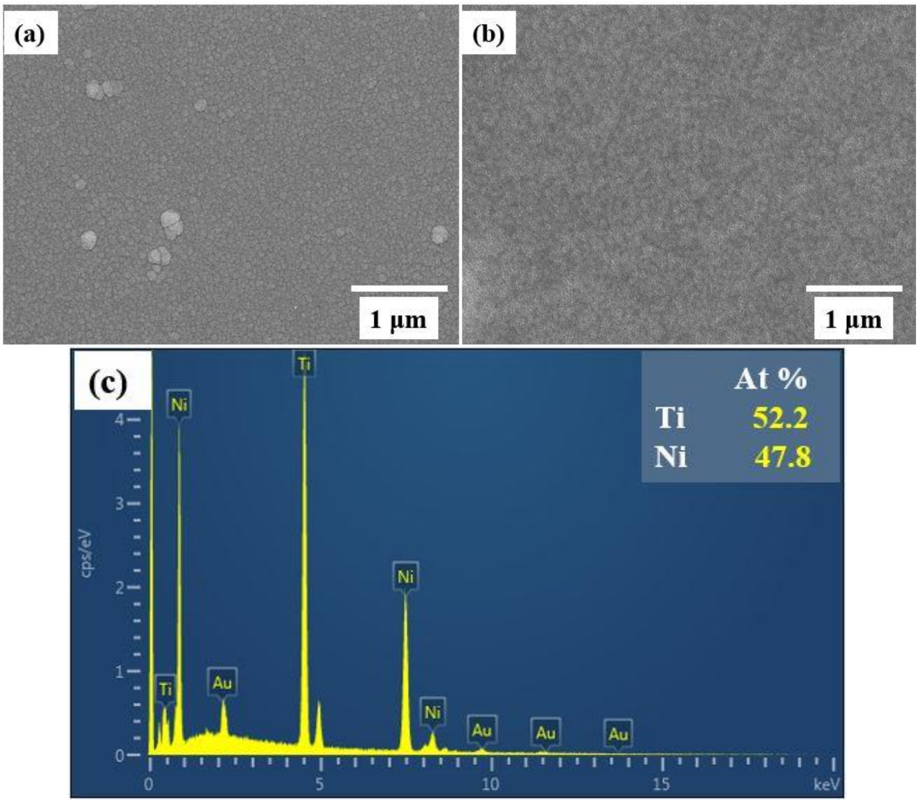

Fig 6.13: Morphology of the deposited NiTi film at **(a)** the center of the optical shutter actuator and **(b)** Near the micromachined edge. **(c)** Composition of the deposited film.

Figure 6.13 shows the SEM images of the NiTi film deposited on the polyimide substrate. At the center of the actuator, the film's grain is coarse illustrated in Fig 6.13 (a). However, the heat interaction of the laser beam at the micromachined edges has induced grain refinement.

Thus, the grains near the micromachined edges in the HAZ region were finer, as illustrated in Fig 6.13 (b). The formation of grains in the film suggests dense deposition, which produces a mirror-like surface of the bimorph and can affect the negligible transmittance of incident light required for optical shutter application. The elemental composition was checked with EDS (Electron Dispersive X-ray Spectroscopy) analysis as shown in fig 6.13 (c). The deposited film contains 52.2 % Ti and 47.8 % Ni. The deposited film was Ti-rich owing to the usage of excess Ti content during the deposition process. Since the deposited film was thin, it was coated with a thin uniform layer of Au before the SEM and EDS analysis to achieve better conductivity of the bimorph. An electron beam with high voltage (20 kV) was incident on the sample during the compositional analysis. Less conductivity of the sample leads to accumulation of electrons on the samples which creates localized charging and image gets blurred. To make the surface more conductive to facilitate the movement of electrons and improve the clarity of images of the samples, Au coating was performed. Thus, Au was observed during the compositional analysis of the samples. In the actual bimorph and micromachined actuator Au was not present.

6.3.3 Structural Analysis

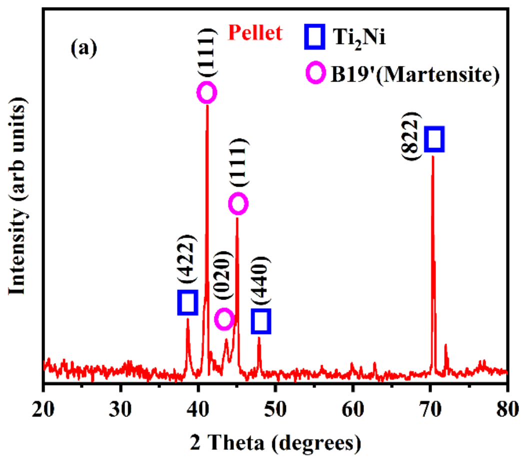

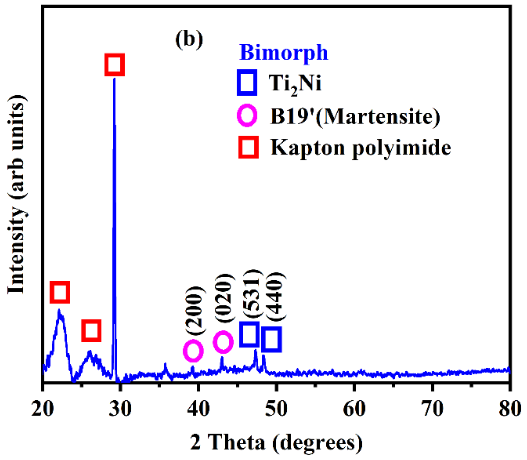

Fig 6.14: XRD analysis of **(a)** Pellet used for deposition and **(b)** Fabricated bimorph optical shutter.

The crystal structure of the pellet utilized for deposition and the deposited film were analysed to study the phases present in the two. The NiTi: Ti pellet formed with a source material ratio of 80:20 using vacuum arc melting was scanned at a 10°/min scanning rate. The pellet shows the presence of Ti_2Ni and B19′ phases, as shown in fig 6.14 (a)[73]. The micromachined bimorph actuator film deposited from the same pellet was considerably less crystalline compared to the pellet, as shown in Fig 6.14 (b). Fast scanning of bimorph results in error and shows peaks of polyimide substrate only due to less thickness of deposited film. Thus, the scanning was done at a slower rate of 2°/min. The structural analysis of the actuator shows that both Ti_2Ni and B19′ phases were still present in the film, as indicated by peaks at 43.11° and 48.25°. The phase B19’ refers to Twinned Martensite phase of the shape memory alloy film with monoclinic crystal structure. It refers to low temperature phase of SMA which on stress application changes the orientation to Detwinned Martensite. Visible actuation of the SMA film can only be observed when phase transformation occurs between low temperature Detwinned Martensite phase and high temperature B2 (Austenite) phase[74],[56]. In current study, the NiTi SMA film was deposited on the Kapton polyimide substrate. Small size of the bimorph structure does not have significant curvature thereby inducing no stress on the film. Thus, low temperature phase observed was B19’ during the XRD analysis. The sharp peak before 30° was due to the crystallization of the polyimide substrate[58]. The two humps observed before 30° correspond to the amorphous regions of Kapton polyimide.

6.3.4 Transmittance and Phase Transformation Study

The study was conducted to determine the phase transformation characteristics using differential scanning calorimetry (DSC). The test was conducted for a temperature range of -80 °C to 200 °C with heating and cooling rates of 10 °C/min. The DSC was conducted in a nitrogen purged environment and the samples weighed 11 mg. The obtained results for bimorph before and after laser micromachining are shown in fig 6.15. The Martensite to Austenite transformation of the NiTi film during heating cycle were observed for both samples indicated by the peaks. This suggests that the shape memory effect was retained in the film after micromachining [75]. However, the Austenite start temperature has reduced from 20 °C to 3.0 °C which can be attributed to the annealing happened during the micromachining. The Austenite finish temperature remains nearly the same. Furthermore, the transformation from full Austenite back to Martensite was not observed in the cooling cycles in both the samples.

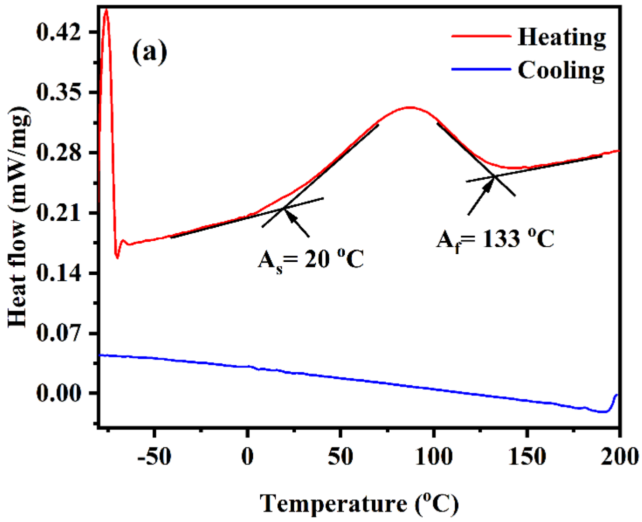

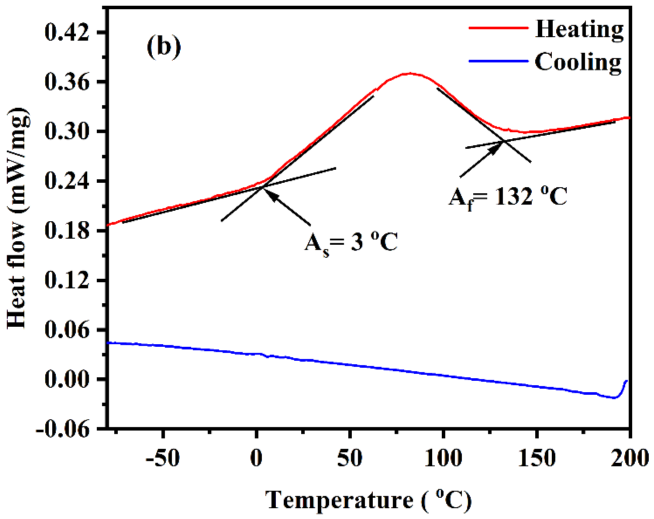

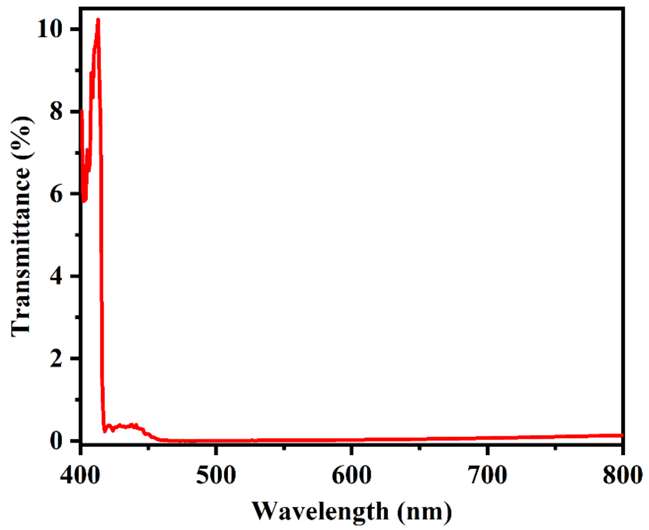

Fig 6.15: Phase transformation analysis of **(a)** NiTi SMA bimorph after deposition **(b)** Laser micromachined actuator **(c)** Transmittance of the incident beam through the optical shutter in a closed configuration.

The transmittance of the optical shutter was determined by UV-visible spectroscopy. The study was performed for a wavelength range of 400 nm to 800 nm to encompass the visible spectrum. The optical shutter in the closed condition should not allow any light to pass through. The UV-visible spectroscopy was aimed to determine the working wavelength range of the optical shutter. The same is shown in Fig 6.15 (c), where the NiTi SMA bimorph-based shutter has shown no transmittance in the 450 nm to 700 nm wavelength range. Wavelength below 450 nm can penetrate the bimorph structure in low percentages. Thus, the fabricated optical shutter can be used to partially transmit a violet light beam.

However, it is helpful as an optical shutter for all other visible wavelengths.

6.4 Summary

The study aims at micromachining the NiTi SMA bimorph using a 1064 nm fiber laser.

Micromachining was studied to generate a single-through cut line for minimal kerf width and heat-affected zones.

- The micromachining parameters were optimized using the design of experiments for which the Full factorial model was employed. The optimal micromachining parameter was 5 W laser power, 5 mm/s laser speed, and 50 µm spot size.
- At laser power below 10 W, laser speed has been the most influential factor in minimizing kerf width and heat affect zone.
- The laser speed of 6 mm/s at all the accompanying laser parameters produced microchannels, while the lower speeds were able to generate a through cut.
- Micromachining of various shapes, such as triangles, squares, and circles, was successfully performed using the optimized micromachining parameter. Also, the NiTi SMA bimorph was micromachined for an optical shutter application.
- SEM images of the fabricated actuator at different locations indicate that micromachining with a laser has annealed the film near the edges and produced finer grains than the shutter's center.
- XRD analysis shows the presence of Ti_2Ni and B19'phases in the pellet and bimorph.
- The phase transformation study confirms the retention of shape memory effect in the film even after laser micromachining.
- The % transmittance of the incident light beam was nearly 0 for wavelengths from 450 nm to 800 nm, which suggests that visible light can't penetrate the optical shutter.

Chapter 7

Explains the utilization of NiTi SMA based bimorph for fabrication of Stewart platform assembly and application in laser beam steering.

Realization of NiTi SMA bimorph-based actuators and mirrors in Stewart Platform Assembly for Opto-Mechatronics Application

7.1 Fabrication and Assembly

7.1.1 Fabrication of NiTi SMA bimorph

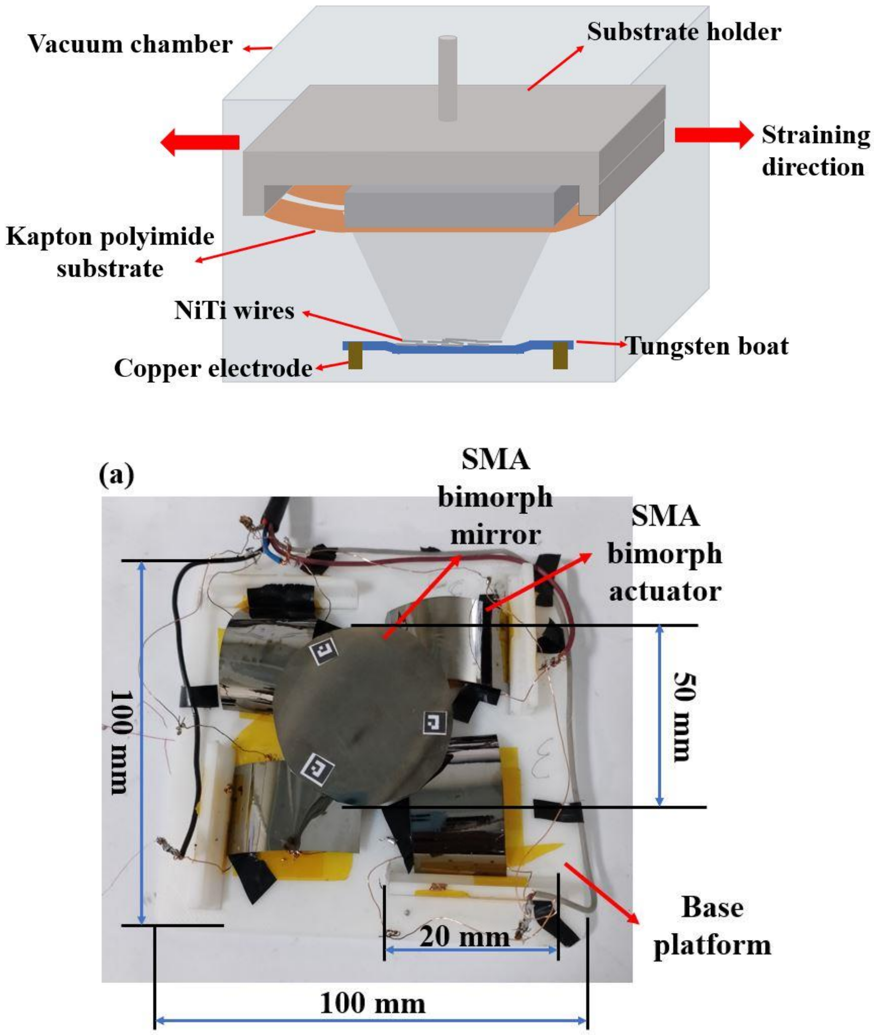

Fig 7.1: (a) NiTi thin film deposition using thermal evaporation technique (b) Fabricated Stewart platform assembly.

NiTi SMA thin film-based bimorph was fabricated using the thermal evaporation technique (Hydro Pneo Vac Technologies)[13][76]. The schematic is shown in figure 2. The Kapton polyimide substrate of size 3 cm x 21 cm, was held in the deposition chamber with the help of a substrate holder. A longitudinal strain of 1 % was applied on the substrate of 75 μm thickness to achieve better actuation[77]. For mirror fabrication, a 200 μm thick Kapton polyimide substrate of size 9 cm x 12 cm was flattened and held in the substrate holder for deposition. A thin NiTi film was deposited by employing the source material in the form of wires, which include NiTi wire (54.2% Ni by weight) and Ti wire of length 4 mm and diameter 1.2 mm. The excess Ti wire has been used in the source material to compensate for the loss of Ti during deposition, which was discussed in our previous work [78]. The adopted source material composition during the deposition was NiTi: Ti=70:30 (by weight). The deposition process was conducted in the chamber at a pressure of 5 x 10^{-5} mbar. The deposition process was conducted at 450 mA for 60 s with a source-to-substrate distance of 100 mm.

7.1.2 ArUco markers-based plane generation

7.1.2.1 ArUco markers

Fig 7.2: ArUco markers utilized for detection of mirror orientation

ArUco markers are kind of fiducial markers which involves images comprising set of distinguishable patterns. They have unique binary codes embedded into the marker pattern in the grid of black and white squares. These markers can be generated in various sizes to be used on plane surfaces. They have been employed for position and orientation detection in autonomous robotic systems like arms, tactile sensors, drones, and AGVs [79–82]. The distance, position, and orientation of the ArUco markers pasted on a surface are usually detected using a camera by image processing. Use of single ArUco marker for pose detection leads to erroneous output. The accuracy of measurement improves with the use of multiple markers. The ArUco markers of size 5 mm x 5 mm generated on a 4 x 4 grid, as shown in Figure 7.2, were used in this study. Since, multiple markers are used, so for clear identification different markers namely ArUco 0, ArUco 1 and ArUco 2 were used. The markers were pasted on the mirror which was tilted for operation with respect to the fixed camera. With this tilting, the detection of ArUco's corner produces noisy and false measurements. Wang et al. have demonstrated that use of additional features (circles) around the ArUco markers improve pose detection accuracy. Similarly, we provided markers with borders to improve the accuracy and stability of corners measurement.

The OpenCV library can access the ArUco marker features for computer vision, machine learning, and image processing[83]. In this study, a live camera feed was used to estimate the real-time position of the markers and orientation of the plane (mirror) under consideration. Python language was utilized with the OpenCV library for this purpose. A Logitech C922 webcam was used to monitor the mirror, and the position and orientation were estimated.

7.1.2.2 Pose Detection Mechanism

The live video stream of the image comprising mirror with three ArUco markers was provided by C920 HD pro webcam developed by Logitech, which provides 30 f/f 1080 p high quality video. The pose detection involves two functions. Firstly, to identify the number of markers present inside the acquired frame. Second function is identifying the marker ID. An adaptive threshold is applied to the frames to obtain the acquire of the markers by dividing the image in to multiple rectangles. The effective borders of the markers and rectangles are identified which reveals the geometry of the candidate marker. Now the validity of the marker was checked by determining their internal codes. The markers image was divided into black and white zones. The borders of the markers were checked to find a matrix of 7 x 7 items with a sub-matrix of 5 x 5 items. The sub-matrix provides the information about the marker ID.

For pose estimation, the camera captures the image containing one or more ArUco markers[84–86]. The image was then processed to detect and extract the markers' pixel coordinates. These coordinates serve as the basis for subsequent calculations. The next step involves the computation of the marker's pose, which refers to its translation (position) and rotation (orientation) in the camera's coordinate system.

The estimation of the pose was achieved through a combination of camera calibration and marker-specific information. This calibration was required to establish a relationship between the image's pixel coordinates and the real-world coordinates. ArUco pose estimation algorithms utilize the known marker size and its corresponding 3D model to calculate the marker's pose. By projecting the 3D model onto the 2D image plane using the camera's intrinsic and extrinsic parameters, the algorithm computes the marker's translation and rotation. This process involves solving the Perspective-n-Point (PnP) problem, which establishes the relationship between the 2D-3D correspondences and the camera's pose.

Three ArUco markers were pasted on the mirror to determine three non-collinear points on the plane of the mirror. These non-collinear points were utilized to generate the equation of the mirror's plane. The approach is mentioned below:

1. Let us assume you have three points on the plane: P_1 (x_1, y_1, z_1), P_2 (x_2, y_2, z_2), and P_3 (x_3, y_3, z_3).
2. Compute two vectors that lie in the plane by subtracting the coordinates of one point from the other two points:

    - Vector $v_1 = P_2 - P_1 = (x_2 - x_1, y_2 - y_1, z_2 - z_1)$
    - Vector $v_2 = P_3 - P_1 = (x_3 - x_1, y_3 - y_1, z_3 - z_1)$

The camera detects the position and inclination of the markers with respect to the initial positions and displays the updated coordinates and inclination.

3. Compute the cross product of the two vectors to obtain a normal vector to the plane:

$$\text{Normal vector } N = v_1 \times v_2$$

The equation of the plane can be expressed in the form $Ax + By + Cz + D = 0$, where (A, B, C) is the normal vector and D is a constant. To find the constant D, substitute the coordinates of one of the points (e.g., P_1) into the equation:

$$A * x_1 + B * y_1 + C * z_1 + D = 0$$

So, the equation of the plane can be determined using the normal vector and one of the points on the plane. The equation involves the normal vector in normalized form, i.e., its magnitude is considered as 1, to simplify the equation.

7.1.2.3 Stewart Platform arrangement integrated with ArUco markers

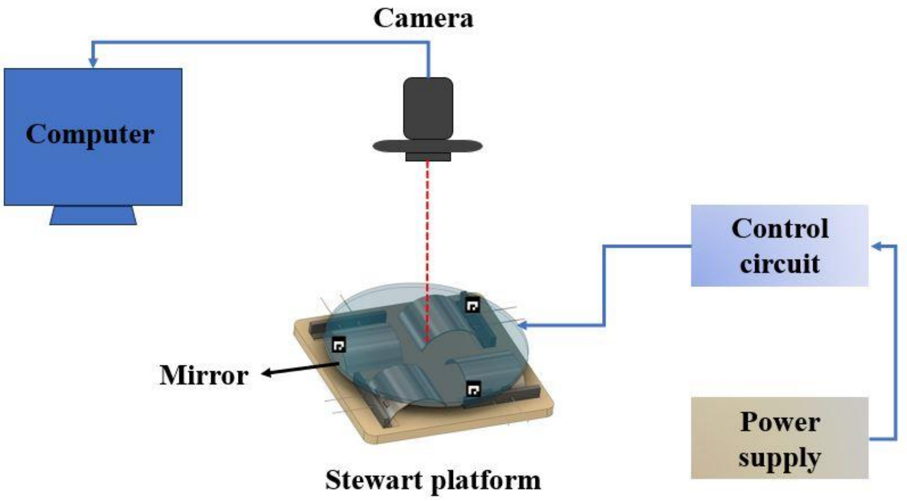

Fig 7.3: Experimental Setup with camera and control unit to determine the mirror tilt

A Stewart platform arrangement was fabricated for mirror tilting and laser beam steering, as shown in Figure 7.1 (b). Four NiTi SMA bimorph actuators of size 40 mm x 15 mm were placed at symmetric positions from the respective proper vertices on a 3d printed platform of size 100 mm x 100 mm. The bimorph actuators were fixed on the platform in slots of size 20 mm x 2 mm. The bimorphs were actuated with the help of Joule heating. The bimorph actuators were connected to the electrical power supply using copper wires. The sequence and the heating time were manipulated using a control circuit, which was driven through Arduino programming. As the bimorph actuators were lightweight and could not support the silicon wafer as a mirror, SMA bimorph was used as a mirror. The heat was supplied to a single as well as two adjacent actuators to study the mirror motion and consequent laser displacement. The bimorph was curved in a normal position and straightened up upon the heating. The 4 of these bimorphs are placed in a specific arrangement to provide motion to the mirror platform placed above them. On heating and straightening up, the bimorph's tip moves down, and the free end moves from its normal position.

The Stewart platform assembly was placed in an acrylic box on which a camera was placed to measure the angular displacement of the mirror. The camera was positioned 8.5 cm above the mirror surface. The camera was operated using computer vision, which calculates the position of the mirror by detecting the positions of the three ArUco markers pasted on the mirror surface, as shown in Figure 7.3. The use of ArUco markers for position and angle detection is discussed in section 7.1.2.1. Using these points, the equation of the plane in real-time and the equation of normal leading to the plane's inclination values with respect to the x, y, and z axes can be determined.

The unactuated position of the mirror is horizontal plane comprising the reference x and y axes. Vertical axis was considered to be the reference z-axis. The angles of ArUco markers with respect to the reference axes in this position. After actuation of the leg, the mirror tilts and the angles and position of markers change which were monitored with live camera feed as shown in fig 7.3. The instantaneous positions of all three markers with respect to reference axes were measured and displayed on the Open CV interface. These positions were utilized to determine the inclination of the mirror with respect to its initial horizontal position.

7.2 Calibration for Pose Detection

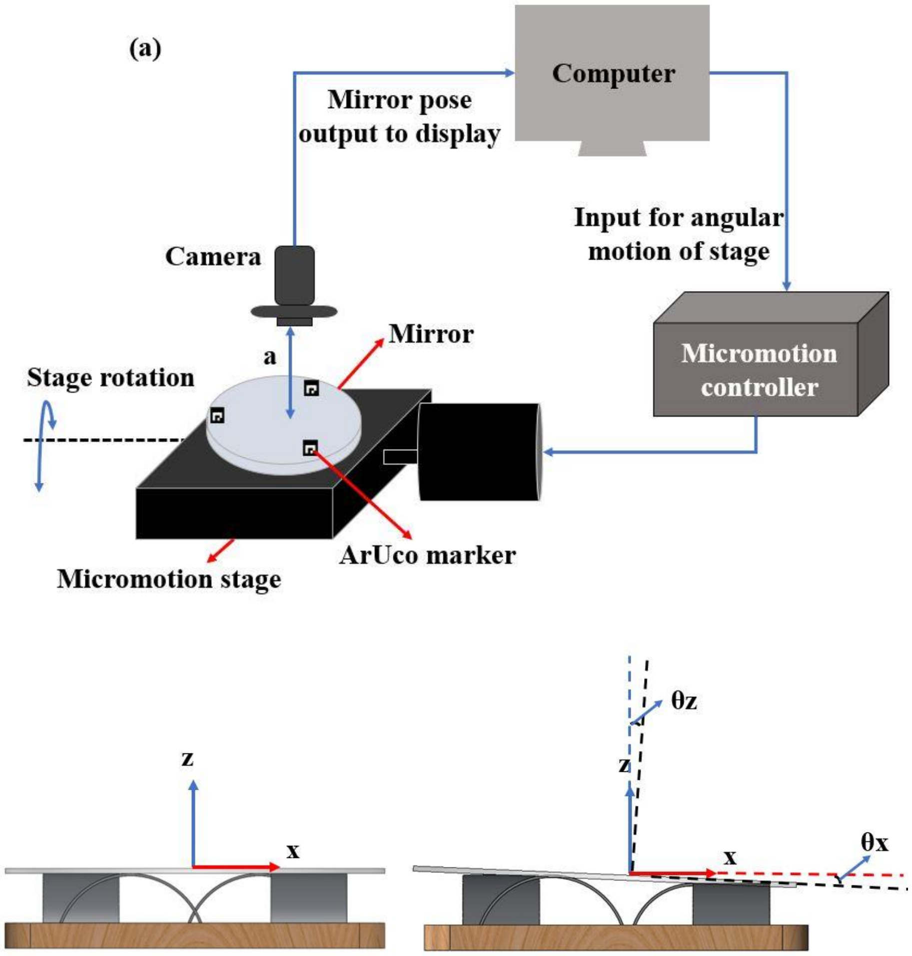

Figure 7.4: (a) Setup for camera calibration **(b)** Side view of angular motion of the mirror.

The camera setup and the ArUco-based positioning and detection system were calibrated to measure the plane's angles. The calibration of the camera for pose detection was performed with the setup shown in fig 7.4 (a). The mirror was placed on a rotating micromotion stage which was driven by a micromotion controller for setting the mirror at a specific angle. The camera was placed on top of the mirror at a distance of a=8.5 cm, which is same as in the Stewart platform setup. The mirror was tilted about both the axes of horizontal plane individually and pose detection of ArUco markers were done. The motion of any one of the actuators in forward direction due to Joule heating tilts the mirror as shown in figure 7.4 (b). The inclination about x-axis or y-axis also results in change in orientation of the mirror about z-axis. Thus, the calibration for orientation detection of the mirror was done for all the axes simultaneously with the said setup.

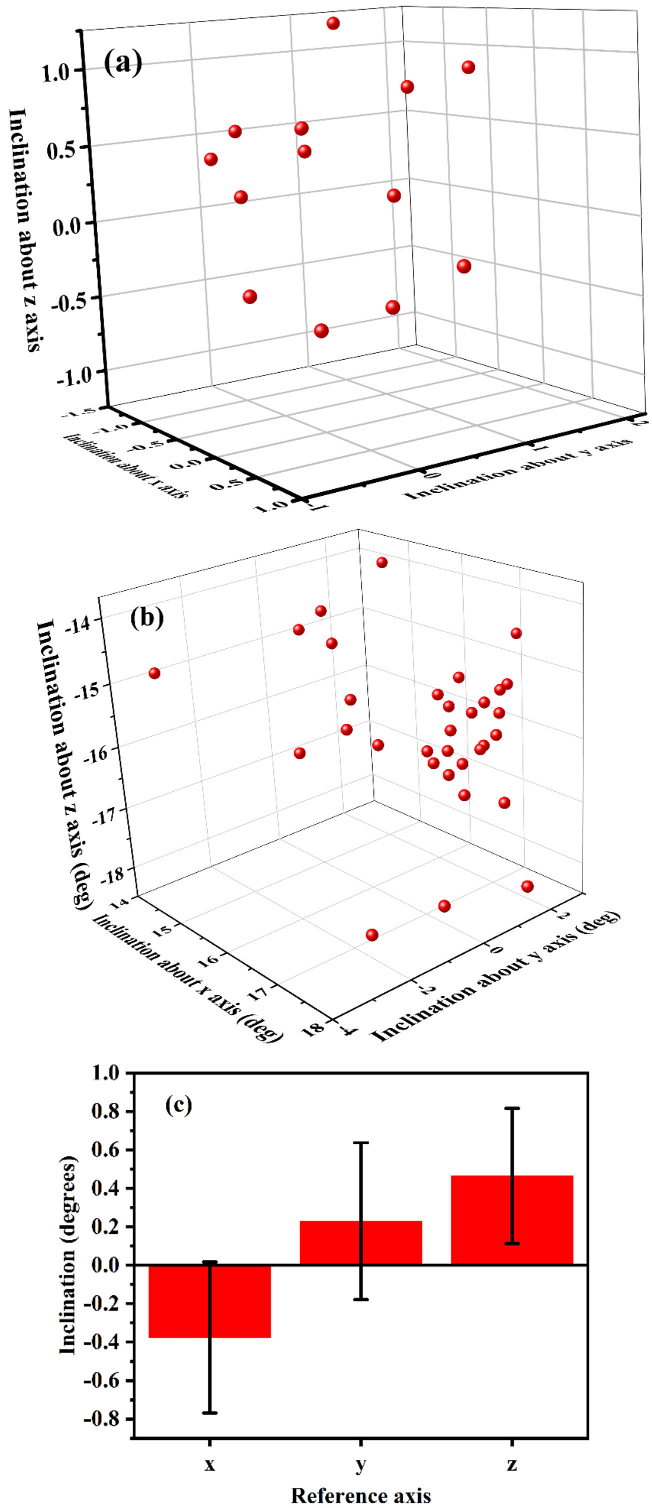

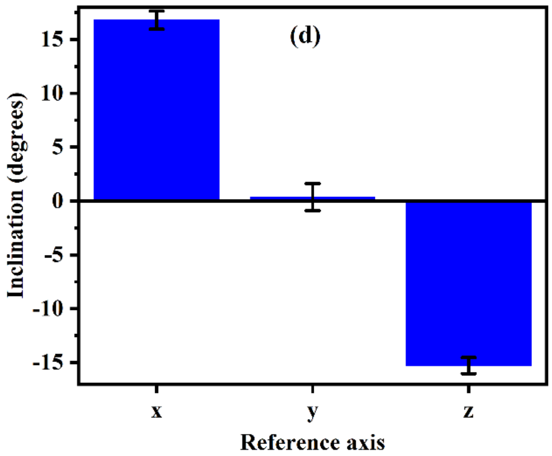

Figure 7.5: The measured angular tilt of the reference plane detected with the ArUco markers for **(a)** horizontal position of the mirror (0°) and **(b)** 16° tilt about x-axis.

The calibration was achieved by detecting the plane's angle tilted at the measured angles of 0° and 16° with respect to the horizontal plane. Figure 6 displays the angles of the plane for six iterations. The inclination of the plane was measured from the top, which produces the angle after conversion through code in the negative direction. Thus, the measured value of 10° angle of the reference plane was -10.28° ±0.26° and of 15° was -15.6°±0.6°. The camera was placed in a slot cut in the acrylic box. A slight misalignment can lead to erroneous readings. Secondly, the feed of the camera for the inclination of the ArUco can vary due to the inclination of the markers. This can also produce errors; thus, higher inclination values were difficult to detect with the current setup. Both camera placement and marker inclination should be proper before considering the input values.

7.3 Motion Detection of Mirror

7.3.1 Mirror Inclination with Single Bimorph Actuation

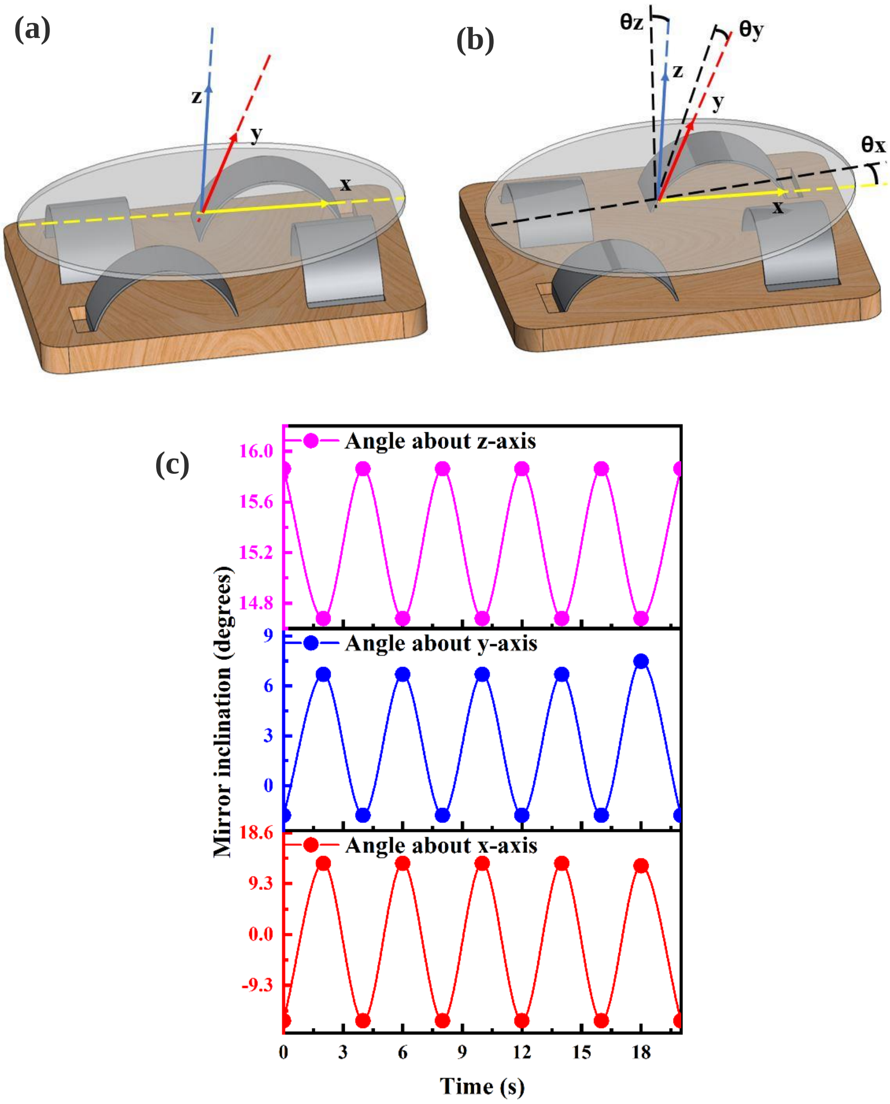

Figure 7.6: Schematic of Stewart platform **(a)** without mirror inclination and **(b)** mirror inclined with single bimorph actuation. **(c)** Mirror inclination with single bimorph actuation for 8 V input at 0.25 Hz cycle.

This section reveals the results obtained for the inclination of the mirror involving a Shape Memory Alloy (SMA) NiTi-based Stewart platform. The initial position of the mirror was horizontal and center of the mirror was considered to be the origin (0, 0, 0). The electrical power was supplied by an external power source, and the frequency of the supply was controlled using a relay and an Arduino. The bimorph has shown the actuation at 8 V supply and has drawn a current of up to 0.12 A for a 0.25 Hz cycle. Only one bimorph was actuated, and the other three were stationary, resulting in the mirror tilting at the top. This tilting was captured using the ArUco and computer vision techniques explained in section 2. Figure 7.6 (b) illustrates the change in orientation of the of the mirror with respect to original position in figure 7.6 (a), when one bimorph leg was actuated. For 0.25 Hz actuation frequency, the mirror tilted about 28.76° about the x-axis, 8.46° about the y-axis, and 1.19° about the z-axis. As mentioned in previous section, when mirror was tilted about the x-axis it results in the inclination of the mirror about other axes as well. The mirror inclination was set about x-axis and resultant inclination was observed about y and z axes but the amplitude was low. The actual angles of inclination about both the x and y axes have values ranging from negative to positive inclination, as shown in Figure 7.6 (c).

7.3.2 Mirror Inclination with Two adjacent Bimorph Actuation

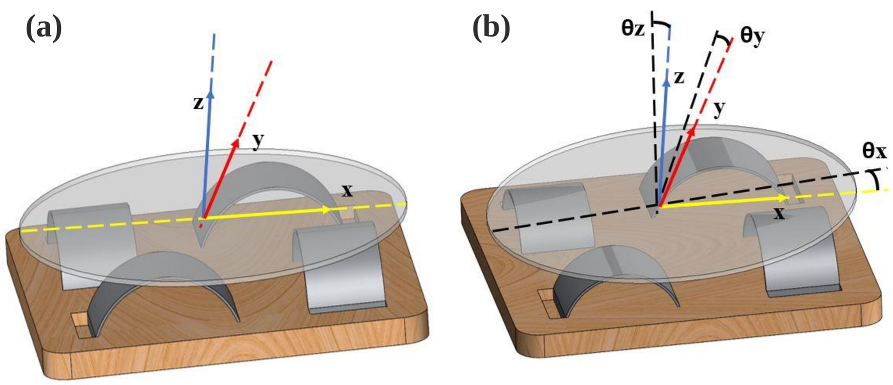

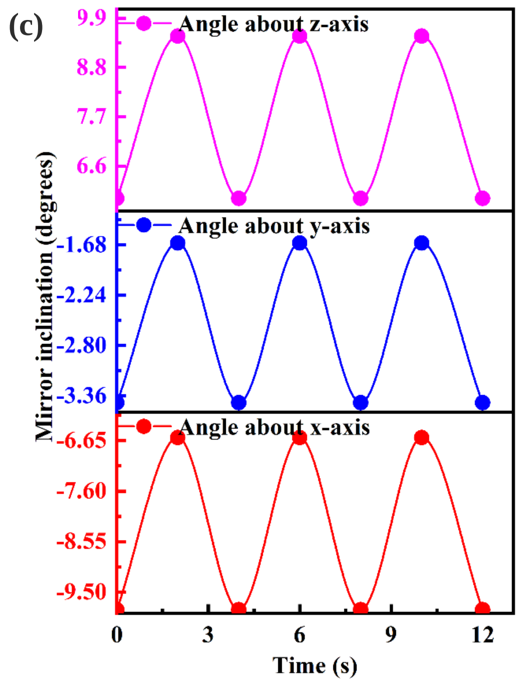

Figure 7.7: Schematic of Stewart platform **(a)** without mirror inclination and **(b)** mirror inclined with two adjacent bimorph actuations. **(c)** Mirror inclination with two adjacent bimorph actuations for 8V input at 0.25 Hz cycle.

The orientation analysis of the mirror was also studied for the actuation of two bimorph legs simultaneously. Both the legs utilized for actuation were adjacent to each other. The supply voltage was 8 V with a current of 0.12 A at an actuation frequency of 0.25 Hz. Fig 7.7 (b) illustrates the change in orientation of the of the mirror with respect to original position in figure 7.7 (a), when two adjacent bimorph legs were actuated simultaneously. The maximum mirror inclination captured by the computer vision was 3.24° about the x-axis, 1.78° about the y-axis and 3.62° about the z-axis which is shown in figure 7.7 (c). During the initial cycle, where the bimorph was at room temperature, a notable deviation was observed upon heating. This deviation can be attributed to the phase transformation of the SMA NiTi material. After the first heating cycle, an intriguing phenomenon was observed: the temperature of the bimorph upon cooling did not return to the exact room temperature. The frequency of actuation (0.25 Hz) didn't allow enough time for cooling. As a result, after few heating and cooling cycles, the bimorph leg exhibited reduced displacement and presented a consistent but slightly deviated trajectory. This behavior suggests the existence of residual stress or incomplete phase transition during the cooling phase, contributing to the observed deviations. Furthermore, as the inclination of the mirror was continuously monitored by a computer vision-integrated camera, the input power can be altered manually to achieve the desired mirror inclination.

7.3.3 Numerical Simulation of Stewart Platform Assembly

The actuator legs were in a cantilever configuration in the Stewart platform assembly and were the primary actuators. However, their motion was not directly captured due to the mirror being on top, and thus, simulation was used to produce an estimated path of the movement of the legs. The kinematic analysis of the Stewart platform arrangement was performed using MATLAB 2023b Simulink software. The bimorph legs have curved profile that straightens on actuation. The motion was reproduced in Simulink using rigid links. The bimorph leg was considered a robotic arm comprising two links, as shown in Figure 7.8 (a). The length of each link was 2 mm, as the bimorph leg utilized in the Stewart platform arrangement was 4 mm in length. Both the movable links were connected via a reactive joint, and the movable link 1 was connected to the base frame through another reactive joint. Figure 7.8 (b) illustrates the subsystem corresponding to the bimorph leg formed in the Simulink. Four such legs were positioned appropriately, and a mirror was placed at the top to form the Stewart platform arrangement. The mirror was attached with link 2 with a sliding pair, which tilts the mirror according to the movement of the leg. The assumptions made to facilitate the study are listed below:

1. The motion will be achieved at the joints only.
2. Links are rigid and have constant shapes and dimensions throughout the study.

3. Material considerations were not included.
4. The free end of link 2 was assumed to be attached to the mirror. Thus, the motion of the free end of link 2 was only measured using Simulink.

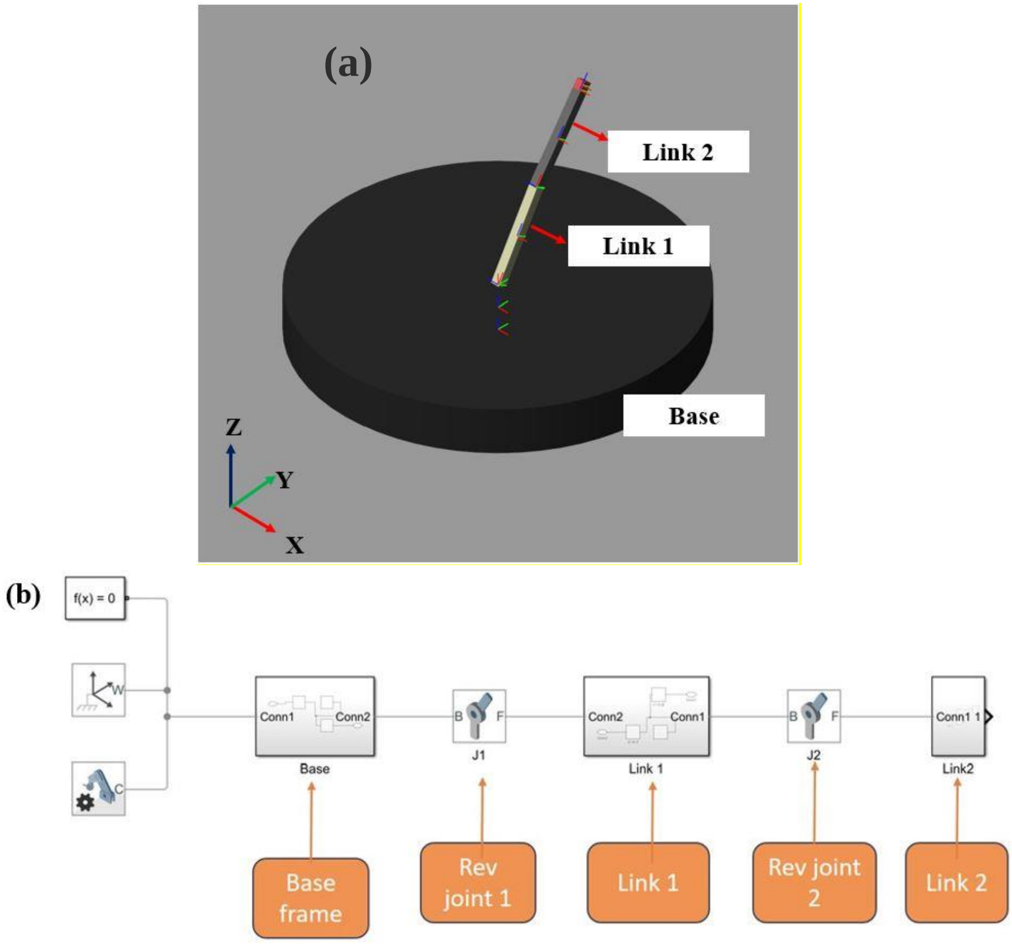

Figure 7.8: (a) Single bimorph leg simulated as a combination of two links (b) Simulink subsystem corresponding to bimorph leg.

The angle of the links (θ_1 and θ_2) with the respective frames were the inputs for the analysis. By applying forward kinematic analysis, the position of the end effector was determined with respect to the universal frame. The position and orientation of the end effector, i.e., mirror, was derived by the transformation of the end effector (mirror) with respect to the fixed frame. Figure 7.9 (a) depicts the Simulink circuit applied to transform the input signals into a graphical representation of the motion of the bimorph. The initial step involved defining the robot, specifying the angles, and establishing movement parameters corresponding to the two angles of the robot's links. Subsequently, a homogeneous transform was applied to ascertain the configuration of the end effector located at the tip of the bimorph robot. To represent the points in the 3D plane derived from the transformation matrix, coordinate transformation conversion was executed, resulting in a vector that encapsulates the positional information of the end effector.

The sinusoidal motion was fed to the circuit with a constant initial displacement of 0.044 mm in the x-direction. The sinusoidal input was provided with a frequency of 0.25 Hz. The position of the end effector was calculated in cartesian coordinates. As the movement of the end effector started, its value dropped to 0.02 mm in the x direction as a result of motion in the y and z directions. The motion in the y and z directions was in the same phase, which is in the opposite phase to that of the x direction, as shown in Figure 7.9 (b). The similar behavior is shown in the experimental results. As the mirror inclination increases about the two axes, its inclination about the third axis reduces. The Simulink results show that angular displacement in the y direction has a range of 0.1 mm and in the z direction has a range of about 0.2 mm.

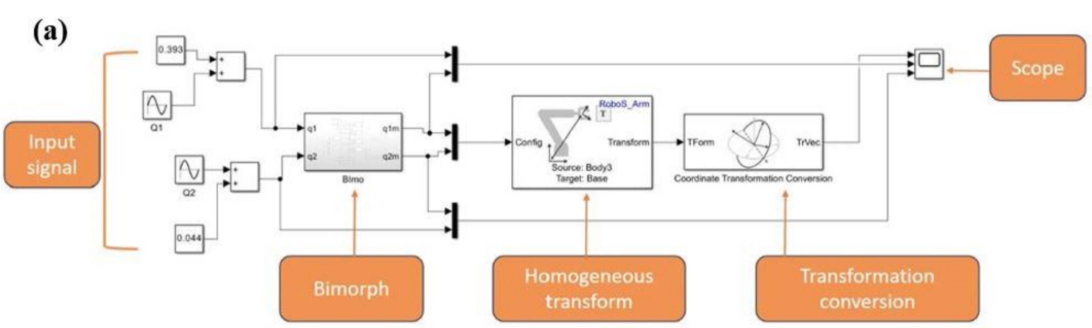

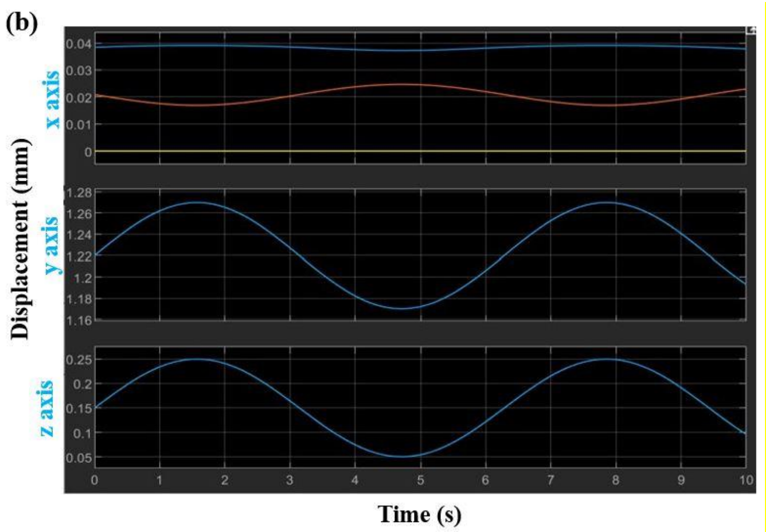

Figure 7.9: (a) Simulink circuit for the transformation of the input signal in the sinusoidal form to a graphical output of the end effector (b) Graphical output of the displacement of the end effector.

7.4 Laser Beam Steering

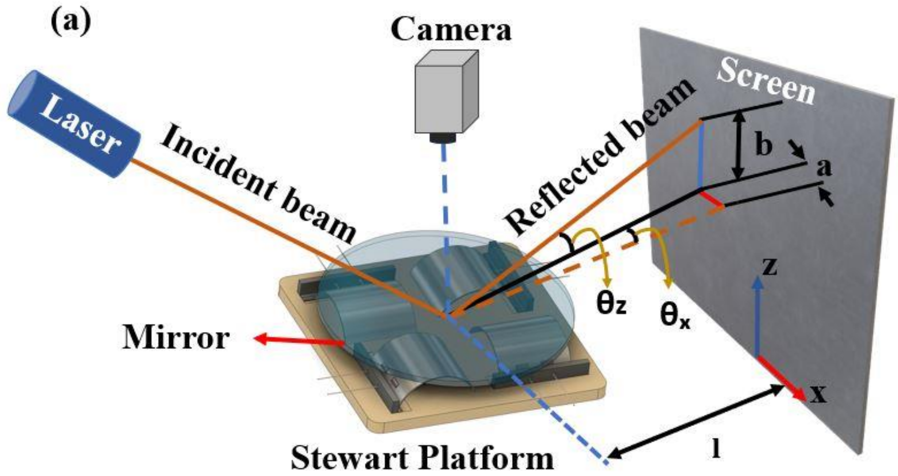

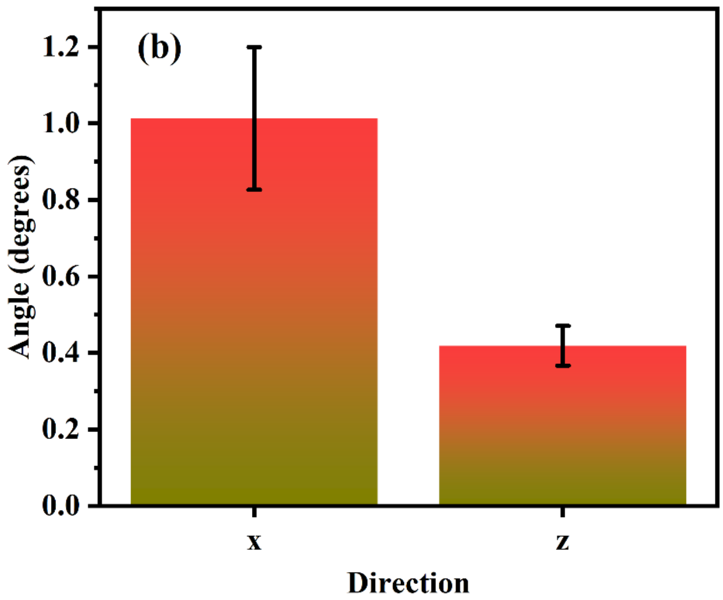

Figure 7.10: (a) Schematic of setup for laser beam steering with SMA integrted Stewart platform arrangement **(b)** Measured laser beam displacement on the screen.

Figure 7.8 (a) illustrates the setup for investigating the laser beam steering achieved by tilting the mirror through external heating of the bimorph leg. A red diode laser (Holmarc DL-R-3) of 650 nm wavelength and 3 mW optical power was utilized as an input laser source for the setup. The distance between the center of the mirror and the screen was 300 mm. The laser beam was incident on the mirror of the Stewart platform arrangement. As the inclination of the mirror changes, the position of the reflected beam obtained on the screen changes. The initial reflected laser beam is depicted by solid line in fig 7.8 (a) and the reflected laser beam after the inclination of the mirror is indicated by the dotted line. The screen position was fixed in the y direction; thus, the laser beam position changed in the x and z directions only.

The position of the reflected laser beam was measured thrice, and the results are shown in Figure 7.8 (b). The initial position of the laser beam on the screen was marked as the origin, i.e. (0,0). After the mirror motion, the beam position changed in the x direction by 5.3±0.976 mm and in the z direction by 2.19±0.27 mm. This measured beam displacement was with respect to the set distance of 300 mm between the center of the mirror and screen, and will vary with the distance l. The more standardized and reliable result has to be in form of angular motion of the beam. The linear displacement of the beam on the screen was converted to angular displacement by applying the formula mentioned below:

$$\theta_x = tan^{-1}(\frac{a}{l}) \text{ and } \theta_z = tan^{-1}(\frac{b}{l})$$

Where, θ_x and θ_z are the angular displacements in x-direction and z-direction respectively (in degrees), a and b are linear beam displacements on the screen an x and z directions respectively and l is the distance between the center of the mirror and screen (mm). The angle moved in x-direction was 1.01±0.18° and in z-direction was 0.42±0.05°. Despite achieving stability in the reflected laser beam's position, a minor shift in the initial position was observed after each cycle. This shift is attributed to residual stresses or non-reversible phase changes that accumulate over repeated cycles. The fabricated Stewart platform arrangement demonstrates the capability to steer the laser beam with a low power input to the legs. Also, the beam can be reflected to a desired location by manipulating the input power, which can be used for scanning and communication purposes.

7.5 Summary

- NiTi/Kapton polyimide bimorph was fabricated using a thermal evaporation technique.
- The bimorph of size 4 cm x 2 cm was employed as the actuator leg of the Stewart platform arrangement. The Stewart platform was assembled on a 3D-printed platform with a bimorph mirror placed atop four bimorph legs.
- The inclination of the mirror as a result of the actuation of a single bimorph and two bimorphs simultaneously was captured, locating the positions of three ArUco markers pasted on the mirror.

- The maximum inclination of the mirror achieved was 28.76° about the x-axis, 8.46° about the y-axis, and 1.19° about the z-axis at 8V supply for single bimorph actuation.
- The maximum inclination of the mirror achieved was 3.24° about the x-axis, 1.78° about the y-axis and 3.62° about the z-axis at 8V supply for actuation of two adjacent bimorph legs.
- Finally, the incident laser beam was steered by an angle of 1.01°±0.18° in x-direction and 0.42°±0.05° in z-direction.

Chapter 8

This chapter explains the effect of pre-straining of Kapton polyimide substrate on the properties of NiTi/Kapton polyimide thin film structure as a self-actuating mirror.

Conclusion and Future Scope

8.1 Conclusions

In this work, NiTi thin film bimorph-based flexible micromirrors and microactuators were fabricated using different manufacturing techniques. Flexible micromirrors were fabricated with E-beam evaporation technique with a focus on studying the influence of substrate and heating on the performance of the flexible micromirror. Actuators were fabricated with both E-beam and thermal evaporation techniques. The substrate-to-film adhesion and actuation of the actuators were improved by employing laser annealing of the Kapton polyimide substrate and the effects of different laser annealing parameters of Nd: YAG laser were investigated. Laser energy was also utilized for micromachining of the bimorph structure to fabricate actuators of customized shapes. Finally, the NiTi/Kapton polyimide bimorph-based mirrors and actuators were assembled in a Stewart platform arrangement. The arrangement proved to be useful for applications involving optical beam deflection.

- The performance of electrically actuated NiTi/polyimide bimorph structures fabricated under varying substrate pre-strain and temperatures was evaluated in a cantilever configuration. Experimental results demonstrated a maximum tip displacement of 75 μm for a 1% pre-strained bimorph, actuated at 25 V and 0.25 A with a driving frequency of 0.25 Hz. However, simulated tip displacements consistently exceeded the experimental values, indicating idealized assumptions in the modelling framework. Notably, bimorphs with 3% pre-strain exhibited no measurable displacement experimentally due to film discontinuity, attributed to delamination or cracking induced by excessive substrate strain recovery. Surface morphology, examined via SEM, revealed a smooth surface in unstrained samples, while pre-strained bimorphs developed strain-induced marks. Increased pre-strain was found to damage the NiTi film post-deposition.

- The variation in nickel concentration notably influenced the transformation temperatures of the SMA film. Specifically, the austenite finish temperature (Af) was observed to increase with increasing Ni content, corroborating earlier findings in SMA literature regarding compositional tuning of transformation behavior. Furthermore, exhibited excellent optical performance, with up to 98.3% reflectance in the visible spectrum for unstrained and 1% pre-strained bimorphs, highlighting their potential utility as flexible micromirrors. Additionally, substrate heating during deposition significantly influenced film morphology. Films deposited at a substrate temperature of 150 °C exhibited denser microstructures and displayed improved hydrophobic surface characteristics.

- In third section of the study, laser annealing of the Kapton polyimide substrate was performed with a 355 nm Nd: YAG laser prior to the deposition to improve substrate-to-film adhesion and actuation characteristics. Laser fluences up to 1200 mJ/cm² induced surface crystallization, while at 1630 mJ/cm² and 50% laser overlap (LO), crystalline peaks disappeared, indicating top layer removal. Crystallinity reappeared at 70% LO. Increased fluence and LO led to surface molecular loss, as shown by rising transmittance. Contact angle measurements dropped significantly for annealed samples, indicating improved wettability. The best film adhesion was achieved on polyimide treated at 1630 mJ/cm² and 70% LO, confirmed by the Scotch tape test. Electrical actuation results showed a notable increase in tip displacement—from 0.1 mm on pristine polyimide to 1.6 mm on laser-annealed polyimide at 1630 mJ/cm² and 70%

LO. While external loading generally reduced displacement, the bimorph on 1630 mJ/cm² and 50% LO remained unaffected.

- Laser assisted micromachining was of the bimorph structure was investigated with a 1064 nm fiber laser, to achieve customized microactuators. Micromachining parameters were optimized using a full factorial design of experiments, identifying 5 W laser power, 5 mm/s speed, and 50 µm spot size as optimal. At powers below 10 W, laser speed significantly influenced kerf width and heat-affected zone. Microchannels formed at 6 mm/s, while lower speeds enabled through cuts. NiTi SMA bimorphs were successfully micromachined to generate actuators of different geometries. SEM analysis showed edge annealing and finer grains near micromachined regions. XRD confirmed Ti_2Ni and B19′ phases, while phase transformation studies validated the preservation of the shape memory effect post-machining. Optical transmittance tests revealed near-zero transmission from 450–800 nm, indicating effective light blocking, ideal for optical shutter functionality. Finally, an optical shutter was fabricated with laser-assisted micromachining capable of opening and closing with electrical power.
- A NiTi/Kapton polyimide bimorph actuator was fabricated via thermal evaporation and used as a 4 cm × 2 cm leg in a Stewart platform assembled on a 3D-printed base. A bimorph mirror atop four actuator legs enabled multi-axis motion. Actuation-induced mirror inclination was tracked using ArUco markers. Maximum tilt for single bimorph actuation reached 28.76°, 8.46°, and 1.19° at 8 V in x, y and z directions respectively. For dual adjacent bimorph actuation, maximum tilts were 3.24°, 1.78°, and 3.62° in x, y and z directions respectively. Laser beam steering was achieved with deflections of $1.01° \pm 0.18°$ in the x-direction and $0.42° \pm 0.05°$ in the z-direction, demonstrating the system's effectiveness for precision optical manipulation.

8.2 Challenges and Future Scope

- Experimental studies on NiTi-based SMA thin films faced challenges due to their sensitivity to processing conditions, particularly in controlling film composition. Titanium loss during deposition led to excessively Ni-rich films (>70% Ni), drastically shifting transformation temperatures and hindering actuation. To address this, excess Ti was added during deposition and pellet preparation, improving composition control. However, achieving near-equiatomic NiTi remains an area for further optimization to enhance actuator performance and reliability.
- For long term operation and stability of the devices developed as a part of the study, the hysteresis effects and fatigue life of the NiTi/Kapton polyimide bimorph-based actuators need to be thoroughly investigated in future. Also, the phase transformation in the NiTi thin film during heating and cooling changes its refractive index. This change may affect the reflectivity of the flexible mirror at high temperatures. Thus, temperature dependent reflectivity of the flexible mirror can be tested in future to narrow down the applicability window of the mirror.
- Laser micromachining offers a precise method for fabricating actuator assemblies such as microgrippers and micropumps, enabling the development of complex thin film based micro-scale devices. It is particularly effective in structuring bimorph thin-film actuators for applications like microheaters and micropumps, where fine geometrical features are essential for efficient performance. Furthermore, the optical shutters developed through this technique can be further tested and adapted for practical use in real-life shutter applications, particularly in miniaturized optical systems and opto-mechatronic devices.
- The Stewart platform assembly can be significantly enhanced by integrating a closed-loop feedback control system to regulate the

power supplied to the bimorph actuators based on the desired mirror inclination, ensuring precise and responsive actuation. Additionally, the current numerical simulation model can be further refined to more accurately predict real-time mirror tilt under varying actuation conditions, improving the system's predictive and adaptive capabilities. Future work may also focus on the miniaturization of the Stewart platform to achieve finer control, reduce actuation power requirements, and broaden its applicability in compact opto-mechatronic systems.

References

1. Kim DH, Park YC, Park S. Design and fabrication of twisting-type thermal actuation mechanism for micromirrors. Sens Actuators A Phys. 2010 Apr;159(1):79–87.

2. Mu X, Sun W, Feng H, Yu A, Chen KWS, Fu CY, Olivo M. MEMS micromirror integrated endoscopic probe for optical coherence tomography bioimaging. Sens Actuators A Phys. 2011 Jul;168(1):202–12.

3. Xie H, Pan Y, Fedder GK. Endoscopic optical coherence tomographic imaging with a CMOS-MEMS micromirror. 2003.

4. Pengwang E, Rabenorosoa K, Rakotondrabe M, Andreff N. Scanning micromirror platform based on MEMS technology for medical application. Vol. 7, Micromachines. MDPI AG; 2016.

5. Izhar U, Izhar AB, Tatic-Lucic S. A multi-axis electrothermal micromirror for a miniaturized OCT system. Sens Actuators A Phys. 2011 Jun;167(2):152–61.

6. Narayane D, Taiwade R V., Sahu K. Review on development and performance of shape memory alloy/polyimide thin-film composites. Vol. 38, Materials and Manufacturing Processes. Taylor and Francis Ltd.; 2023. p. 245–59.

7. Samal S, Sulovský M, Kopeček J, Šittner P. Deposition and characterization of plasma sprayed NiTi powder on stainless steel and graphite substrate. Mater Chem Phys. 2023 Oct 1;307.

8. He JL, Won KW, Chang CT, Chen KC, Lin HC. Cavitation-resistant TiNi films deposited by using cathodic arc plasma ion plating [Internet]. Wear. Available from: www.elsevier.comrlocaterwear

9. Yang LM, Tieu AK, Dunne DP, Huang SW, Li HJ, Wexler D, Jiang ZY. Cavitation erosion resistance of NiTi thin films

produced by Filtered Arc Deposition. Wear. 2009 Jun 15;267(1–4):233–43.

10. Gu HD, Leung KM, Chung CY, You L, Han XD, Chan KS, Lai JKL. Pulsed laser deposition of NiTi shape memory alloy thin films with optimum parameters. Vol. 330, Thin Solid Films. ELSEVIER; 1998.

11. Hou H, Hamilton RF, Horn MW, Jin Y. NiTi thin films prepared by biased target ion beam deposition co-sputtering from elemental Ni and Ti targets. Thin Solid Films. 2014 Nov 3;570(PartA):1–6.

12. Jayachandran S, Mani Prabu SS, Manikandan M, Muralidharan M, Harivishanth M, Akash K, Palani IA. Exploring the functional capabilities of NiTi shape memory alloy thin films deposited using electron beam evaporation technique. Vacuum. 2019 Oct 1;168.

13. Jayachandran S, Akash K, Mani Prabu SS, Manikandan M, Muralidharan M, Brolin A, Palani IA. Investigations on performance viability of NiTi, NiTiCu, CuAlNi and CuAlNiMn shape memory alloy/Kapton composite thin film for actuator application. Compos B Eng. 2019 Nov 1;176.

14. Mineta T, Kasai K, Sasaki Y, Makino E, Kawashima T, Shibata T. Flash-evaporated TiNiCu thick film for shape memory alloy micro actuator. Microelectron Eng. 2009 Apr;86(4–6):1274–7.

15. Makino E, Mitsuya T, Shibata T. Fabrication of TiNi shape memory micropump.

16. Subbian J, Raikwar S, Sindam NK, Madhav MT, Anand PI. Design and Development of NiTi Shape Memory Alloy Belt for Waste Heat Energy Recovery System. J Mater Eng Perform. 2021 Dec 1;30(12):9048–58.

17. Karna P, Prabu SSM, Karthikeyan SC, Mithun R, Jayachandran S, Resnina N, Belyaev S, Palani IA. Investigations on laser actuation and life cycle characteristics of NiTi shape memory alloy bimorph for non-contact functional applications. Sens Actuators A Phys. 2021 Apr 15;321.

18. Adams TM, Kirkpatrick SR, Wang Z, Siahmakoun A. NiTi shape memory alloy thin films deposited by co-evaporation. Mater Lett. 2005 Apr;59(10):1161–4.

19. Zainal MA, Sahlan S, Mohamed Ali MS. Micromachined shape-memory-alloy microactuators and their application in biomedical devices. Vol. 6, Micromachines. MDPI AG; 2015. p. 879–901.

20. Mehrpouya M, Bidsorkhi HC. MEMS Applications of NiTi Based Shape Memory Alloys: A Review. Micro and Nanosystems. 2017 Jun 22;8(2):79–91.

21. Narayane D, Taiwade R V. Tailoring the actuation characteristics of Ni-Ti shape memory alloy/polyimide thin film composites. Composites Communications. 2025 Jan 1;53:102220.

22. Fu YQ, Luo JK, Flewitt AJ, Huang WM, Zhang S, Du HJ, Milne WI. Thin film shape memory alloys and microactuators. Vol. 2, Int. J. Computational Materials Science and Surface Engineering. 2009.

23. Liu H, Tang Y, Xie Y, Lu L, Wan Z, Tang W, Yang L, Yang D. Effect of pulsed Nd:YAG laser processing parameters on surface properties of polyimide films. Surf Coat Technol. 2019 Mar 15;361:102–11.

24. Nam KH, Abdulhafez M, Najaf Tomaraei G, Bedewy M. Laser-Induced fluorinated graphene for superhydrophobic surfaces

with anisotropic wetting and switchable adhesion. Appl Surf Sci. 2022 Feb 1;574.

25. Hiraoka H, Lazare S. Surface modifications of Kapton and cured polyimide films by ArF excimer laser: applications to imagewise wetting and metallization. Vol. 46, Applied Surface Science.

26. Balp '~ Z, Feurer T, Callahan DL, Sauerbrey R. Thermal and mechanical coupling between successive pulses in KrF-excimer-laser ablation of polyimide. Vol. 62, Appl. Phys. A. 1996.

27. Bolle M, Lazare S. applied surface science Large scale excimer laser production of submicron periodic structures on polymer surfaces. Vol. 69, Applied Surface Science. 1993.

28. Danev G, Spassova E, Assa J, Ihlemann J, Schumacher D. Excimer laser structuring of bulk polyimide material.

29. Inagaki M, Harada ~ Sunao, Sato T, Nakajima T, Horino Y, And $, Morita K. CARBONIZATION OF POLYIMIDE FILM "KAPTON." Vol. 21, Carbon. 1989.

30. Du Q, Ai J, Qin Z, Liu J, Zeng X. Fabrication of superhydrophobic/superhydrophilic patterns on polyimide surface by ultraviolet laser direct texturing. J Mater Process Technol. 2018 Jan 1;251:188–96.

31. Santosh S, Srivatsan S, Vignesh Pandian R. Unravelling the effect of CO2 laser machining parameters on the surface and shape memory characteristics of CuAlFeMn quaternary shape memory alloy. Opt Laser Technol. 2023 Aug 1;163.

32. Pfleging W, Ludwig A, Seemann K, Preu R, Mackel H, Glunz SW. Laser micromachining for applications in thin film technology [Internet]. Vol. 154, Applied Surface Science. 2000. Available from: www.elsevier.nlrlocaterapsusc

33. Daemi B, Ekberg P, Mattsson L. Lateral performance evaluation of laser micromachining by high precision optical metrology and image analysis. Precis Eng. 2017 Oct 1;50:8–19.

34. Jithin MA, Ganapathi KL, Udayashankar NK, Mohan S. Novel fabrication technique for NiTi and TiN micro-structures by femtosecond lasers. In: IOP Conference Series: Materials Science and Engineering. IOP Publishing Ltd; 2020.

35. Liu L, Li DB, Tong YF, Zhu YF. Fiber laser micromachining of thin NiTi tubes for shape memory vascular stents. Appl Phys A Mater Sci Process. 2016 Jul 1;122(7).

36. Panigrahi D, Patel SK. Influence of dry and wet environments during fiber laser processing of metallic substrate under a neoteric scan mode. Opt Laser Technol. 2023 Feb 1;158.

37. Leone C, Genna S, Tagliaferri V. Fibre laser cutting of CFRP thin sheets by multi-passes scan technique. Opt Lasers Eng. 2014;53:43–50.

38. Çelen S. Laser micro-machined semi-slinky like MEMS structures: Novel interface coolers. Opt Laser Technol. 2012 Oct;44(7):2043–8.

39. Chkalov R, Khorkov K, Kochuev D. Femtosecond Laser Micromachining of Metal Thin Films [Internet]. Vol. 11, Materials Today: Proceedings. 2019. Available from: www.sciencedirect.comwww.materialstoday.com/proceedings2214-7853

40. Auricchio F, Saccos E. A ONE-DIMENSIONAL MODEL FOR SUPERELASTIC SHAPE-MEMORY ALLOYS WITH DIFFERENT ELASTIC PROPERTIES BETWEEN AUSTENITE AND MARTENSITE. Vol. 32, lnt. J. Non-Linear Mechanics. 1997.

41. Qidwai MA, Lagoudas DC. Numerical implementation of a shape memory alloy thermomechanical constitutive model using return mapping algorithms. Vol. 47, INTERNATIONAL JOURNAL FOR NUMERICAL METHODS IN ENGINEERING Int. J. Numer. Meth. Engng. 2000.

42. Lagoudas D, Hartl D, Chemisky Y, MacHado L, Popov P. Constitutive model for the numerical analysis of phase transformation in polycrystalline shape memory alloys. Int J Plast. 2012 May;32–33:155–83.

43. Ozturk MM, Bhattacharyya A. A computational study of cyclic thermal response of shape memory alloy thin-film island structures. Acta Mech. 2017 Oct 1;228(10):3497–509.

44. Sun S, Jiang X. Nonlinear analysis of actuation performance of shape memory alloy composite film based on silicon substrate. Math Probl Eng. 2014;2014.

45. Miyazaki S, Imai T, Igo Y, Otsuka K. Effect of Cyclic Deformation on the Pseudoelasticity Characteristics of Ti-Ni Alloys.

46. Kohl M, Just E, Pfleging W, Miyazaki S. SMA microgripper with integrated antagonism [Internet]. Vol. 83, Sensors and Actuators. 2000. Available from: www.elsevier.nlrlocatersna

47. Otsuka K, Ren X. Recent developments in the research of shape memory alloys.

48. Velmurugan C, Senthilkumar V, Dinesh S, Arulkirubakaran D. Review on phase transformation behavior of NiTi shape memory alloys [Internet]. Vol. 5, Materials Today: Proceedings. 2018. Available from: www.sciencedirect.comwww.materialstoday.com/proceedings

49. Jiang S, Sun D, Zhang Y, Hu L. Deformation behavior and microstructure evolution of NiTiCu shape memory alloy

subjected to plastic deformation at high temperatures. Metals (Basel). 2017 Aug 3;7(8).

50. Patra N, Geetha SR, Harish C, Chouhan N, Singh V, Palani IA. Compositional influence of CuAlMn SMA coated optical fiber towards sensing low temperature. Sens Actuators A Phys. 2024 Feb 1;366.

51. Surbled-sputtering.

52. Sun H, Nykypanchuk D. New Insights into Shape Memory Alloy Bimorph Actuators Formed by Electron Beam Evaporation.

53. Cocean A, Cocean I, Gurlui S, Iacomi F. STUDY OF THE PULSED LASER DEPOSITION PHENOMENA BY MEANS OF COMSOL MULTIPHYSICS. UPB Sci Bull, Series A. 2017;79(2).

54. Geetha M, Dhanalakshmi K, Jayachandran S, Palani IA, Sathish Kumar V. Analysis of actuation characteristics of CuAlNiMn/Polyimide thin film shape memory alloy. In: Materials Today: Proceedings. Elsevier Ltd; 2019. p. 9580–5.

55. Geetha Priyadarshini B, Aich S, Chakraborty M. Nano-crystalline Ni-Ti alloy thin films fabricated using magnetron co-sputtering from elemental targets: Effect of substrate conditions. Thin Solid Films. 2016 Oct 1;616:733–45.

56. Lagoudas DC. Shape memory alloys : modeling and engineering applications. Springer; 2008. 435 p.

57. Noh HY, Lee KH, Cui X, Choi CS. The composition and structure of TiNi thin film formed by electron beam evaporation [Internet]. 2000. Available from: www.elsevier.com/locate/scriptamat

58. Summers GJ, Kasiama MG, Summers CA. Polyimides and Sulfonated Polyimides Derived from Functionalized 1,1-Diphenylethylene Derivatives. Macromol Symp. 2017 Oct 1;375(1).

59. Sun Y, Zhu Z, Jin Y, Liu C, Wang Z, Liu J, Hou M, Zhang Q. The effects of high electronic energy loss on the chemical modification of polyimide q [Internet]. Available from: www.elsevier.com/locate/nimb

60. Kumar V, Goyal P, Gupta R, Kumar S, Goyal PK. Tailoring of optical band gap and refractive index of heat treated Kapton-H Polyimide. Available from: https://www.researchgate.net/publication/268367040

61. Severin D, Ensinger W, Neumann R, Trautmann C, Walter G, Alig I, Dudkin S. Degradation of polyimide under irradiation with swift heavy ions. In: Nuclear Instruments and Methods in Physics Research, Section B: Beam Interactions with Materials and Atoms. 2005. p. 456–60.

62. Megusar J. Low temperature fast-neutron and gamma irradiation of Kapton ® polyimide films. Vol. 245, Journal of Nuclear Materials. 1997.

63. Mihailov S, Duley W. Study of the ablation threshold of polyimide (Kapton H) utilizing double-pulsed XeCl excimer laser radiation. J Appl Phys. 1991;69(7):4092–102.

64. Mihailov S, Duley WW. Study of surface reflectivity and etch rates of polyimide (Kapton H) utilizing double-pulsed 308 nm laser radiation. J Appl Phys. 1993;73(5):2510–7.

65. Sahre K, Eichhorn KJ, Simon F, Pleul D, Janke A, Gerlach G. Characterization of ion-beam modified polyimide layers. Vol. 139, Surface and Coatings Technology. 2001.

66. Oldham KB, Parnis JM. Shining light on Beer's law. ChemTexts. 2017 Jun 1;3(2).

67. Lu QH, Li M, Yin J, Zhu ZK, Wang ZG. Polyimide surface modification by pulsed ultraviolet laser irradiation with low fluence. J Appl Polym Sci. 2001 Dec 9;82(11):2739–43.

68. Lind J, Hagenlocher C, Weckenmann N, Blazquez-Sanchez D, Ackermann C, Weber R, Graf T. Adjustment of the cutting front and kerf by means of beam shaping to increase the speed of laser cutting.

69. Arun A, Rajkumar K, Santosh S. Fiber laser cutting study on ternary NiTiV shape memory alloy. Materials and Manufacturing Processes. 2023;38(14):1745–54.

70. Caiazzo F, Curcio F, Daurelio G, Minutolo FMC. Laser cutting of different polymeric plastics (PE, PP and PC) by a CO 2 laser beam. J Mater Process Technol. 2005 Feb 10;159(3):279–85.

71. Santosh S, Kevin Thomas J, Pavithran M, Nithyanandh G, Ashwath J. An experimental analysis on the influence of CO2 laser machining parameters on a copper-based shape memory alloy. Opt Laser Technol. 2022 Sep 1;153.

72. Ravindran DM, Palanisamy C. Accuracy and Heat affected Zone Study on Polycarbonate CO 2 Laser Cutting [Internet]. Available from: https://ssrn.com/abstract=4498250

73. El-Eskandarany MS. Metallic glassy Ti 2 Ni grain-growth inhibitor powder for enhancing the hydrogenation/dehydrogenation kinetics of MgH 2. RSC Adv. 2019;9(2):1036–46.

74. Shilei Z, Kun Z, Fuwen W. Microstructure and phase transition characteristics of NiTi shape memory alloy. In: Journal of Physics: Conference Series. IOP Publishing Ltd; 2020.

75. Balasubramaniyan C, Rajkumar K, Santosh S. Fiber Laser Cutting of Cu–Zr Added Quaternary NiTi Shape Memory Alloy: Experimental Investigation and Optimization. Arab J Sci Eng. 2023 Mar 1;48(3):3665–79.

76. Jayachandran S, Karna P, Gangwar K, Kaithwas A, Resnina N, Belyaev S, Palani IA. Parametric investigation on laser micro-patterned CuAlNi Shape-memory alloy (SMA) bimorph micromirror and its actuation performance. Transactions of the Indian Institute of Metals. 2021 Oct 1;74(10):2471–80.

77. Gangwar K, Jayachandran S, Sahu A, Singh A, Palani IA. Influence of pre-strain on attributes of Ni-rich NiTi/ Kapton polyimide bimorph for flexible mirrors. Sens Actuators A Phys [Internet]. 2022 Jul;341:113607. Available from: https://linkinghub.elsevier.com/retrieve/pii/S092442472200245X

78. Gangwar K, Gupta D, Anand PI. Parametric Investigation on laser annealing of polyimide on improving the characteristics of NiTi SMA-based bimorph towards the development of microactuators. Sens Actuators A Phys [Internet]. 2023 Oct;360:114536. Available from: https://linkinghub.elsevier.com/retrieve/pii/S0924424723003850

79. Stepanova K, Rozlivek J, Puciow F, Krsek P, Pajdla T, Hoffmann M. Automatic self-contained calibration of an industrial dual-arm robot with cameras using self-contact, planar constraints, and self-observation. Robot Comput Integr Manuf. 2022 Feb 1;73.

80. Zhong Y, Wang Z, Yalamanchili A V., Yadav A, Srivatsa BNR, Saripalli S, Bukkapatnam STS. Image-based flight control of unmanned aerial vehicles (UAVs) for material handling in custom manufacturing. J Manuf Syst. 2020 Jul 1;56:615–21.

81. Qiu Z, Lin D, Jin R, Lv J, Zheng Z. A Global ArUco-Based Lidar Navigation System for UAV Navigation in GNSS-Denied Environments. Aerospace. 2022 Aug 1;9(8).

82. Can Kara O, Member S, Everson C, Alambeigi F. Towards Design and Development of an ArUco Markers-Based Quantitative Surface Tactile Sensor.

83. Rato D, Oliveira M, Santos V, Gomes M, Sappa A. A sensor-to-pattern calibration framework for multi-modal industrial collaborative cells. J Manuf Syst. 2022 Jul 1;64:497–507.

84. Vela C, Fasano G, Opromolla R. Pose determination of passively cooperative spacecraft in close proximity using a monocular camera and AruCo markers. Acta Astronaut. 2022 Dec 1;201:22–38.

85. Oščádal P, Heczko D, Vysocký A, Mlotek J, Novák P, Virgala I, Sukop M, Bobovský Z. Improved pose estimation of aruco tags using a novel 3d placement strategy. Vol. 20, Sensors (Switzerland). MDPI AG; 2020. p. 1–16.

86. Čepon G, Ocepek D, Kodrič M, Demšar M, Bregar T, Boltežar M. Impact-Pose Estimation Using ArUco Markers in Structural Dynamics. Exp Tech. 2023;